Exploration and Application of Mechanoresponsive Polymers: Polymer Architecture, Amplified Response, and Additive Manufacturing

Gregory I. Peterson

A dissertation
submitted in partial fulfillment of the
requirements for the degree of:

Doctor of Philosophy

University of Washington

2015

Reading Committee:

Andrew J. Boydston, Chair

Daniel T. Chiu

Gojko Lalic

Program Authorized to Offer Degree:

Chemistry

University of Washington

Abstract

Exploration and Application of Mechanoresponsive Polymers: Polymer Architecture, Amplified Response, and Additive Manufacturing

Gregory I. Peterson

Chairperson of the Supervisory Committee:
Professor Andrew J. Boydston
Department of Chemistry

My graduate work has been primarily dedicated to basic and applied research in the field of polymer mechanochemistry, or more specifically, the exploration and application of polymers that undergo targeted chemical transformations in response to mechanical force. In chapter one, I begin by discussing our work on exploring how polymer architecture affects the kinetics of mechanochemical reactivity. We compared linear and star polymer degradation kinetics both with and without mechanoresponsive moieties in the polymer backbone. We determined that the molecular weight of the arms, regardless of architecture, was the defining kinetic parameter. In the next chapter, I describe the development of a computational model that predicts the evolving molecular weight distribution of star polymers undergoing mechanochemical degradation. We demonstrate the model for three- and four-arm star polymers and describe how it can be expanded for a n-arm star polymer. In chapter three, I discuss our work on studying the kinetics and mechanism of mechanochemical activation, and subsequent depolymerization, of a low ceiling temperature polymer. In addition to our demonstrating that complete deppolymerization of a polymer to its monomer units is possible (mechanochemically), we also are able to experimentally support a heterolytic degradation mechanism, which is rare in polymer mechanochemistry. I conclude my work on mechanochemisty by describing our work on 3D printing of

mechanochromic polymers. We printed complex architectures that would be difficult if not impossible to prepare with other manufacturing techniques, as well as developed a prototype force sensor. I conclude this dissertation by describing some of the work that I have done that is not related to polymer mechanochemisty. I discuss our work on developing a thermal trigger for the depolymerization of a polyurethane into its monomer units. We explored the temperature-dependent depolymerization kinetics and confirmed the mechanism of the trigger activation with chain-end trapping experiments.

Table of Contents

List of Abbreviations

3DP – three-dimensional printing

ATRP – atom transfer radical polymerization

CAD – computer aided design

Đ – dispersity (equivalent to PDI)

DMA – *N*,*N*-dimethylacrylamide

DMF – *N*,*N*-dimethylformamide

DMSO – dimethylsulfoxide

DP – degree of polymerization

EDTA – ethylenediaminetetraacetic acid

FFF – fused filament fabrication

GPC – gel permeation chromatography

k_{PL} – first-order rate constant obtained via PL

k_{RI} – first-order rate constant obtained via GPC

Ln – natural log

MALS – multiangle laser light scattering

M – molecular weight

M_{arm} – arm molecular weight

M_{lim} – limiting molecular weight

M_n – number average molecular weight

M_p – molecular weight at the P_{max} retention time

M_{span} – spanning molecular weight (two times M_{arm})

M_{total} – total molecular weight

M_w – weight average molecular weight

MWD – molecular weight distribution

NMR – nuclear magnetic resonance

Oct – 2-ethylhexanoate

P_2-t-Bu – 1-*tert*-Butyl-2,2,4,4,4-pentakis(dimethylamino)-2λ^5,4λ^5-catenadi(phosphazene)

PA – *ortho*-phthalaldehyde

PCL – poly(ε-caprolactone)

PDI – polydispersity index

PDMA – poly(*N*,*N*-dimethylacrylamide)

PL – photoluminescence

PMA – poly(methyl acrylate)

P_{max} – peak maximum

PPA – poly(phthalaldehyde)

RI – refractive index

RT – room temperature

SIP – self-immolative polymer

TBAP – tetrabutylammonium periodate

TBS-Cl – *tert*-butyldimethylsilyl chloride

T_c – ceiling temperature

TLC – thin layer chromatography

TFAA – trifluoroacetic anhydride

THF – tetrahydrofuran

TREN – tris(2-aminoethyl)amine

UV – ultraviolet light

UV-vis – ultraviolet-visible light

List of Figures

List of Schemes

List of Tables

Acknowledgments

I would first like to acknowledge my advisor, AJ Boydston. Without his never-ending dedication and enthusiasm for this research program, this work would have never been possible. I thank him for his constant support and for making me a better person, both in and out of the lab. I would also like to acknowledge the original Boydston group members: Mike Larsen, Kelli Ogawa, and Derek Church. They made working in the lab more enjoyable and have undoubtedly made intellectual contributions to each of these projects. Below are the acknowledgments specific to each chapter.

Chapter 1: I thank Derek Church, the lead author on this paper. The staff from Wyatt Technologies Corporation for helpful discussions. Financial support of this research by the University of Washington, University of Washington Royalty Research Fund, and Army Research Office Young Investigator Program (grant number W911NF-11-1-0289).

Chapter 2: I thank Derek Church for making the polymers for the experimental component of this project. The staff of Wyatt Technology Corporation for helpful discussions regarding number fraction GPC plots. Financial support of this research by the University of Washington and the Army Research Office Young Investigator Program (grant number W911NF-11-1-0289).

Chapter 3: I thank our collaborators Jeff Moore, Todd Martinez, Scott White, and their researchers who were coauthors on the first report that was published in Nature Chemistry. Financial support of this research by the University of Washington, University of Washington Royalty

Research Fund, and Army Research Office Young Investigator Program (grant number W911NF-11-1-0289).

Chapter 4: I thank Mike Larsen, who was the second author on this paper. Also, Mark Ganter and Duane Storti, our Mechanical Engineering collaborators, and Mete Yurtoglu (ME graduate student) who was a coauthor on our (not so) "initial" report in the Rapid Prototyping Journal. Financial support of this research by from the University of Washington.

Chapter 5: I thank Derek Church, who was the second author on this paper. Also, Neal Yakelis, Brian Levandowski, and Alex Wisbeck for helpful discussions regarding the trigger design and reactivity. Financial support from the University of Washington, University of Washington Royalty Research Fund, Army Research Office Young Investigator Program (grant number W911NF-11-1-0289), and Army Research Office STIR Program (grant number W911NF-14-1-0213).

Chapter 1 – Comparison of Mechanochemical Chain Scission Rates for Linear versus Three-Arm Star Polymers in Strong Acoustic Fields

1.1. Introduction

Mechanochemistry involves transduction of mechanical input into chemical output by coupling force vectors with productive geometric distortions of functional groups.[1] Polymer mechanochemistry, specifically, uses macromolecular scaffolds to direct and distribute mechanical forces as a function of shape and composition of the polymer framework.[2,3] Perhaps the simplest chemical output that can arise from tensile forces within a polymer main chain is bond scission leading to fragmentation of the polymer. Understanding mechanochemical chain scission has important implications for multiple disciplines, considering that a number of physicochemical properties depend upon polymer molecular weight.

Studies focusing on the influence of polymer structure on mechanochemical reactivity have unveiled key correlations.[4–7] One of the most basic tenets for linear polymers in elongational flow fields is a linear relationship between chain scission rate and molecular weight.[8] Variations in polymer shape, however, give rise to changes in molecular weight distribution, which in turn can influence scission rates. For example, star polymers display an enhanced shear stability in comparison with linear polymer analogues of the same total molecular weight (M_{total}).[5,9] This effect is ascribed to the star polymers having a lower effective molecular weight that is roughly

equivalent to two of the arms. This spanning region has a molecular weight (M_{span}) that is much lower than the M_{total}, thus the slower rate of chain scission.[5c]

One of the challenges to determining rate constants for specific chain scission events is that daughter fragments typically have molecular weights greater than the limiting molecular weight (M_{lim}) for chain scission. Therefore, commonly employed analyses of changes in ensemble averages for a polymer sample, such as molecular weight or viscosity, are not explicitly linked to chain scission in a single species (Figure 1). For example, Striegel and co-workers have studied ultrasound-induced chain scission in a series of star polymers and observed an apparent increase in observed rate constant upon prolonged sonication.[5c] This was explained by an increase in the number of polymer species present that were above M_{lim} as the star polymers shed arms and an inability to distinguish between the reacting species when monitoring the average molecular weight of the mixture. Herein, we describe a quantitative assessment of rate constants for mechanochemical chain scission in complementary series of star and linear polymers and resolution of scission events between parent and daughter species.

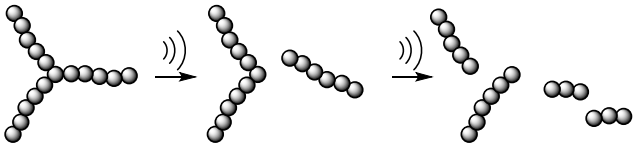

Figure 1. Generalized depiction of chain scission sequences in parent.

1.2. Results and Discussion

To begin, we synthesized a series of well-defined linear and three-arm polymer counterparts as depicted in Figure 2. The linear analogues were designed to represent the "two-arm" daughter fragments resulting from hypothetical single-arm cleavage of the corresponding

three-arm star polymer. Observed trends were found to be independent of either planar or tetrahedral core geometries (vide infra). We used a "core-first" approach and atom-transfer radical polymerization to produce a series of polymers each with narrow polydispersity index (PDI).[10] Kinetic analyses were conducted using the method described by Florea.[11] This method involves following the refractive index (RI) signal intensity of a single section of the insipient portion of the gel-permeation chromatogram over the course of the sonication experiment. This approach more effectively distinguishes initial chain scission from scission of daughter fragments than the average molecular weight analysis developed by Malhotra and used by Striegel.[5c,12] A caveat of the Florea method, however, is that adequate resolution of polymer species by gel permeation chromatography (GPC) must be achieved.

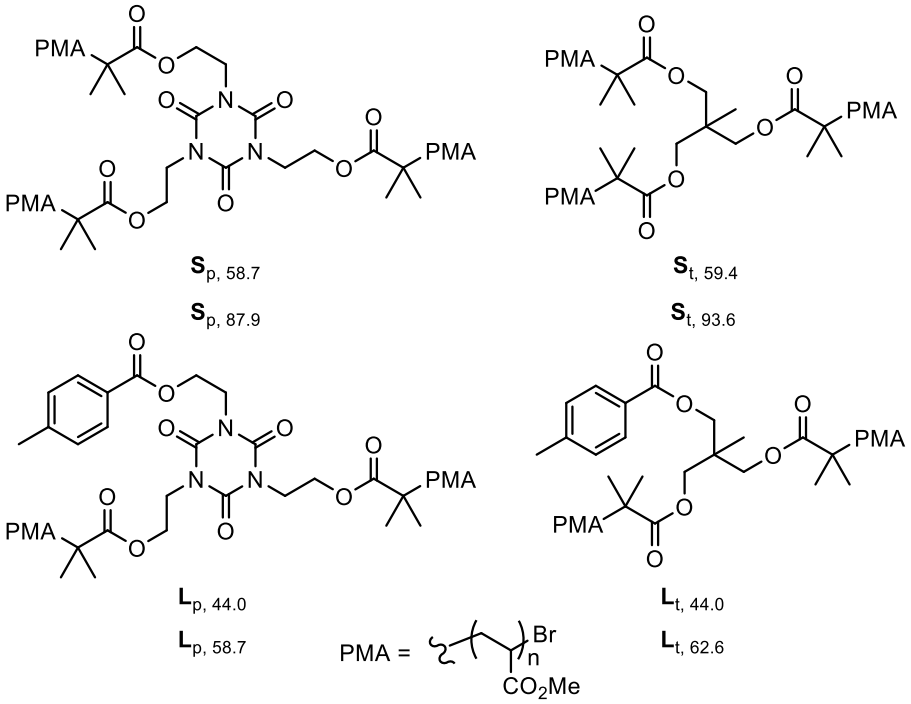

Figure 2. Structures of star and linear polymers used in this study. Subscripts indicate core geometry (planar or tetrahedral) and M_n values. All PDIs were found to be <1.1 (see Table 3 in section 1.4.3.).

Each linear and star polymer was subjected to sonication in DMF, and aliquots were analyzed by GPC over time. As a representative example, GPC traces of $\mathbf{S}_{t,59.4}$ are depicted in Figure 3 (top). The peak maximum (P_{max}) retention time before sonication was found to be 20.4 min (indicated by the dashed red line). Monitoring the RI signal intensity at that retention time over the course of the sonication experiment provided a first-order rate constant (k_{RI}) for the consumption of the polymer species with a molecular weight of M_p. The P_{max} for each initial polymer remained consistent throughout the set of three runs, indicating to us that column drift was not significant (see Table 4 in section 1.4.4.).

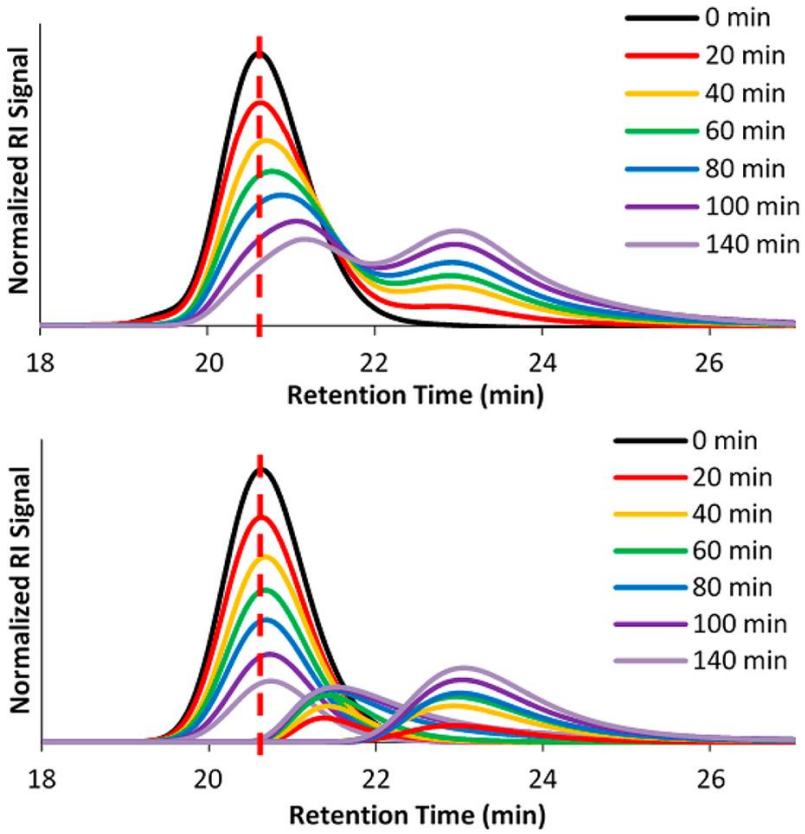

Figure 3. (top) GPC traces of $\mathbf{S}_{t,59.4}$ during ultrasonication. Sonication conditions: polymer concentration of 5 mg/mL in DMF, 13.8 W/cm^2, duty cycle of 1 s on 9 s off, N_2 atmosphere, 4 °C monitored internally. (bottom) Resolved GPC traces from nonlinear regression analysis of the

chromatograms in the top plot. Dashed red lines indicate the retention time at which RI signal intensity was recorded for kinetic analyses.

Applying the same sonication conditions and analyses to each of the polymers in the series provided k_{RI} values as listed in Table 1. The trends are consistent with those observed by Striegel in which the M_{arm}, as opposed to M_{total}, of the polymer dictates the rate of chain scission.[5c] While two sequential chain scission events are operative in the mechanochemical degradation of three-arm star polymers, k_{RI} for consumption of each star polymer closely matches that of the corresponding linear counterpart of equal M_{arm}. For polymers with M_{arm} of ca. 20 kDa, k_{RI} were all similar, ranging from 1.02 to 1.26 × 10^{-2} min^{-1}. Moreover, the differences in k_{RI} correlated well with the slight differences in M_{arm}. The same general trend was observed from the polymers bearing ~30 kDa arms, with k_{RI} clustered between 2.38 and 2.66 × 10^{-2} min^{-1}. Notably, an increase in linear polymer M_{total} from $\mathbf{L_t}_{,44.0}$ to $\mathbf{L}_{t,62.6}$ resulted in an approximately doubled value of k_{RI}. In contrast, increasing M_{total} via a branch point to form a star polymer (cf. $\mathbf{L}_{t,44.0}$ versus $\mathbf{S}_{t,59.4}$) actually resulted in a slight reduction in k_{RI}, consistent with the reduction in M_{arm}.

Table 1. Summary of k_{RI} for mechanochemical chain scission of three-arm star and linear polymers.[a]

Polymer	M_{total} (kDa)	M_{arm} (kDa)	k_{RI} (× 10^{-2} min^{-1})
$\mathbf{S}_{p,58.7}$	58.7	19.6	1.02 ± 0.02
$\mathbf{S}_{t,59.4}$	59.4	19.8	1.10 ± 0.02
$\mathbf{L}_{p,44.0}$	44.0	22.0	1.26 ± 0.03
$\mathbf{L}_{t,44.0}$	44.0	22.0	1.25 ± 0.08
$\mathbf{S}_{p,87.9}$	87.9	29.3	2.44 ± 0.17
$\mathbf{L}_{p,58.7}$	58.7	29.3	2.38 ± 0.12
$\mathbf{S}_{t,93.6}$	93.6	31.2	2.66 ± 0.14
$\mathbf{L}_{t,62.6}$	62.6	31.3	2.63 ± 0.06

[a]Mtotal (M_n values) determined by GPC analysis using multiangle laser light scattering (MALS) to give M_w values from which M_n values were calculated. M_{arm} were assumed to be one-third M_{total} for stars and one-half M_{total} for linear polymers. Rate constants were calculated from linear regression of the Ln(RI signal intensity) at the P_{max} retention time of the virgin sample versus ultrasonication "on time" and are an average of three runs ± one standard deviation.

A nonlinear regression analysis was used to resolve each GPC trace, which verified that the daughter fragments were not significantly contributing to the peak height at the retention time used for determining k_{RI} (Figure 3, bottom). Using the resolved peaks, we calculated rate constants for scission of the initial polymer based upon the resolved initial P_{max} retention time RI intensity (k_{res}) and total peak area (k_{area}) for that species. We found k_{RI} to be in good agreement with k_{res} and k_{area} for each polymer (see Table 5 in section 1.4.4.).

To investigate site-selective mechanophore activation as a function of polymer shape, we also prepared and analyzed a linear ($\mathbf{L}_{DA,61.6}$) and star polymer ($\mathbf{S}_{DA,85.9}$) pair that each contained an anthracene-maleimide Diels−Alder adduct mechanophore (Figure 4). Importantly, the average M_{arm} was similar in each polymer. The mechanophore, which has been extensively studied by Bielawski and co-workers, is capable of mechanochemical UV−vis and photoluminescence (PL) "turn-on" response upon mechanically facilitated cycloreversion to generate an anthracene moiety.[13]

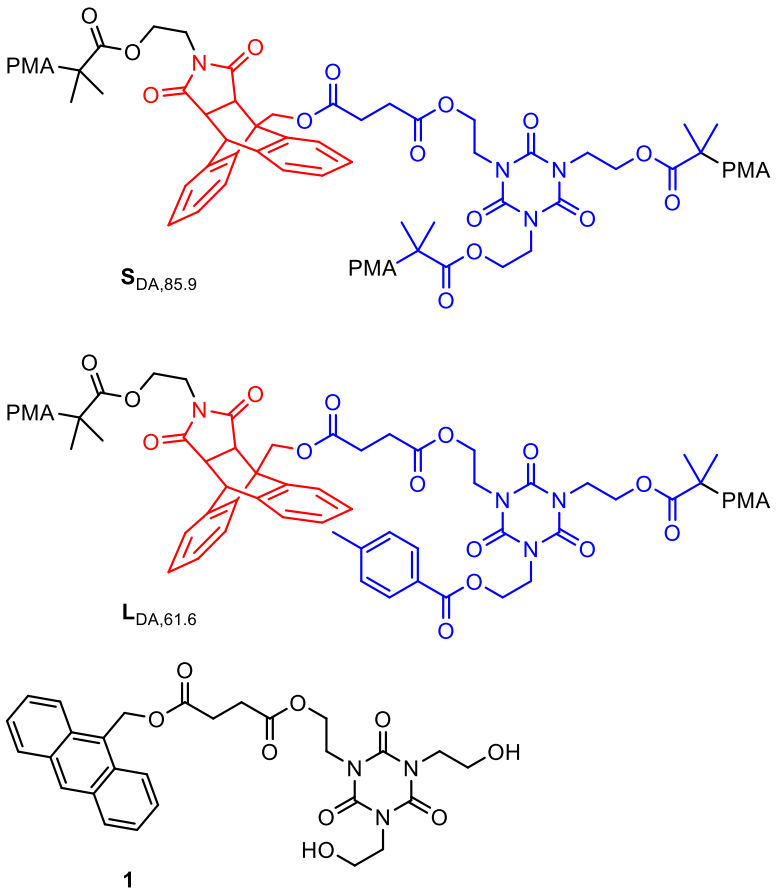

$\mathbf{S}_{DA,85.9}$ $\mathbf{L}_{DA,61.6}$ **1**

Figure 4. Mechanophore-containing star ($\mathbf{S}_{DA,85.9}$) and linear ($\mathbf{L}_{DA,61.6}$) polymers and PL control compound **1**. Mechanophore is highlighted in red and core is highlighted in blue.

After subjecting $\mathbf{L}_{DA,61.6}$ and $\mathbf{S}_{DA,85.9}$ each to sonication as described above, the formation of anthracene was confirmed by UV−vis (Figure 5A) and PL spectroscopies (Figure 5B). Although the UV−vis spectra were consistent with formation of anthracene, control experiments revealed increases in solution optical density upon sonication of PMA (absent mechanophore). Although background corrections could be made, the optical density was dependent upon the extent of chain scission, which occurred at different rates and via different mechanisms for unfunctionalized PMA versus mechanophore-containing polymers (vide infra). PL experiments, however, confirmed

consistent emission intensity over 60 min of sonication time (Figure 5C) for an anthracene-containing control (**1**) sonicated in the presence of $\mathbf{L}_{P,58.7}$. This confirmed the stability of anthracene to sonication and circumvents issues with increased optical density upon sonication of polymer solutions. Additionally, we observed a linear correlation between PL intensity and concentration of **1** over the concentration range relevant to our kinetic studies (Figure 5D).

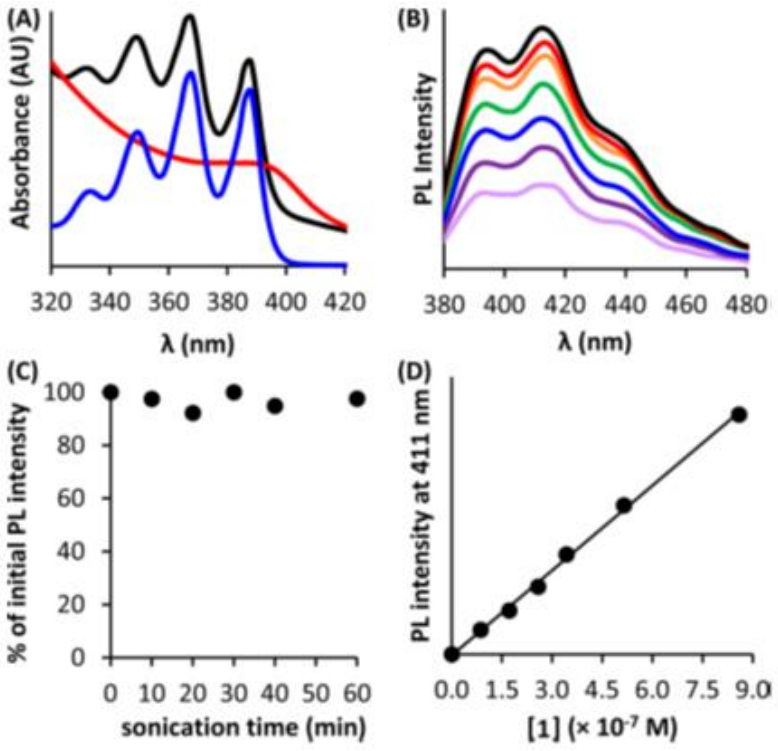

Figure 5. (A) UV−vis spectra in DMF of $\mathbf{S}_{DA,85.9}$ before (red) and after (black) sonication and a small molecule control (**1**, blue); (B) PL spectra in DMF of $\mathbf{L}_{DA,61.6}$ upon increasing sonication time (10−40 min, 5 min increments bottom-to-top); (C) % of initial PL intensity with increasing sonication time of a mixture of $\mathbf{L}_{p,58.7}$ and **1** in DMF; (D) PL intensity versus concentration of **1** in the presence of $\mathbf{L}_{p,58.7}$ ($R^2 = 0.9981$).

Monitoring the consumption of initial polymer via GPC-RI, and production of anthracene via PL spectroscopy (to give k_{PL}), provided corroborating data for consistent chain scission rate constants between the two polymer structures. As in the previous series, we found k_{RI} for the linear and star analogues to be very similar, consistent with their similar M_{arm} values (Table 2). Additionally, the k_{PL} values for each polymer were also similar to one another and to the k_{RI} values. The similarity between the k_{RI} and k_{PL} values is consistent with high selectivity for initial chain scission occurring at the mechanophore.

Table 2. Rate constants for mechanochemical chain scission for $\mathbf{S}_{DA,85.9}$ and $\mathbf{L}_{DA,61.6}$.[a]

Polymer	M_{total} (kDa)	M_{arm} (kDa)	k_{RI} ($\times 10^{-2}$ min^{-1})	k_{PL} ($\times 10^{-2}$ min^{-1})
$\mathbf{S}_{DA,85.9}$	85.9	28.6	3.13 ± 0.11	3.20 ± 0.14
$\mathbf{L}_{DA,61.6}$	61.6	30.8	3.27 ± 0.38	3.26 ± 0.09

[a]M_{total}, M_{arm}, and k_{RI} were determined as described above. Rate constants via PL (k_{PL}) were calculated from linear regression of the Ln(PL intensity at 411 nm) versus ultrasonication "on time". Rate constants are an average of three runs ± one standard deviation.

The inclusion of the mechanophore resulted in a discernible increase in k_{RI}, (cf. Table 1 and Table 2). Specifically, polymers with M_{arm} values near 30 kDa clearly had k_{RI} values less than those observed from the mechanophore-containing polymers. To our knowledge, direct comparisons of rate constants for this mechanophore versus PMA homopolymers have not been reported. However, the relative increase in rate constant upon inclusion of the mechanophore in these studies is consistent with those reported by Moore and co-workers for investigation of cyclobutane-based mechanophores.[8b]

1.3. Conclusions

In summary, we report precise investigations of mechanochemical chain scission rates in linear and three-arm star polymers. Our results are consistent with previous chain scission models in which the scission rate is governed by the length of any two arms emanating from the core. By resolving daughter fragments from the analysis and incorporating a fluorogenic "turn-on" mechanophore, we have provided kinetic analysis for specific scission events. These results provide quantitative guidelines for augmenting the mechanochemical reaction rates of macromolecules through control of the overall polymer architecture. Importantly, we observed nearly identical rate constants for activation of a mechanophore incorporated into structurally varied polymers of significantly different molecular weights.

1.4. Experimental

1.4.1. General Considerations

Dry DMF was obtained from a Glass Contour solvent purification system. All other reagents and solvents were used as obtained from commercial sources. GPC setup consists of: a Shimadzu pump, three in-line MZ-Gel 10 μm size-exclusion columns (10^3, 10^3, and 10^5 Å), DAWN-HELEOS II 18-angle multi-angle laser light scatter and OptiLab T-rEx refractive index detectors (each from Wyatt Technologies Corporation), and an Agilent Technologies UV-vis detector. The mobile phase consisted of 0.01 M LiBr in DMF. No calibration standards were used, and dn/dc values were obtained for each injection assuming 100% mass elution from the columns. Sonication experiments were done using a 20 kHz Sonics VSX series sonication probe (1.2 cm tip diameter) calibrated according to literature procedures.[14] Fluorescence spectroscopy was

conducted using a Perkin Elmer Luminescence Spectrometer LS 50 B. UV-vis spectra were recorded on a Varian Cary 500 scan UV-Vis-NIR Spectrophotometer.

1.4.2. Synthesis and Characterization of Polymers and Controls

Compounds were prepared and characterized via ^{1}H and ^{13}C NMR spectroscopy, as well as low-resolution mass spectroscopy. Synthetic protocols and characterization data can be found in the Supplemental Information of the published manuscript.[15]

1.4.3. Sonication Procedure

Sonication experiments were done in a flame-dried, N_2-purged Suslick flask, with the sonication horn (1 cm diameter) already attached to Suslick flask. Each arm of the Suslick flask was fitted with a rubber septum. In a separate flame-dried round bottom flask, the polymer sample was dissolved in dry DMF at a concentration of 5 mg/ml. The polymer solution was then transferred to the Suslick flask under dry N_2 via syringe. The entire apparatus (sonication horn + Suslick flask) was then transferred to a cold room (4 °C) for the duration of sonication experiment. Polymer solutions were sonicated at 13.8 W/cm^2 for a pulse of 1s on, 9s off. Aliquots of 0.5 mL were withdrawn from the reaction periodically and analyzed by GPC. Final GPC analysis data are given in Table 3. ^{1}H NMR spectra of the polymers before and after sonication showed consistent resonances for the core structure. This indicated to us that the core remained intact during sonication, and chain scission was occurring within the polymer arm. Representative spectra are shown in Figure 6.

Table 3. GPC data for star and linear polymers before (top) and after (bottom) sonication.

Polymer	M_n (kDa)	M_w (kDa)	PDI
$\mathbf{S}_{p,58.7}$	58.7	59.9	1.02
$\mathbf{S}_{t,59.4}$	59.4	60.6	1.02
$\mathbf{L}_{p,44.0}$	44.0	45.8	1.04
$\mathbf{L}_{t,44.0}$	44.0	44.4	1.01
$\mathbf{S}_{p,87.9}$	87.9	88.8	1.01
$\mathbf{L}_{p,58.7}$	58.7	59.3	1.01
$\mathbf{S}_{t,93.6}$	93.6	97.3	1.04
$\mathbf{L}_{t,62.6}$	62.6	64.5	1.03
$\mathbf{S}_{DA,\ 85.9}$	85.9	87.6	1.02
$\mathbf{L}_{DA,61.6}$	61.6	63.5	1.03
Polymer	M_n (kDa)	M_w (kDa)	PDI
$\mathbf{S}_{p,58.7}$	22.6	30.2	1.34
$\mathbf{S}_{t,59.4}$	26.1	31.9	1.23
$\mathbf{L}_{p,44.0}$	21.0	23.6	1.12
$\mathbf{L}_{t,44.0}$	19.8	23.3	1.19
$\mathbf{S}_{p,87.9}$	41.1	53.2	1.30
$\mathbf{L}_{p,58.7}$	29.7	35.9	1.21
$\mathbf{S}_{t,93.6}$	36.7	51.0	1.40
$\mathbf{L}_{t,62.6}$	29.0	35.1	1.20
$\mathbf{S}_{DA,\ 85.9}$	42.7	51.0	1.20
$\mathbf{L}_{DA,61.6}$	33.0	38.7	1.17

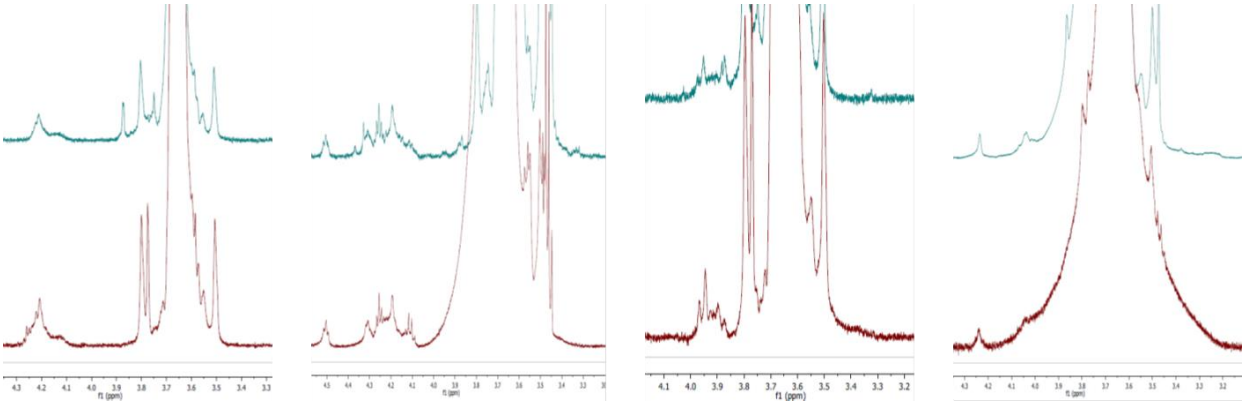

Figure 6. Representative ^{1}H NMR spectra before (red) and after (blue) sonication. From left to right: $\mathbf{S}_{p,58.7}$, $\mathbf{L}_{p,44.0}$, $\mathbf{S}_{t,59.4}$, $\mathbf{L}_{t,44.0}$.

1.4.4. Data Analysis

During sonication experiments, aliquots were withdrawn and injected directly into the GPC system, which uses a manual injector with a loop volume of 143 µL. Polymer peaks in the RI traces were normalized to constant area. The peak maximum (P_{max}) retention time of each virgin polymer was recorded. The RI intensity at that retention time for each normalized GPC trace taken during sonication was then used to generate a first-order kinetic plot. Three independent experiments were conducted for each polymer sample, with aliquots being drawn at the same time intervals for each run. The rate constants (k_{RI}) determined from each run were averaged, and standard deviations were calculated. Plots shown in Appendix A provide the average value for each data point, with error bars representing the standard deviation for each. Column drift was also investigated and found to be small (Table 4). Specifically, the standard deviation for the P_{max} retention time for the time zero samples were found to be < 0.2 min for each polymer sample.

Table 4. Average peak maxima for time zero GPC traces.

Polymer	Mean P_{max} Retention Time (min)	Standard Deviation (min)
$\mathbf{S}_{p,58.7}$	20.498	0.028
$\mathbf{S}_{t,59.4}$	20.551	0.100
$\mathbf{L}_{p,44.0}$	20.898	0.009
$\mathbf{L}_{t,44.0}$	21.014	0.187
$\mathbf{S}_{p,87.9}$	19.756	0.041
$\mathbf{L}_{p,58.7}$	20.408	0.024
$\mathbf{S}_{t,93.6}$	19.682	0.033
$\mathbf{L}_{t,62.6}$	20.166	0.016
$\mathbf{S}_{DA,\ 85.9}$	19.640	0.000
$\mathbf{L}_{DA,61.6}$	20.151	0.060

To verify that the daughter fragments were not contributing to the RI signal intensity of the reactant polymer, the overlapping peaks were resolved using a non-linear regression analysis. For linear and star polymers, GPC peaks were assumed to be the sum of two or three polynomial modified Gaussian functions, respectively.[16] The Microsoft Excel Solver function was used to minimize the sum of squared differences between the experimental and fit data. Peak resolution was completed for a single run of each polymer type. For comparison, the experimental and corresponding resolved GPC traces for each experiment are shown in Appendix A. The red vertical lines indicate the retention time used for rate constant determination. The resolved data were used to calculate rate constants based upon the RI intensities (k_{res}), and the total area of the reactant polymer peak (k_{area}). The peak resolution studies suggest that the daughter fragments do not significantly contribute to the intensity at the initial P_{max} retention time, which is further supported by the consistency of the rate constants determined from the experimental and resolved data (summarized in Table 5).

Table 5. Summary of rate constants for consumption of parent polymer via mechanochemical chain scission.

Polymer	M_{total} (kDa)	M_{arm} (kDa)	k_{RI} (× 10^{-2} min^{-1})	k_{res} (× 10^{-2} min^{-1})	k_{area} (× 10^{-2} min^{-1})
$\mathbf{S}_{p,58.7}$	58.7	19.6	1.02 ± 0.02	0.99	0.95
$\mathbf{S}_{t,59.4}$	59.4	19.8	1.10 ± 0.02	1.12	1.09
$\mathbf{L}_{p,44.0}$	44.0	22.0	1.26 ± 0.03	1.24	1.20
$\mathbf{L}_{t,44.0}$	44.0	22.0	1.25 ± 0.08	1.15	1.12
$\mathbf{S}_{p,87.9}$	87.9	29.3	2.44 ± 0.17	2.31	2.29
$\mathbf{L}_{p,58.7}$	58.7	29.3	2.38 ± 0.12	2.35	2.35
$\mathbf{S}_{t,93.6}$	93.6	31.2	2.66 ± 0.14	2.48	2.43
$\mathbf{L}_{t,62.6}$	62.6	31.3	2.63 ± 0.06	2.74	2.72
$\mathbf{S}_{DA,\ 85.9}$	85.9	28.6	3.13 ± 0.11	3.33	3.30
$\mathbf{L}_{DA,61.6}$	61.6	30.8	3.27 ± 0.38	3.00	2.87

For polymers containing the Diels-Alder adduct mechanophore, rate constants were also determined by photoluminescence spectroscopy. A 50 µL aliquot was drawn at various time points during the sonication experiment. The aliquot was then diluted to 5 mL total volume using a volumetric flask and filtered through a 0.45 µm filter. Finally the photoluminescence emission spectrum was collected from 370 to 600 nm using an excitation wavelength of 360 nm. The time zero emission spectrum was subtracted from each subsequent data file, as a background correction. The emission intensity at 411 nm was used to determine photoluminescence rate constant (k_{PL}) for the formation of anthracene. The experiment was conducted in triplicate for each mechanophore-containing polymer, and the rate constants were averaged and standard deviations calculated. Figure 7 shows the photoluminescence spectra for a representative run and first-order kinetic plots for $\mathbf{S}_{DA,85.9}$ and $\mathbf{L}_{DA,61.6}$.

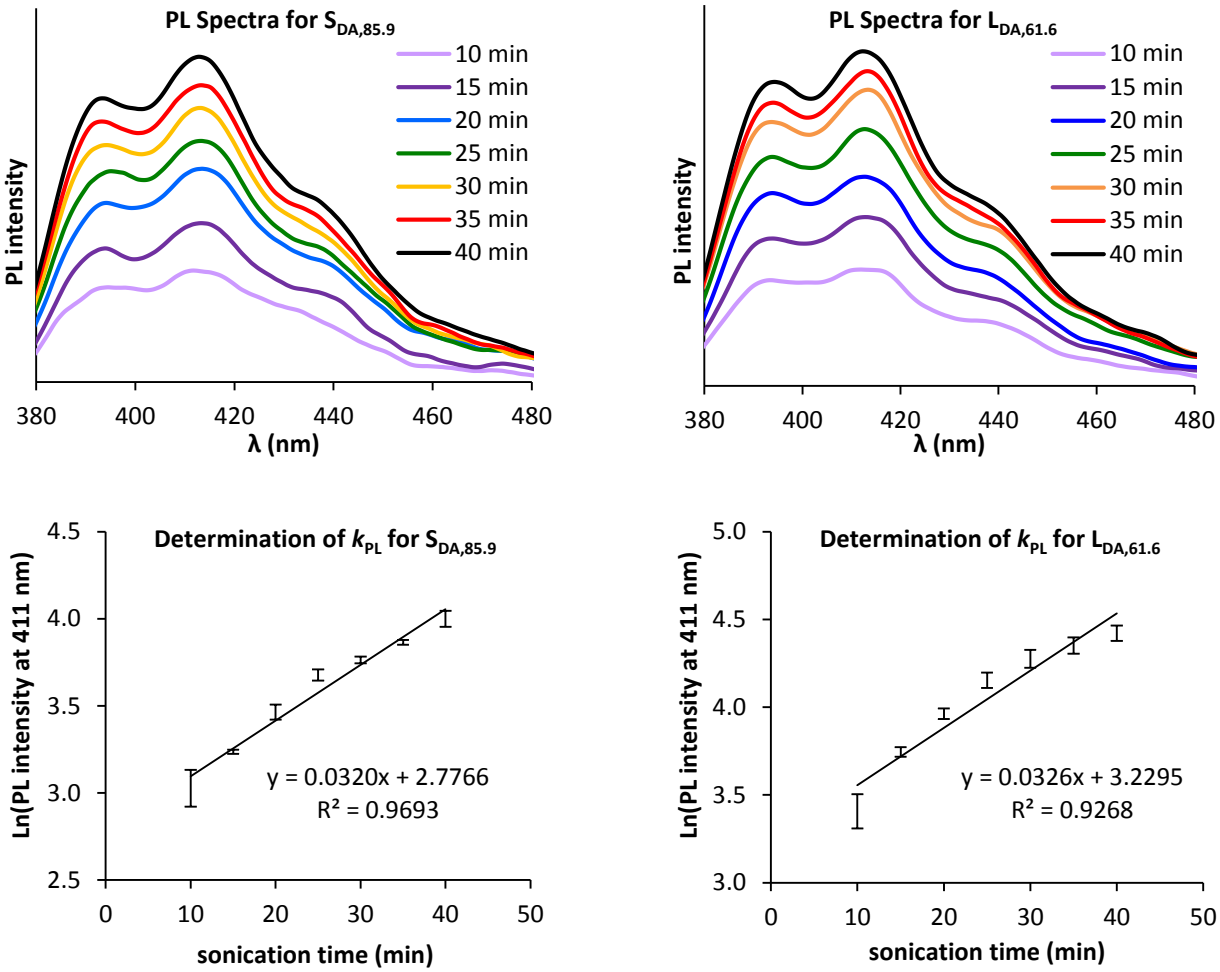

Figure 7. PL spectra and PL intensity for **S**$_{DA,85.9}$ and **L**$_{DA,61.6}$ upon increasing sonication time.

UV-vis absorption spectra were also used to confirm the formation of anthracene upon sonication of the mechanophore-containing polymers. A representative set of spectra are show in Figure 8.

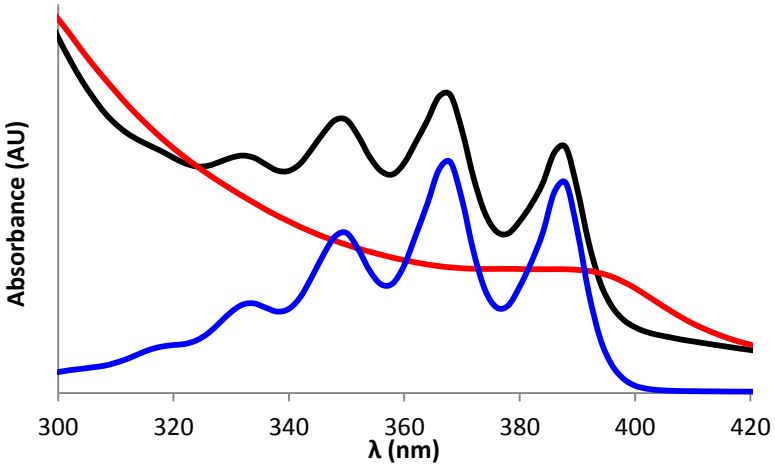

Figure 8. UV-vis absorption spectrum in DMF of **1** (blue line), and $\mathbf{S}_{DA,85.9}$ before (red line) and after (black line) sonication. The characteristic features observed in the blue and black traces are consistent with anthracene formation upon sonication of $\mathbf{S}_{DA,85.9}$.

1.4.5. Photoluminescence Control Experiments

As a sonication control experiment, a mixture of $\mathbf{L}_{p,58.7}$ (64 mg) and **1** (0.61 mg, 0.0011 mmol) in DMF (12.8 mL, 5 mg/mL polymer solution) was sonicated as described in section 1.4.3. for kinetic studies. The PL spectrum was recorded from 370 to 600 nm using an excitation wavelength of 360 nm. The total integrated emission intensity was plotted as a % of initial value versus sonication time (Figure 5C and Figure 9). These results confirm the stability of product anthracene moieties to sonication and that the UV-absorbing material formed upon degradation of unfunctionalized PMA does not influence the PL output intensities. The PL intensity at 411 nm (excitation at 360 nm) for a mixture of $\mathbf{L}_{p,58.7}$ and **1** was also recorded over a concentration range for **1** consistent with the theoretical concentrations of anthracene produced in the kinetic studies (Figure 5D and Figure 9). A linear correlation was observed.

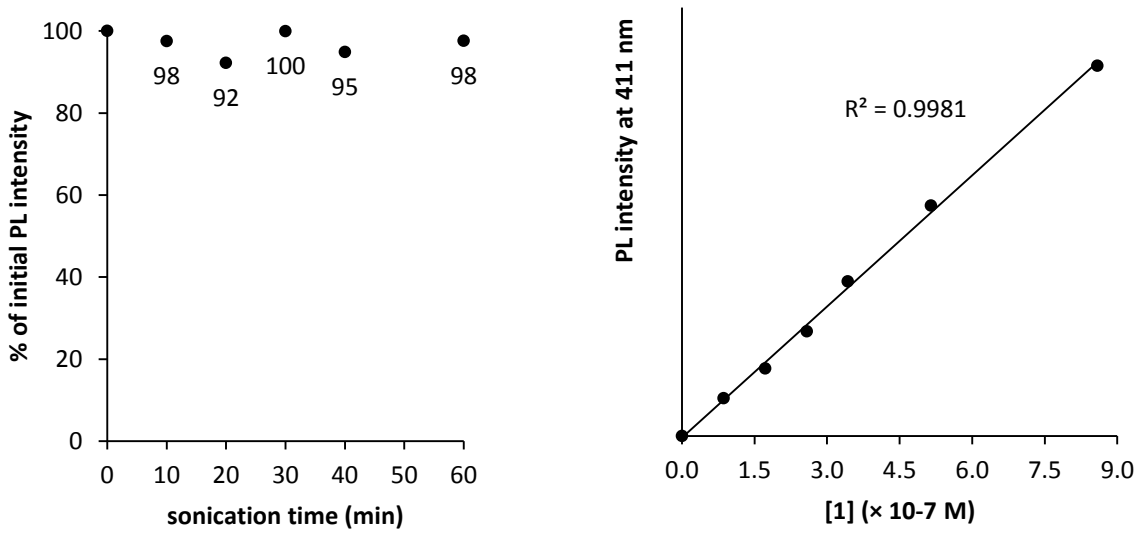

Figure 9. (left) % of initial PL intensity with increasing sonication time of a mixture of $\mathbf{L}_{p,58.7}$ and **1** in DMF, and (right) linear correlation between PL intensity and concentration of **1** in the presence of $\mathbf{L}_{p,58.7}$.

1.5. References

(1) For select reviews, see: (a) Seidel, C. A. M.; Kuhnemuth, R. *Nat. Nanotechnol.* **2014**, *9*, 64. (b) Cravotto, G.; Gaudino, E. C.; Cintas, P. *Chem. Soc. Rev.* **2013**, *42*, 7521. (c) Sepelak, V.; Duvel, A.; Wilkening, M.; Becker, K.-D.; Heitjans, P. *Chem. Soc. Rev.* **2013**, *42*, 7507. (d) Wang, G.-W. *Chem. Soc. Rev.* **2013**, *42*, 7668. (e) Gilman, J. J. *Science* **1996**, *274*, 65.

(2) For recent reviews, see: (a) Brantley, J. N.; Bailey, C. B.; Wiggins, K. M.; Keatinge-Clay, A. T.; Bielawski, C. W. *Polym. Chem.* **2013**, *4*, 3916. (b) May, P. A.; Moore, J. S. *Chem. Soc. Rev.* **2013**, *42*, 7497. (c) Wiggins, K. M.; Brantley, J. N.; Bielawski, C. W. *Chem. Soc. Rev.* **2013**, *42*, 7130. (d) Groote, R.; Jakobs, R. T. M.; Sijbesma, R. P. *Polym. Chem.* **2013**, *4*, 4846. (e) Brantley, J. N.; Wiggins, K. M.; Bielawski, C. W. *Polym. Int.* **2013**, *62*, 2. (f) Ariga, K.; Mori, T.; Hill, J. P. *Adv. Mater.* **2012**, *24*, 158. (g) Boulatov, R. *Pure Appl. Chem.* **2011**, *83*, 25. (h) Caruso, M. M.;

Davis, D. A.; Shen, Q.; Odom, S. A.; Sottos, N. R.; White, S. R.; Moore, J. S. *Chem. Rev.* **2009**, *109*, 5755. (i) Beyer, M. K.; Clausen-Schaumann, H. *Chem. Rev.* **2005**, *105*, 2921.

(3) For recent examples, see: (a) Diesendruck, C. E.; Peterson, G. I.; Kulik, H. J.; Kaitz, J. A.; Mar, B. D.; May, P. A.; White, S. R.; Martinez, T. J.; Boydston, A. J.; Moore, J. S. *Nat. Chem.* **2014**, *6*, 623. (b) Brantley, J. N.; Bailey, C. B.; Cannon, J. R.; Clark, K. A.; Vanden Bout, D. A.; Bodbelt, J. S.; Keatinge-Clay, A. T.; Bielawski, C. W. *Angew. Chem., Int. Ed.* **2014**, *53*, 5088. (c) Lee, C. K.; Diesendruck, C. E.; Lu, E.; Pickett, A. N.; May, P. A.; Moore, J. S.; Braun, P. V. *Macromolecules* **2014**, *47*, 2690. (d) Grady, M. E.; Beiermann, B. A.; Moore, J. S.; Sottos, N. R. *ACS Appl. Mater. Interfaces* **2014**, *6*, 5350. (e) Larsen, M. B.; Boydston, A. J. *J. Am. Chem. Soc.* **2014**, *136*, 1276. (f) Gossweiler, G. R.; Hewage, G. B.; Soriano, G.; Wang, Q.; Welshofer, G. W.; Zhao, X.; Craig, S. L. *ACS Macro Lett.* **2014**, *3*, 216. (g) Beiermann, B. A.; Kramer, S. L. B.; May, P. A.; Moore, J. S.; White, S. R.; Sottos, N. R. *Adv. Funct. Mater.* **2014**, *24*, 1529. (h) Chen, Y.; Zhang, H.; Fang, X.; Lin, Y.; Xu, Y.; Weng, W. *ACS Macro Lett.* **2014**, *3*, 141.

(4) For selected examples of linear polymers, see: (a) Klukovich, H. M.; Kouznetsova, T. B.; Kean, Z. S.; Lenhardt, J. M.; Craig, S. L. *Nat. Chem.* **2013**, *5*, 110. (b) Berkowski, K. L.; Potisek, S. L.; Hickenboth, C. R.; Moore, J. S. *Macromolecules* **2005**, *38*, 8975. (c) Odell, J. A.; Keller, A. *J. Polym. Sci., Polym. Phys.* **1986**, *24*, 1889. (d) Encina, M. V.; Lissi, E.; Sarasua, M.; Gargallo, L.; Radic, D. *J. Polym. Sci., Polym. Lett. Ed.* **1980**, *18*, 757. (e) Schmid, G.; Rommel, O. *Z. Physik. Chem.* **1939**, *185*, 97.

(5) For star polymers, see: (a) Duan, M.; Fang, S.; Zhang, L.; Wang, F.; Zhang, P.; Zhang, J. *e-Polym.* **2011**, *11*, 86. (b) Xue, L.; Agarwal, U. S.; Lemstra, P. J. *Macromolecules* **2005**, *38*, 8825. (c) Striegel, A. M. *J. Biochem. Biophys. Methods* **2003**, *56*, 117. (d) Kim, O. K.; Little, R. C.; Patterson, R. L.; Ting, R. Y. *Nature* **1974**, *250*, 408.

(6) For selected examples of brush/graft polymers, see: (a) Li, Y.; Nese, A.; Lebedeva, N. V.; Davis, T.; Matyjaszewski, K.; Sheiko, S. S. *J. Am. Chem. Soc.* **2011**, *133*, 17479. (b) Sheiko, S. S.; Sun, F. C.; Randall, A.; Shirvanyants, D.; Rubinstein, M.; Lee, H-i.; Matyjaszewski, K. *Nature* **2006**, *440*, 191. (c) Agarwal, U. S.; Mashelkar, R. A. *J. Non-Newtonian Fluid. Mech.* **1994**, *54*, 1.

(7) For selected examples of mechanochemistry in cross-linked networks, see: (a) Larsen, M. B.; Boydston, A. J. *J. Am. Chem. Soc.* **2013**, *135*, 8189. (b) Klukovich, H. M.; Kouznetsova, T. B.; Kean, Z. S.; Lenhardt, J. M.; Craig, S. L. *Nat. Chem.* **2013**, *5*, 110. (c) Baytekin, H. T.; Baytekin, B.; Grzybowski, B. A. *Angew. Chem., Int. Ed.* **2012**, *51*, 3596. (d) Kingsbury, C. M.; May, P. A.; Davis, D. A.; White, S. R.; Moore, J. S.; Sottos, N. R. *J. Mater. Chem.* **2011**, *21*, 8381.

(8) (a) Vijayalakshmi, S. P.; Madras, G. *Polym. Degrad. Stab.* **2005**, *90*, 116−122. (b) Kryger, M. J.; Munaretto, A. M.; Moore, J. S. *J. Am. Chem. Soc.* **2011**, *133*, 18992−18998. (c) Basedow, A. M.; Ebert, K. H. *Adv. Polym. Sci.* **1977**, *22*, 83−148. (d) Jellinek, H. H. G. *J. Polym. Sci.* **1959**, *37*, 485−497.

(9) (a) Marsalko, T. M.; Majoros, I.; Kennedy, J. P. *J. Macromol. Sci., Pure Appl. Chem.* **1997**, *34*, 775. (b) Covitch, M. *J. Soc. Automot. Eng., [Spec. Publ.] SP* **1998**, *1390*, 14.

(10) Matyjaszewski, K.; Xia, J. *Chem. Rev.* **2001**, *101*, 2921.

(11) Florea, M. *J. Appl. Polym. Sci.* **1993**, *50*, 2039.

(12) (a) Malhotra, S. L. *J. Macromol. Sci., Part A* **1986**, *23*, 729. (b) Malhotra, S. L. *J. Macromol. Sci., Part A* **1982**, *18*, 1055.

(13) (a) Konda, S. S. M.; Brantley, J. N.; Varghese, B. T.; Wiggins, K. M.; Bielawski, C. W.; Makarov, D. E. *J. Am. Chem. Soc.* **2013**, *135*, 12722. (b) Wiggins, K. M.; Syrett, J. A.; Haddleton, D. M.; Bielawski, C. W. *J. Am. Chem. Soc.* **2011**, *133*, 7180.

(14) Potisek, S. L.; Davis, D. A.; Sottos, N. R.; White, S. R.; Moore, J. S. *J. Am. Chem. Soc.* **2007**, *129*, 13808.

(15) Church, D. C.; Peterson, G. I.; Boydston, A. J. *ACS Macro Lett.* **2014**, *3*, 648.

(16) Nikitas, P.; Pappa-Louisi, A.; Papageorgiou, A. *J. Chrom. A* **2001**, *912*, 13.

Chapter 2 – Modeling the Mechanochemical Degradation of Star Polymers

2.1. Introduction

The mechanochemical degradation of polymers has received considerable attention from both the experimental and theoretical sciences.[1] This is due largely to the fact that the molecular weight distributions (MWDs) and degradation profiles of polymers undergoing mechanochemical chain scission have significant impacts on the physicochemical properties of the bulk material. For example, pharmacokinetics, bulk viscosity, and surface adhesion are properties that apply to a diverse array of applications and each depends greatly on MWD. Therefore, methods for modeling the results of mechanochemical chain scission over time can provide valuable information about the evolving properties of the polymer sample undergoing degradation. Various equations have been developed to describe the evolution of the average molecular weight (M)[2] or MWDs[3] of a linear polymer sample during degradation. Modeling of more complex polymer architectures, such as star polymers, has received much less attention. This is unfortunate considering the important advantages that star polymer architectures can afford, and their unique degradation behavior in comparison with linear counterparts.

The mechanochemical degradation of star polymers has been mostly studied in relation to their use as viscosity enhancers, as star polymers show greater shear-resistance than their linear analogues.[4] Experimentally, informative studies on the kinetics of degradation of star polymers

have been conducted.[4b,5] Existing models for star polymers include those for random (non-mechanochemical) degradation,[6] and change in the number average molecular weight (M_n)[7] and MWDs[8] upon mechanochemical degradation. For the latter model, the authors noted that discrepancies between the computationally and experimentally obtained MWDs increased with time, as the polymers underwent greater extents of chain scission and the *M* decreased.

In seeking to develop a model for accurately predicting the MWDs of star polymers undergoing mechanochemical degradation, over extended periods of time, the linear polymer degradation model developed by Glynn, van der Hoff, and Reilly emerged as an excellent entryway.[3j] In particular, the model is easily accessible for modification and, importantly, was shown to be in good agreement with the ultrasonic degradation of poly(styrene), poly(methyl acrylate) (PMA), PMA with a chain-centered mechanophore, and poly(phthalaldehyde).[9,10,11] Herein, we describe our efforts to expand this linear polymer model to be readily applicable to n-arm star polymers, and provide direct comparisons with experimental results from ultrasonic degradation of three-arm star polymers.

2.1.1. Description of the Model for Linear Polymers

Glynn et al. described the following general model for the degradation of linear polymers:[3j]

$$(N + t + 1)f_n(t + 1, x) - (N + t)f_n(t, x) = 2\left\{\sum_{y=x+1}^{\infty} P(t, y)Q(y, x)\right\} - P(t, x) \qquad (1)$$

which can be rearranged to give:

$$f_n(t + 1, x) = \frac{(N+t)f_n(t,x) - P(t,x) + 2\left\{\sum_{y=x+1}^{\infty} P(t,y)Q(y,x)\right\}}{N+t+1} \qquad (2)$$

where

$$P(t, x) = A(t)(M_\circ x)^s f_n(t, x) \qquad (3)$$

and

$$Q(y,x) = \frac{1}{ry\sqrt{2\pi}} e^{\left(-\frac{\left(x-\frac{y}{2}\right)^2}{2r^2y^2}\right)} \quad (4)$$

Descriptions for the terms in these equations can be found in Table 6. The normalization coefficient $A(t)$ must be calculated for each $P(t,x)$ distribution such that the following equation is satisfied:

$$\sum_{x=1}^{\infty} P(t,x) = 1 \quad (5)$$

This model requires that the polymer sample's degree of polymerization (DP) distribution, which can be acquired by dividing the molecular weights of the MWD by $M_\circ$, be known prior to any scission events occurring, i.e. knowing $f_n(0,x)$ for each value of x. From this initial distribution, each successive distribution, $f_n(t+1,x)$, is calculated. Multiple iterations of the calculation are completed until the desired extent of degradation has occurred.

Table 6. Description of the terms for the linear polymer degradation model.

Term	Description
t	Number of scission events
N	Number of polymer chains
x	Degree of polymerization (DP)
y	Degree of polymerization plus one $(x+1)$
$f_n(t,x)$	Number fraction for a polymer with a DP of x after t scission events
$P(t,x)$	Probability that a polymer with a DP of x will undergo scission after t scission events
$Q(y,x)$	Probability that a polymer with a DP of y will produce a polymer with a DP of x upon scission
$A(t)$	Normalization coefficient
$M_\circ$	Monomer molecular weight
s	Power constant
r	Gaussian parameter

This model assumes that the $Q(y,x)$ distribution is described by a Gaussian function symmetric with respect to the midpoint of the polymer chain, giving rise to the two in the denominator of the $\frac{y}{2}$ fraction in Equation 4. This symmetry also accounts for the factor of two in Equation 2, given that fragments with a DP of x are produced with equal probability upon rupture at a DP of x units from either end of the polymer chain. Experimentally, the mechanochemically active region of linear polymers is generally considered to be within the middle 15% of the backbone.[1g] For the model, the mechanochemically active region of each polymer chain is defined by the Guassian parameter r, as the product of r and y is equal to the standard deviation of the *Q* distribution. With small values of r (< 0.005), a center cleavage model is produced in which the distribution is so narrow that only the centermost bond in the polymer chain is susceptible to scission. With large values (> 10), a random scission model is produced, such that the distribution is so wide that the probabilities of chain scission are essentially equal for all values of y. Intermediate values provide a Gaussian cleavage model where the distribution spans most of the chain length, but the probability is still highest for scission near the center and decreases as the chain ends are approached. The Gaussian cleavage model has been shown to be in the best agreement with the mechanochemical degradation of polymers without a scissile mechanophore.[9,10]

2.1.2. Necessary Changes for Modeling Star Polymers

The MWDs described by the Gaussian cleavage model will evolve such that linear polymers will undergo scission to produce fragments of $\frac{1}{2^t}M$ (as shown in Figure 10A). One of the limitations of this model is that it does not account for the experimental observation that

mechanochemical degradation does not occur below a limiting molecular weight (M_{lim}). That is, the halving process will proceed until M is below M_{lim}, and then degradation of those chains will stop. While Glynn et al. suggested that the model could be modified to include this parameter,[3j] it was not demonstrated explicitely. It is important for a working model for the mechanochemical degradation of polymers to account for M_{lim} so as to not overestimate the amount of polymer chains being produced below M_{lim}. Additionally, probability distributions for chain scission are dependent upon the number of chains in the population. Therefore, disregarding a M_{lim} is likely to underestimate the degree of chain scission for polymer chains of higher M.

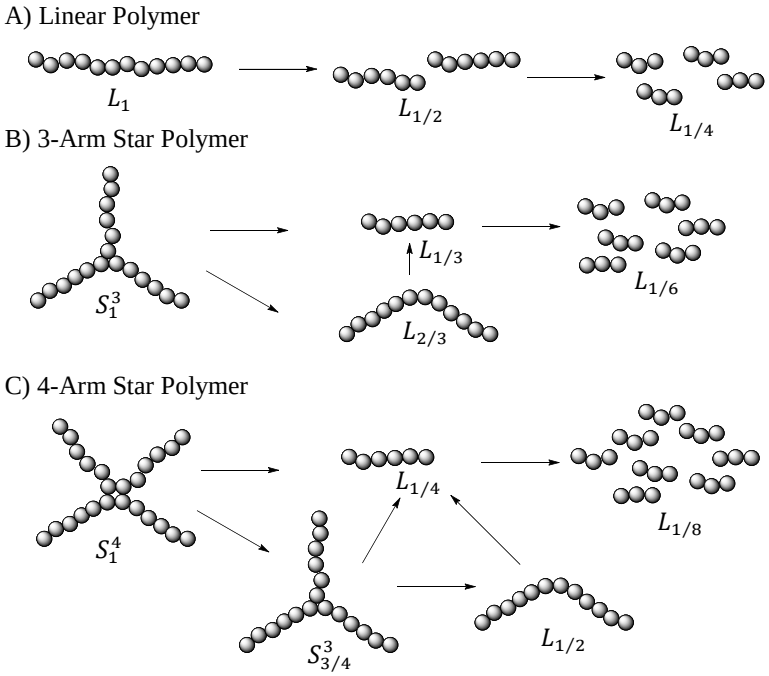

Figure 10. Generalized depiction of (A) linear, (B) three-arm star, and (C) four-arm star polymers undergoing mechanochemical degradation. L = linear architecture with the subscript indicating the fraction of the initial M. S = star architecture with the superscript indicating the number of arms and the subscript indicating the fraction of the initial M.

If we consider the simple architecture of a three-arm star polymer with equal arm lengths, the progression of its MWD upon chain-centered scission (i.e. near or at the core) will differ from its linear counterpart. A three-arm star polymer will first cleave into $\frac{2}{3}M$ and $\frac{1}{3}M$ fragments which, now having a linear structure, will cleave to $\frac{1}{3}M$ and $\frac{1}{6}M$ fragments, respectively (as shown in Figure 10B). The linear fragments would continue to be halved until the M_{lim} is reached. Thus a model for the degradation of star polymers must be able to mathematically treat the star and linear components of the distribution as individual entities that degrade differently.

2.2. Results and Discussion

2.2.1. Modifying the Linear Polymer Model

We first modified the linear polymer model to include a term for M_{lim}. This was achieved by expressing Equation 3 in the following form:

$$P(t, M) = A(t)(M - M_{lim})^s f_n(t, M) \quad (6)$$

where $A(t)$ must be calculated such that the following equation is satisfied (as described by Glynn et al.[3j]):

$$\sum_{M_{lim}}^{\infty} P(t, x) = 1 \quad (7)$$

When M is less than M_{lim}, Equation 6 will give a negative value for the probability, which was treated as a value of zero, such that the sum of all probabilities for a chain below M_{lim} to undergo scission was equal to zero.

To demonstrate how this equation could be modified for general use as a model for star polymers, we first showed how the linear polymer model can be modified such that terms representing the individual linear polymer fragments that compose the MWD are treated uniquely. For simplicity, in all further references to the linear and star polymer models, we have combined

the terms $M_\circ$ and x, such that all equations will be in terms of M rather than x. The $f_n(t+1,M)$ distribution for a linear polymer is equal to the sum of the parent and daughter MWDs. These terms are denoted by $L_z(t+1,M)$, where the subscript z indicates the fraction of the initial M (e.g., L_1 refers to the parent polymer and $L_{1/2}$ refers to a fragment equal to $\frac{1}{2}$ M). Thus, the description of the number fraction for linear polymers becomes:

$$f_n(t+1,M) = L_1(t+1,M) + L_{1/2}(t+1,M) + L_{1/4}(t+1,M) + \cdots \qquad (8)$$

Equation 2 then becomes:

$$f_n(t+1,M) = \frac{(N+t)L_1(t,M) - P_{L1}(t,M) + 2\{\sum_{y=M+1}^{\infty} P_{L1}(t,y)Q(y,M)\}}{N+t+1} +$$

$$\frac{(N+t)L_{1/2}(t,M) - P_{L1/2}(t,M) + 2\{\sum_{y=M+1}^{\infty} P_{L1/2}(t,y)Q(y,M)\}}{N+t+1} +$$

$$\frac{(N+t)L_{1/4}(t,M) - P_{L1/4}(t,M) + 2\{\sum_{y=M+1}^{\infty} P_{L1/4}(t,y)Q(y,M)\}}{N+t+1} + \cdots \qquad (9)$$

Figure 11A shows the results of using Equation 2 and Equation 9 each to calculate the $f_n(t+1,M)$ distributions for a theoretical 60 kDa linear polymer. The calculated MWDs are identical, as shown by the overlapping solid and dashed curves. This result shows that the term for the parent polymer can be isolated from those of the daughter fragments without changing the predicted MWDs, which is the first step toward expanding the model to apply to star polymers. Additionally, using Equation 9 provides the MWD for each of the individual polymer components (as in Figure 11B) which would otherwise not be easily obtained. It is important to note that for this example, the initial parent M was chosen such that the M of the $L_{1/8}$ fragments was below M_{lim}. When this is not the case, additional $L_n(t+1,M)$ terms must be added, until a fragment below M_{lim} is produced, to achieve the full extent of degradation of any single polymer chain.

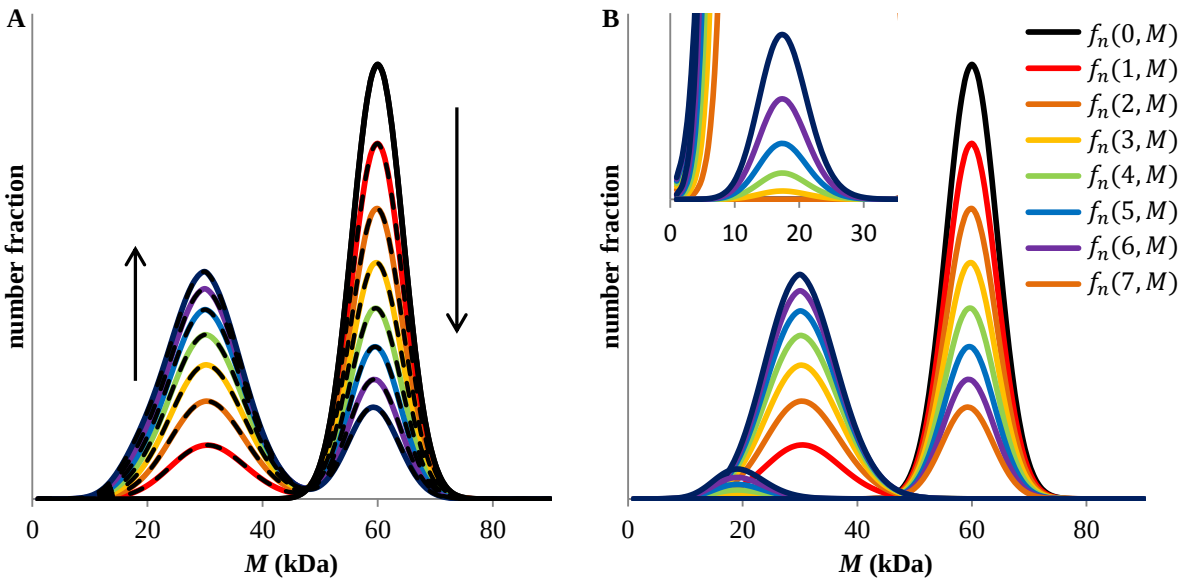

Figure 11. (A) Predicted MWDs for a theoretical 60 kDa polymer (r = 0.1, M_{lim} = 30 kDa, N = 10) by calculating $f_n(t+1,M)$ using Equation 2 (solid colored lines) and the MWDs calculated using Equation 9 (black dashed lines) up to t = 7. The arrows indicate the direction of the peak movement. (B) Predicted MWDs (with the same starting polymer and parameters) for each of the individual polymer fragments present in the left plot, $L_1(t,M)$, $L_{1/2}(t,M)$, $L_{1/4}(t,M)$, and $L_{1/8}(t,M)$, up to t = 7. Inset: plot of the $L_{1/8}(t,M)$ distributions.

2.2.2. Development of the Model for Star Polymers

For a three arm star polymer, the $f_n(t+1,M)$ MWD is the sum of the parent, $S_1^3(t+1,M)$ (where the superscript indicates the number of arms and the subscript indicates the fraction of the initial M) and daughter fragments present in the sample, $L_{2/3}(t+1,M)$, $L_{1/3}(t+1,M)$, $L_{1/6}(t+1,M)$, … (see Figure 10B). As the linear fragments can be combined to give $f_n(t+1,M)$ in the case of the linear polymer model, they can also be combined here resulting in:

$$f_n(t+1,M) = S_1^3(t+1,M) + L_n(t+1,M) \qquad (10)$$

Which can be further expanded to the following form:

$$f_n(t+1,M) =$$

$$\frac{(N+t)S_1^3(t,M) - P_{S3}(t,M) + \left\{\sum_{y=M+1}^{\infty} P_{S3}(t,y)Q_{S3_1}(y,M)\right\} + \left\{\sum_{y=M+1}^{\infty} P_{S3}(t,y)Q_{S3_2}(y,M)\right\}}{N+t+1} +$$

$$\frac{(N+t)L_n(t,M) - P_{Ln}(t,M) + 2\left\{\sum_{y=M+1}^{\infty} P_{Ln}(t,y)Q(y,M)\right\}}{N+t+1} \quad (11)$$

The *P* probability distributions in Equation 11 are further described by the following:

$$P_{S3}(t,M) = B(t)(\tfrac{2}{3}(M - M_{lim}))^s S_1^3(t,M) \quad (12)$$

and

$$P_{Ln}(t,M) = B(t)(M - M_{lim}))^s L_n(t,M) \quad (13)$$

The *Q* probability distributions in Equation 11 are further described by the following:

$$Q_{S3_1}(y,M) = \frac{1}{ry\sqrt{2\pi}} e^{\left(-\frac{\left(M-\frac{y}{3/2}\right)^2}{2r^2y^2}\right)} \quad (14)$$

and

$$Q_{S3_2}(y,M) = \frac{1}{ry\sqrt{2\pi}} e^{\left(-\frac{\left(M-\frac{y}{3}\right)^2}{2r^2y^2}\right)} \quad (15)$$

Equations 12 and 13 share a new normalization coefficient $B(t)$ which must be calculated such that the following equation is satisfied:

$$\sum_{M_{lim}}^{\infty} P_{S3}(t,M) + \sum_{M_{lim}}^{\infty} P_{Ln}(t,M) = 1 \quad (16)$$

It has been proposed that the degradation of star polymers, via ultrasound-induced caviation, is dependent upon its spanning molecular weight (M_{span}), which is equal to two times the arm molecular weight (M_{arm}).[5,12] Therefore, Equation 12 has an additional $\frac{2}{3}$ factor to account for the M_{span} of a three-arm star polymer, which is effectively $\frac{2}{3}M$. The first fraction on the right hand side of Equation 11 is equal to $S_1^3(t+1,M)$ and the second fraction is equal to $L_n(t+1,M)$. The two summations are required for the $S_1^3(t+1,M)$ component of Equation 10 because two different *M*s are being produced from a single scission of a star polymer, each requiring a unique *Q* probability

distribution. Equations 14 and 15 differ by the denominator of the $\frac{y}{j}$ term. The $Q_{S3_1}(y, M)$ distribution leads to the production of $\frac{2}{3}$ M fragments using a j value of $\frac{3}{2}$ and the $Q_{S3_1}(y, M)$ distribution leads to the production of $\frac{1}{3}$ M fragments using a j value of 3. As is the case for the linear polymer model, the new MWDs after t scission events can be derived from the initial MWD.

2.2.3. Comparison of Models with Experimental Data

We initially modeled a 36 kDa linear polymer to verify that the inclusion of the M_{lim} term into the Glynn et al. model still produced MWDs that were in good agreement with experimental results. First, the plot for the virgin polymer (0 min plot in Figure 12A) was fit with a polynomial modified Gaussian function,[13] which was then used to produce the $f_n(0, M)$ distribution at 1 kDa intervals. The predicted MWDs were determined with the Glynn et al. model using Equation 6 (Figure 12B) and Equation 3 (Figure 12C), separately. A value of N was chosen such that the $f_n(20, M)$ distribution obtained when using Equation 6 most closely resembled the 100 min plot of the experimental data, thus facilitating comparison of the distributions. Each of the parameters were kept the same when modeling with either equation, except the M_{lim}. The predicted MWDs using Equation 6 are in good agreement with the experimental results. The predicted MWDs using Equation 3 have a substantial amount of the ca. 20 kDa fragments degrading to give ca. 10 kDa fragments, which was not observed experimentally. For instance, the gel permeation chromatography (GPC) chromatogram for the 36 kDa polymer, after 180 min of sonication, does not show the appearance of a new peak that would correspond to ca. 10 kDa fragments and a M_{n} below 9 kDa is not calculated by the multi-angle laser light scatter (MALS) detector (Figure 13). The extent of degradation of the parent polymer was less when Equation 3 was used over the same number of scission events, as the probability of a scission event occurring in the parent chains is

decreased (see Equation 5). Overall, these results demonstrate the importance of incorporating the M_{lim} term.

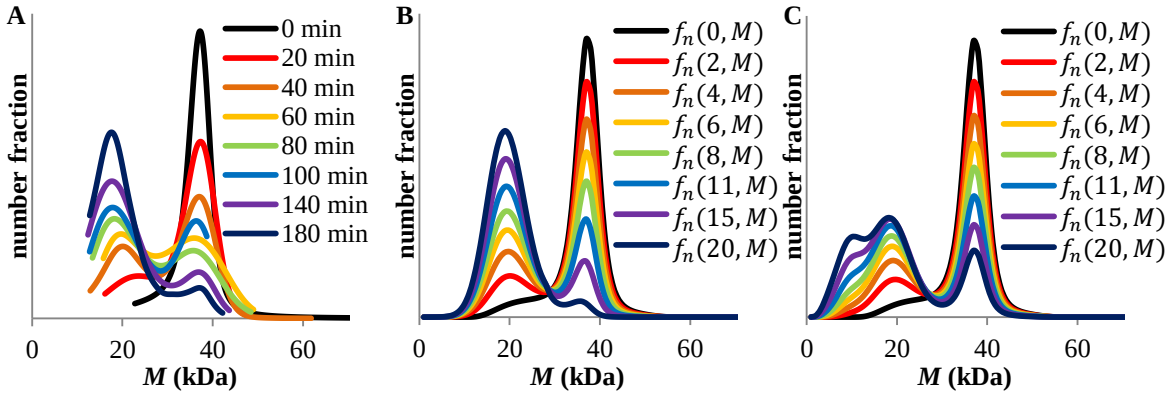

Figure 12. (A) Number fraction plots for a 36 kDa linear PMA undergoing ultrasonic degradation at various time points; (B) Predicted MWDs for the same polymer using the Glynn et al. model modified with Equaiton 6 (r = 0.1, M_{lim} = 28 kDa, N = 25); (C) Predicted MWDs for the same polymer using the unmodified Glynn et al. model, i.e. using Equation 3 (r = 0.1, N = 25).

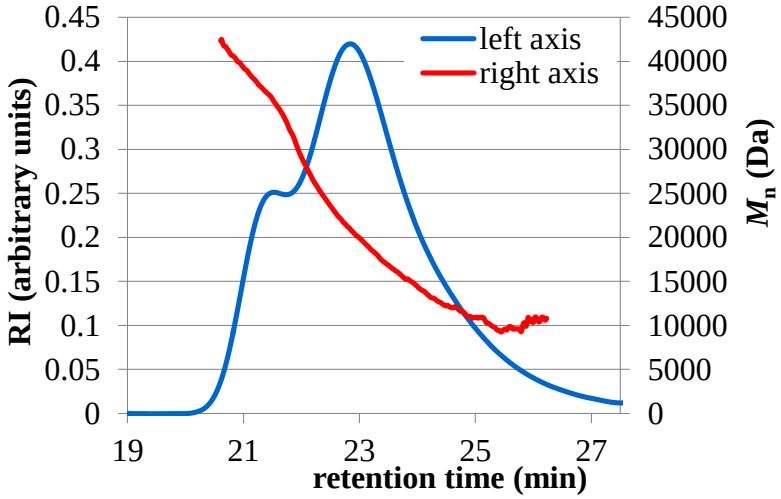

Figure 13. RI and M_n versus retention time for the 36.2 kDa linear polymer after 180 min of sonication.

We next modeled the distributions of the 86 and 62 kDa star polymers (Figure 14B and Figure 14D). The $f_n(0, M)$ distributions were calculated in the same manner as for the linear 36 kDa PMA, except that for the 86 kDa polymer the distribution was calculated in 2 kDa increments. As shown in Figure 14, the predicted MWDs for both star polymers are visually in good agreement with the experimental findings. Additionally, as shown in Figure 15, the predicted M_n for each MWD closely matches those of the experimental results for each polymer. Molecular weight comparisons were made assuming that each sequential $f_n(t, M)$ distribution corresponded to about 5 or 9 min of sonication time for the 86 and 62 kDa polymers, respectively.

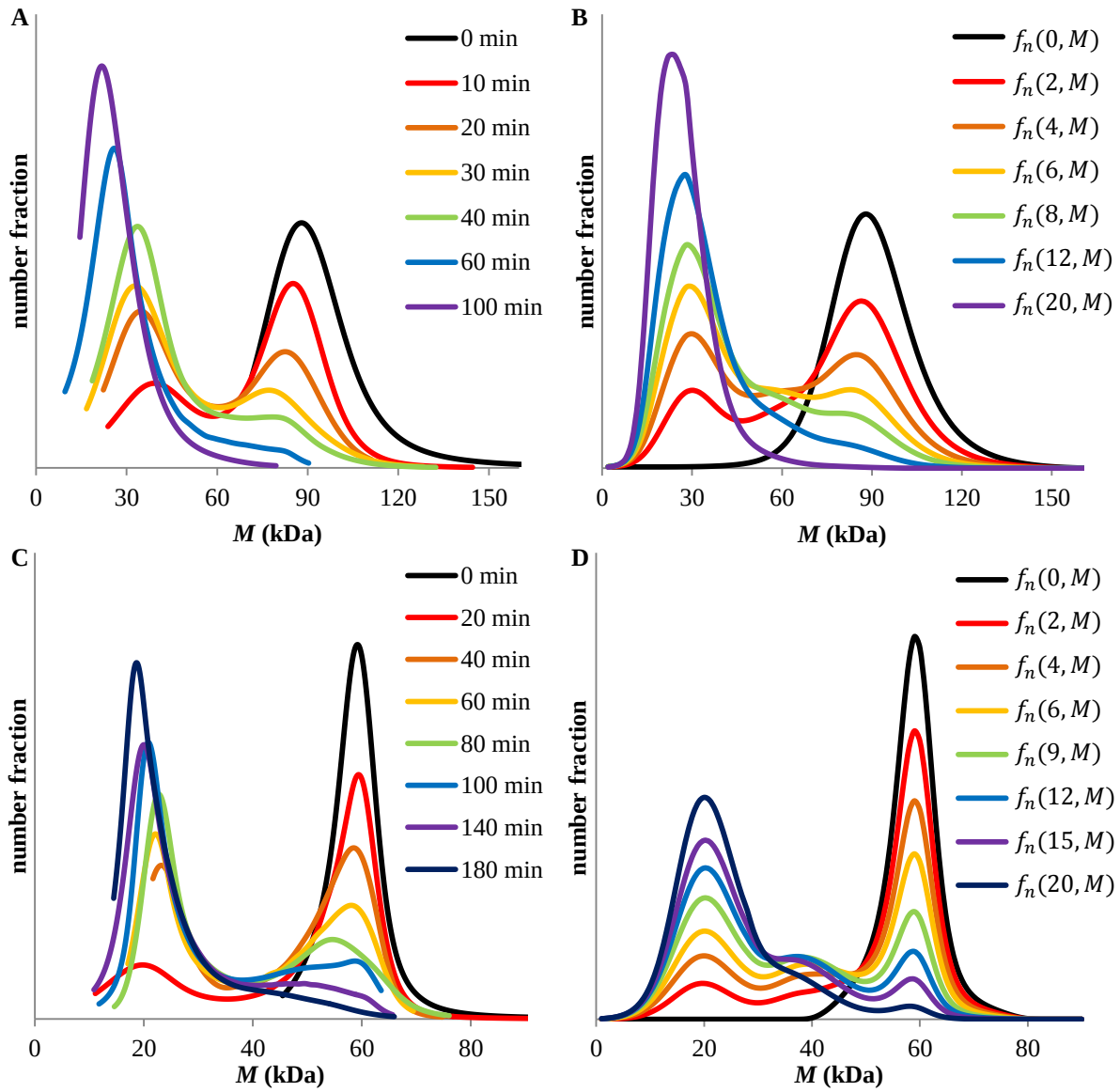

Figure 14. (A) Number fraction plots for a 86 kDa PMA undergoing ultrasonic degradation at various time points; (B) Predicted MWDs for the same polymer using the three-arm degradation model (r = 0.1, M_{lim} = 28 kDa, N = 8); (C) Number fraction plots for a 62 kDa PMA undergoing ultrasonic degradation at various time points; (D) Predicted MWDs for the same polymer using the three-arm degradation model (r = 0.1, M_{lim} = 28 kDa, N = 14).

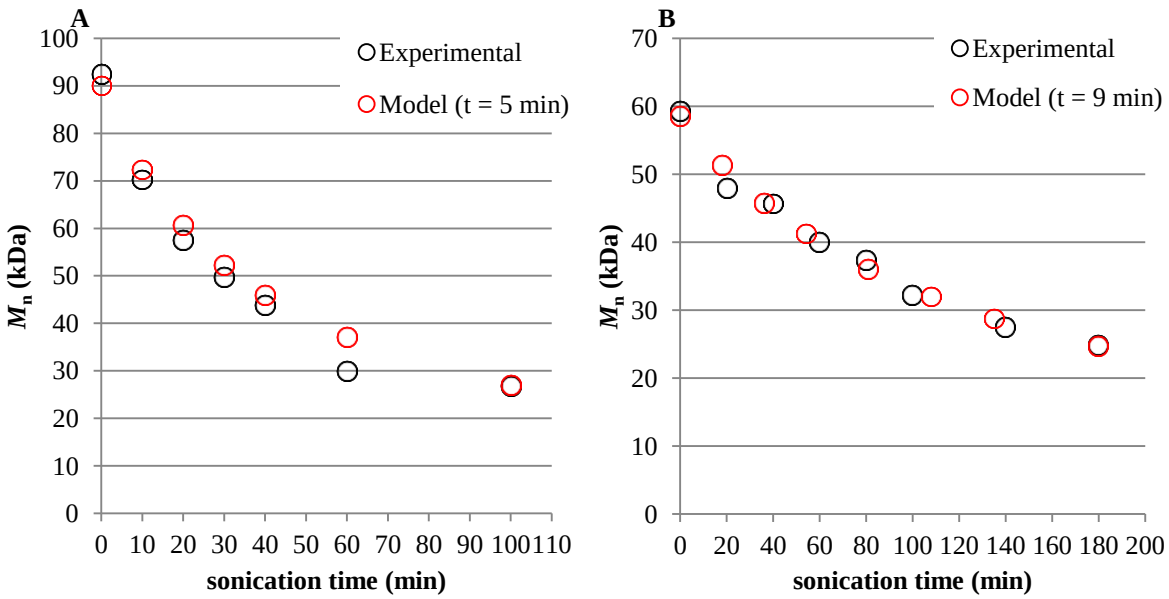

Figure 15. Experimental and predicted M_n values for the ultrasonic degradation of (A) a 86 kDa three-arm star polymer and (B) a 62 kDa three-arm star polymer. The predicted M_n values were calculated from the $f_n(t, M)$ distributions assuming that t corresponded to approximately 5 min (for the 86 kDa star polymer) or 9 min (for the 62 kDa star polymer) of sonication time.

For the unmodified linear polymer model, it was reported that large values of N were not needed to produce consistent MWD predictions.[3j] Glynn et al. observed that increasing N from 25 to 100 did not significantly change the predicted distributions. For the 86 kDa star polymer modeled in Figure 9, 83% parent degradation is predicted after 25 scission events when N = 25, versus 100% degradation after 20 scission events when N = 8. Being able to use lower values of N is advantageous, especially when using computational programs such as Microsoft Excel to assist with the modeling, as it requires calculating lower numbers of scission events. In order to determine the effects of decreasing the value of N on the predicted MWD, we examined the $t = \frac{1}{2}N$ distributions of the 86 kDa star polymer for various values of N, as shown in Figure 16A.

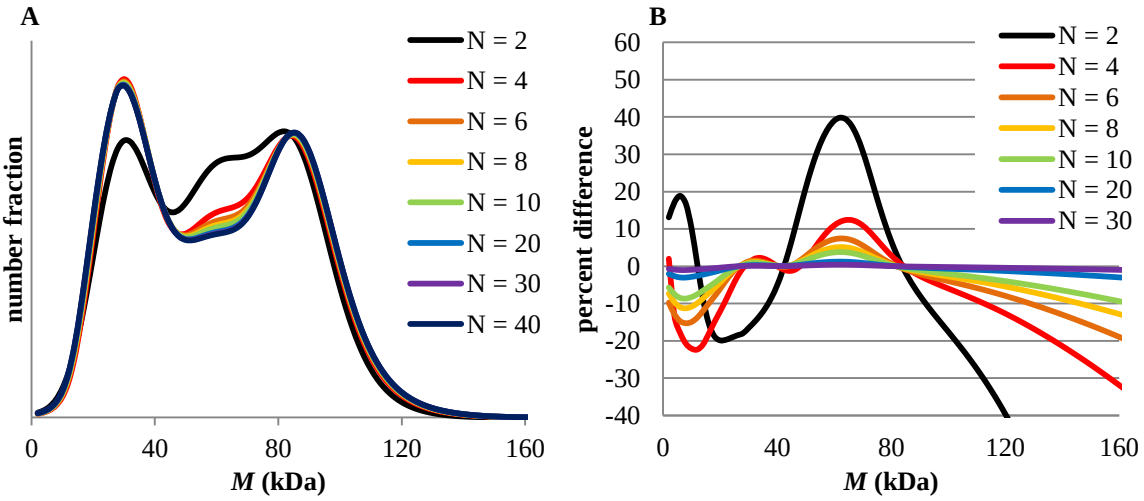

Figure 16. (A) The $t = \frac{1}{2}N$ MWDs for various values of N for the degradation of a 86 kDa star polymer; (B) The percent difference of the $t = \frac{1}{2}N$ plot for a given N value from the $t = \frac{1}{2}N$ plot when N = 40.

Visually, the predicted distributions are in good agreement when $N \geq 6$. In order to quantify the similarity between the predicted $t = \frac{1}{2}N$ distributions, the percent difference of each distribution from the N = 40 distribution was calculated. As shown in Figure 16B, the N = 30 distribution is almost identical and the deviation increases with a decreasing value of N. However, the N = 6 distribution has less than a 10% difference from the N = 40 distribution for M values of ca. 18 to 130 kDa. The N = 8 distribution (the value that was used for the 86 kDa star polymer in Figure 14) has a difference of 5% or less from the N = 40 distribution for M values of ca. 18 to 118 kDa. The percent difference does begin to substantially increase at the boundaries of the distributions, but this is largely amplified by the low values of the number fractions at these points, and thus would not be expected to significantly change the predicted MWDs or M_n values.

2.2.4. Extension to Four- and n-Arm Models.

For a four-arm star polymer, the $f_n(t+1,M)$ distribution is given by the sum of the parent four-arm polymer, $S_1^4(t+1,M)$, a three-arm daughter fragment, $S_{3/4}^3(t+1,M)$, and the linear daughter fragments present in the sample, $L_{1/2}(t+1,M)$, $L_{1/4}(t+1,M)$, $L_{1/8}(t+1,M)$, … (see Figure 10C). Thus the total MWD after *t* scission events is described by the following:

$$f_n(t+1,M) =$$

$$\frac{(N+t)S_1^4(t,M) - P_{S4}(t,M) + \left\{\sum_{y=M+1}^{\infty} P_{S4}(t,y)Q_{S4_1}(y,M)\right\} + \left\{\sum_{y=M+1}^{\infty} P_{S4}(t,y)Q_{S4_2}(y,M)\right\}}{N+t+1} +$$

$$\frac{(N+t)S_{3/4}^3(t,M) - P_{S3}(t,M) + \left\{\sum_{y=M+1}^{\infty} P_{S3}(t,y)Q_{S3_1}(y,M)\right\} + \left\{\sum_{y=M+1}^{\infty} P_{S3}(t,y)Q_{S3_2}(y,M)\right\}}{N+t+1} +$$

$$\frac{(N+t)L_n(t,M) - P_{Ln}(t,M) + 2\left\{\sum_{y=M+1}^{\infty} P_{Ln}(t,y)Q(y,M)\right\}}{N+t+1} \qquad (17)$$

Since the M_{span} for the 4-arm polymer is given by two of the arms, the probability distribution $P_{s4}(t,M)$ must include a $\frac{1}{2}$ factor (as opposed to the $\frac{2}{3}$ factor for the three-arm star polymer). A new normalization coefficient is needed such that the probabilities $P_{S4}(t,M)$, $P_{S3}(t,M)$, and $P_{Ln}(t,M)$ sum to unity. Additionally, the Q_{S4} distributions are equal to:

$$Q_{S4_1}(y,M) = \frac{1}{ry\sqrt{2\pi}} e^{\left(-\frac{\left(M-\frac{y}{4/3}\right)^2}{2r^2y^2}\right)} \qquad (18)$$

and

$$Q_{S4_2}(y,M) = \frac{1}{ry\sqrt{2\pi}} e^{\left(-\frac{\left(M-\frac{y}{4}\right)^2}{2r^2y^2}\right)} \qquad (19)$$

These modified *Q* distributions lead to the production of $\frac{3}{4}$ and $\frac{1}{4}$ *M* fragments. Figure 17 shows the predicted MWDs of a theoretical 75 kDa four-arm star polymer undergoing degradation.

In order to expand this model to other star polymers having arms of equal length, the following general formula is provided:

$$f_n(t+1,M) =$$

$$\left\{\sum_{a=3}^{n} \frac{(N+t)S^a(t,M) - P_{Sa}(t,M) + \left\{\sum_{y=M+1}^{\infty} P_{Sa}(t,y)Q_{Sa_1}(y,M)\right\} + \left\{\sum_{y=M+1}^{\infty} P_{Sa}(t,y)Q_{Sa_2}(y,M)\right\}}{N+t+1}\right\} +$$

$$\frac{(N+t)L_n(t,M) - P_{Ln}(t,M) + 2\left\{\sum_{y=M+1}^{\infty} P_{Ln}(t,y)Q(y,M)\right\}}{N+t+1} \quad (20)$$

Here, n and a are the number of arms and the Q_{Sa} distributions are equal to:

$$Q_{Sa_1}(y,M) = \frac{1}{ry\sqrt{2\pi}} e^{\left(-\frac{\left(M-\frac{y}{\left(\frac{a}{a-1}\right)}\right)^2}{2r^2y^2}\right)} \quad (21)$$

and

$$Q_{Sa_2}(y,M) = \frac{1}{ry\sqrt{2\pi}} e^{\left(-\frac{\left(M-\frac{y}{a}\right)^2}{2r^2y^2}\right)} \quad (22)$$

The P_{Sa} distribution is equal to:

$$P_{Sa}(t,M) = C(t)\left(\tfrac{2}{a}(M - M_{lim})\right)^s S_a(t,M) \quad (23)$$

Each P distribution needs the same normalization coefficient, $c(t)$, such that the sum of all P distributions equals unity. We anticipate that this model will be able to accurately predict the MWDs of n-arm star polymer degradation.

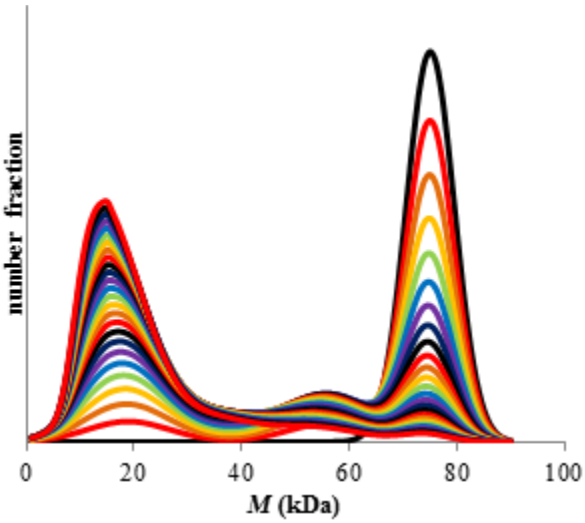

Figure 17. Predicted $f_n(t, M)$ distributions, up to t = 25, for a theoretical 75 kDa four-arm star polymer undergoing mechanochemical degradation (r = 0.1, M_{lim} = 30 kDa, N = 10).

2.3. Conclusions

We have developed a model to predict the MWDs of star polymers with equal length arms undergoing mechanochemical degradation. We initially showed that the Glynn et al. model could be easily modified to include a M_{lim} term. This modification enabled prediction of MWDs for a 36 kDa linear PMA that were in good agreement with the experimental distributions. The three-arm model was also shown to produce MWDs that were consistant with the experimental distributions for 62 and 86 kDa star polymers. For each example, the evolution of the M_n was also in accord with the experimental values. Expansion of the model to four-arm star polymers was also demonstrated and the equations for n-arm star polymers were described. Furthermore, we demonstrated that low values of N could be used, thus requiring fewer iterations of calculations and enabling the use of user-friendly computational software such as Microsoft Excel. These features demonstrate that the model is an attractive option for modeling the mechanochemical degradation of star polymers and should be readily accessible to a broad audience.

2.4. Experimental

2.4.1. Synthesis of Star and Linear Polymers

Two three-arm PMA star polymers were prepared by atom transfer radical polymerization (ATRP) as reported previously (with tetrahedral cores, as in Figure 2).[12] The molecular weights of the samples were 61.6 kDa (M_n) and 85.9 kDa with PDIs of 1.03 and 1.02, respectively. A linear 36.2 kDa (PDI = 1.03) PMA was also prepared.

2.4.2. Sonication Experiments

Sonication experiments were carried out in a flame-dried, N_2-purged Suslick flask attached to a sonication horn (1 cm diameter). Each arm of the Suslick flask was fitted with a rubber septum. In a separate flame-dried round bottom flask, the polymer sample was dissolved in dry DMF at a concentration of 5 mg/ml. The polymer solution was transferred to the Suslick flask under dry N_2 via syringe. The entire apparatus (sonication horn + Suslick flask) was then transferred to a cold room (4 °C) for the duration of the sonication experiment. Polymer solutions were sonicated at 13.8 W/cm^2 with a pulse cycle of 1 s on, 9 s off using a 20 kHz Vibra-Cell Ultrasonic Processor. Aliquots of 0.5 mL were withdrawn from the reaction at specific time points and analyzed by GPC.

2.4.3. Characterization

The GPC setup consisted of a Shimadzu pump, three in-line MZ-Gel 10 μm size-exclusion columns (10^3, 10^3, and 10^5 Å), DAWN-HELEOS II 18-angle MALS and OptiLab T-rEx refractive index detectors (each from Wyatt Technologies Corporation), and an Agilent Technologies UV-vis detector. The mobile phase consisted of 0.01 M LiBr in DMF. No calibration standards were

used, and dn/dc values were obtained for each injection assuming 100% mass elution from the columns. Differential number fraction plots were generated for each time point for comparison against the modeled distributions.

2.4.4. Modeling

All calculations were completed using Microsoft Excel 2010. A macro was written to solve for the normalization coefficients for each *P* distribution after any of the variables for the model were changed. The input data for each model consists of the values for s, r, M_{lim}, N, and $f_n(0, M)$ at discrete *M* intervals. The s exponent in the *P* distributions was set to a value of one. In all cases a value of 0.1 was used for r. A M_{lim} of 28 kDa was found to provide MWDs that best matched the experimental data. This value is consistent with literature values of M_{lim}.[1g] N values between 8 and 25 were used. For the 62 and 86 kDa star polymers, 1 and 2 kDa intervals were used to describe the $f_n(0, M)$ distributions, respectively. Larger *M* intervals helped to minimize the calculation time and simplify setting up the equations in Excel. This simplification is in accord with those made by Glynn et al.[3j]

2.5. References

(1) For recent reviews, see: (a) Brantley, J. N.; Bailey, C. B.; Wiggins, K. M.; Keatinge-Clay, A. T.; Bielawski, C. W. *Polym Chem.* **2013**, *4*, 3916. (b) May, P. A.; Moore, J. S. *Chem. Soc. Rev.* **2013**, *42*, 7497. (c) Wiggins, K. M.; Brantley, J. N.; Bielawski, C. W. *Chem. Soc. Rev.* **2013**, *42*, 7130. (d) Brantley, J. N.; Wiggins, K. M.; Bielawski, C. W. *Polym. Int.* **2012**, *62*, 2. (e) Ariga, K.; Mori, T.; Hill, J. P. *Adv. Mater.* **2012**, *24*, 158. (f) Boulatov, R. *Pure Appl. Chem.* **2011**, *83*, 25. (g) Caruso, M. M.; Davis, D. A.; Shen, Q.; Odom, S. A.; Sottos, N. R.; White, S. R.; Moore, J. S.

Chem. Rev. **2009**, *109*, 5755. (h) Beyer, M. K.; Clausen-Schaumann, H. *Chem. Rev.* **2005**, *105*, 2921.

(2) (a) Akyuz, A.; Catalgil-Giz, H.; Giz, A. T. *Macromol. Chem. Phys.* **2008**, *209*, 801. (b) Tang, S.-Y.; Liu, D.-Z. *Adv. Tech. Mat. Mat. Proc. J.* **2006**, *8*, 180. (c) Vijayalakshmi, S. P.; Madras, G. *Polym. Degrad. Stab.* **2005**, *90*, 116. (d) Madras, G.; Chattopadhyay, S. *Polym. Degrad. Stabil.* **2001**, *71*, 273. (e) Malhotra, S. *J. Macromol. Sci., Part A* **1982**, *18*, 1055. (f) Harrington, R. E.; Zimm, B. H. *J. Phys. Chem.* **1965**, *69*, 161. (g) El'tsefon, B. S.; Berlin A. A. *Polym. Sci. U.S.S.R.* **1964**, *5*, 668. (h) F. Rodriguez, C. C. Winding, *Ind. Eng. Chem.* **1959**, *51*, 1281 (i) Ovenall, D. W.; Hastings, G. W.; Allen, P. E. M. *J. Polym. Sci.* **1958**, *33*, 207.

(3) (a) Lin, Z.-L.; Luo, J.; Chen, Z.-J.; Tu, K.-H.; Wang, L.-Q.; Wang, Y.-W. *Chin. J. Polym. Sci.* **2013**, *31*, 1056. (b) Iedema, P. D. *Polymer* **2011**, *52*, 3537. (c) Tobita, H. *Macromol. React. Eng.* **2010**, *4*, 333. (d) Yeow, Y. L.; Guan, B. G.; Wu, L.; Yap, T.-M.; Leong, Y.-K. *AIChE J.* **2008**, *54*, 2699. (e) Bose, S. M.; Git Y. *Macromol. Theory Simul.* **2004**, *13*, 453. (f) Giz, A. T.; Catalgil-Giz, M. S. *Macromol. Theory Simul.* **2001**, *10*, 117. (g) Nguyen, T. Q. *Polym. Degrad. Stabil.* **1994**, *46*, 99. (h) Doulah, M. S. *J. Appl. Polym. Sci.* **1978**, *22*, 1735. (i) van der Hoff, B. M. E.; Gall, C. E. *J. Macromol. Sci., Part A: Chem.* **1977**, *11*, 1739. (j) Glynn, P. A. R.; Van Der Hoff, B. M. E.; Reilly, P. M. *J. Macromol. Sci.-Chem.* **1972**, *6*, 1653.

(4) (a) Duan, M.; Fang, S.; Zhang, L.; Wang, F.; Zhang, P.; Zhang, J. *e-Polymers* **2011**, *11*, 1618. (b) Xue, L.; Agarwal, U. S.; Lemstra, P. J. *Macromolecules* **2005**, *38*, 8825. (c) Kim, O. K.; Little, R. C.; Patterson, R. L.; Ting, R. Y. *Nature (London)* **1974**, *250*, 408.

(5) Striegel, A. M.; *J. Biochem. Biophys. Methods* **2003**, *56*, 117.

(6) Tobita, H. *Macromolecules* **1996**, *29*, 3000.

(7) Zhu, S.; Li, D.; Yu, Q.; Hunkeler, D. *J. Macromol. Sci., Part A: Pure Appl. Chem.* **1998**, *35*, 33.

(8) Kudish, I. I.; Airapetyan, R. G.; Hayrapetyan, G. R.; Covitch, M. J. *Tribology Trans.* 2005, 48, 176.

(9) Glynn, P. A. R.; van der Hoff, B. M. E. *J. Macromol. Sci., Chem.* **1973**, *A7*, 1965.

(10) Kryger, M. J.; Ong, M. T.; Odom, S. A.; Sottos, N. R.; White, S. R.; Martinez, T. J.; Moore, J. S. *J. Am. Chem. Soc.* **2010**, *132*, 4558.

(11) Diesendruck, C. E.; Peterson, G. I.; Kulik, H. J.; Kaitz, J. A.; Mar, B. D.; May, P. A.; White, S. R.; Martinez, T. J.; Boydston, A. J.; Moore, J. S. *Nat. Chem.* **2014**, *6*, 623.

(12) Church, D. C.; Peterson, G. I.; Boydston, A. J. *ACS Macro Lett.* **2014**, *3*, 648.

(13) Nikitas, P.; Pappa-Louisi, A.; Papageorgiou, A. *J. Chrom. A* **2001**, *912*, 13.

Chapter 3 – Kinetic Analysis of Mechanochemical Chain Scission of Linear Poly(phthalaldehyde)

3.1. Introduction

Polymer architectures have the ability to channel elongational forces to the chain midpoint where bond scission occurs if the forces are great enough.[1,2] In most cases, two half-chain polymer fragments are generated, and these newly formed chain ends are capable of subsequent reaction.[1] It was recently demonstrated that ultrasound-induced cavitation could be used to mechanochemically trigger the depolymerization of a low-ceiling temperature (T_c) polymer.[3] Specifically, when solutions of poly(phthalaldehyde) (PPA) were subjected to ultrasound, reactive hemiacetalate and oxocarbenium end groups were formed and rapid and complete depolymerization to monomer was observed above its T_c of -40 °C.[4,5] As the depolymerization is rapid after backbone scission, lower molecular weight polymer fragments were not observed during the course of the sonication experiments. While future applications may manifest from the ability to reconfigure materials between polymer and monomer in a cyclic fashion, the absence of macromolecular daughter fragments in the degradation of PPA may also be advantageous for studying fundamental concepts such as kinetic parameters of mechanochemical chain scission.

Methods for assessing rates of chain scission typically involve monitoring the change in average polymer molecular weight over time during sonication. These methods generally involve polymers that are cleaved into two half-molecular weight daughter fragments that contribute to the

overall average molecular weight of the sample. Importantly, degradation of the daughter fragments can continue until they reach a limiting molecular weight (M_{lim}), below which elongational forces are not great enough to induce bond cleavage. Methods developed by Malhotra have been used to determine scission rates,[6] however the method can be unreliable for high molecular weight or star polymers in which the daughter fragments have molecular weights > M_{lim}. For these larger polymers, secondary chain scission events can manifest an over-approximation of scission rates for the parent polymer, since the average molecular weight is reduced not only by cleavage of the parent polymer, but also by cleavage of any of the daughter fragments. Alternatively, the decrease in polymer concentration over time for the incipient portions of the chromatographic peaks in gel permeation chromatography (GPC) can be used to determine scission rates.[7] This approach, however, requires adequate resolution of the half-molecular weight fragments from the parent polymer and may give inconsistent results depending upon the polydispersity of the sample and chromatography conditions. To our knowledge, a low T_c polymer that depolymerizes upon chain scission, thus precluding half-molecular weight fragments and the problems associated with the previously described methods, has not been used to study the kinetics of mechanochemical degradation. We envisioned that PPA would be ideal for such an application, and that by using a polydisperse sample we could examine scission rates for a range of molecular weights from a single sonication experiment.

Molecular weight is one of the principle polymer characteristics that contribute to the force that is generated upon elongation in a flow field. For ultrasound-induced cavitation studies, some experimental results indicate a linear relationship between molecular weight and chain scission rate for molecular weights between M_{lim} and ca. 150 kDa.[8] Other studies, however, have shown an exponential relationship.[7,9] Herein, we report the ultrasound-induced chain scission of PPA to

study the kinetics of mechanochemical scission without complications from daughter fragments, and the use of chain-end trapping agents to modify depolymerization profiles.

3.2. Results and Discussion

To explore the kinetics of linear PPA degradation, we prepared linear polymer via phosphazine super base mediated polymerization.[4b,10] We initially investigated the ultrasonic degradation of PPA in dimethylformamide (DMF) using an ultrasound power density of 13.7 W/cm^2 and an internally monitored temperature between 10 and 15 °C. As shown in Figure 18, we observed a gradual decrease in PPA concentration and number average molecular weight (M_n) as a function of sonication time for 32 kDa PPA (PDI = 1.6). As a control, we found PPA to show negligible change in molecular weight over the same time period and conditions when ultrasound irradiation was not applied. Additionally, as previsouly reported,[3] sonication of 3.5 kDa PPA (PDI = 1.2), which is below M_{lim}, showed no signs of degradation after 60 min of sonication time. These experiments confirmed the mechanical origins of the initiating chain scission, and specifically rule out the possibility of thermal activation.

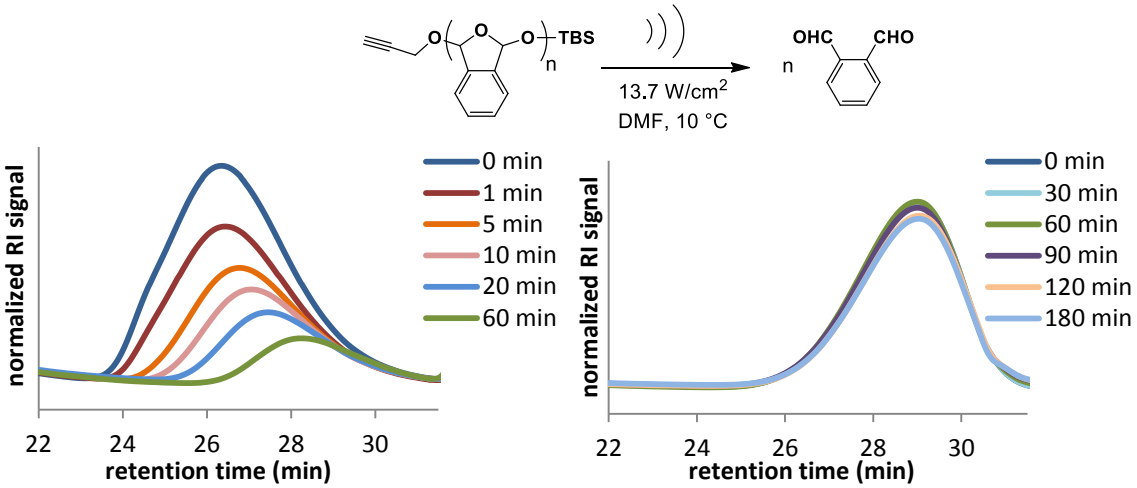

Figure 18. GPC traces of (left) 32 kDa PPA and (right) 3.5 kDa PPA with increasing sonication time. Times indicate total "on time" of ultrasound using a duty cycle of 1 s on, 9 s off. A 200 kDa polystyrene internal standard (3.0 mg/mL) was added to each sample prior to injection for RI normalization and retention time referencing.

We next determined rate constants for activation as a function of PPA molecular weight. The absence of lower molecular weight byproducts, combined with the sonication of a polydisperse sample, enabled us to determine rate constants of activation for multiple molecular weight ranges from a single sonication experiment. For kinetic studies, we prepared and analyzed a PPA sample with M_n = 27 kDa and PDI = 1.5. Sectional analysis using 5 kDa ranges between 35 and 75 kDa was performed on each GPC trace taken throughout the sonication experiment, using the area of each section (determined by RI signal intensity) as an indication of residual PPA of the corresponding M_n. First-order plots were prepared for each M_n (Figure 19). A linear dependence of the rate constant on molecular weight was observed over the range of 35 to ca. 65 kDa.

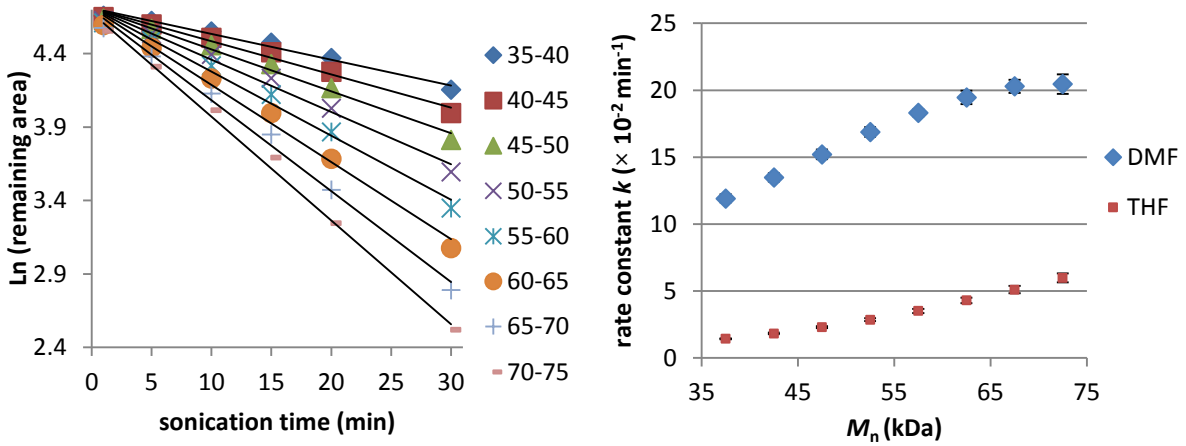

Figure 19. (left) Representative example of a set of first-order plots for molecular weight sections analyzed via GPC. The R^2 values for each M_n range are as follows: 35-40, 0.9817; 40-45, 0.9826; 45-50, 0.984; 50-55, 0.9856; 55-60, 0.9876; 60-65, 0.99; 65-70, 0.9929; 70-75, 0.9956. (right) Plot of rate constant vs M_n (average of three runs with error bars indicating one standard deviation).

To investigate the solvent dependence of mechanochemical scission rate constants, we analyzed PPA samples that were sonicated in THF and CH_2Cl_2. Linear first-order plots were observed for sonications in THF, and the solvent characteristics were found to greatly influence the rate of chain scission. Lower rate constants were obtained in THF than in DMF (Figure 19), most likely due to the decreased cavitation efficiency in the higher vapor pressure solvent.[1] The rate constants in DMF began to plateau at the highest molecular weight ranges, which is not observed in THF. These differences likely arise from different solubility parameters, and thus solution conformations and relaxation dynamics, of PPA in each solvent. The nature of the solvent also influenced the resulting products of depolymerization. Analysis of sonicated PPA in DMF by ^{1}H NMR spectroscopy confirmed the production of *ortho*-phthalaldehyde (PA), along with unidentifiable PA decomposition products that were consistent with results from independent sonication of PA in DMF (see Figure 21 in section 3.4.5.). In context, when PPA was sonicated in

THF-d_8, PA was cleanly produced over the sonication time without the production of the byproducts observed in DMF sonications (see Figure 22 in section 3.4.5.). This is significant for applications in which PPA may be used as a reconfigurable material and its monomers must be repolymerized.[3] The rate of degradation with CH_2Cl_2 as solvent could not be reliably calculated due to very rapid degradation of the polymer. This is likely ascribed to the fact that CH_2Cl_2 is known to degrade during sonication, presumably generating HCl,[11] which can catalyze the rapid depolymerization of PPA. During our sonication experiments using CH_2Cl_2 as solvent, we observed complete loss of PPA in less than three minutes of sonication on-time (see Figure 23 in section 3.4.6.). As with experiments in DMF, we found the PPA to be stable in CH_2Cl_2 for extended periods without exposure to ultrasound irradiation, further indicating degradation products of CH_2Cl_2 as a likely source of the breakdown during sonication.

Previously, a heterolytic activation mechanism was computationally and experimentally demonstrated for the mechanochemical degradation of PPA.[3] We wanted to further explore how the degradation rate of PPA could be attenuated based on the nature and concentration of trapping agents. Toward this end, we conducted sonication experiments of PPA in the presence of the nucleophilic agents indole and 2-methylindole and electrophilic species *tert*-butyldimethylsilyl chloride (TBS-Cl) and trifluoroacetic anhydride (TFAA). The oxocarbenium end groups were successfully trapped by indole and 2-methylindole (each 50 molar equivalents relative to PPA repeat units). We observed similar PPA depolymerization profiles in the presence of each of these trapping agents, and both were found to retard the degradation of PPA by curtailing depolymerization. When a higher concentration of 2-methylindole was used (250 molar equivalents) the rate of polymer degradation was further slowed (Figure 20). This concentration dependence is consistent with chain-end trapping to arrest depolymerization. The hemiacetalate

end group was trapped in separate experiments by the electrophilic trapping agents TFAA and TBS-Cl. Again, we observed a decreased rate of disappearance of PPA for each trapping agent, with TFAA leading to less of an effect than TBS-Cl.

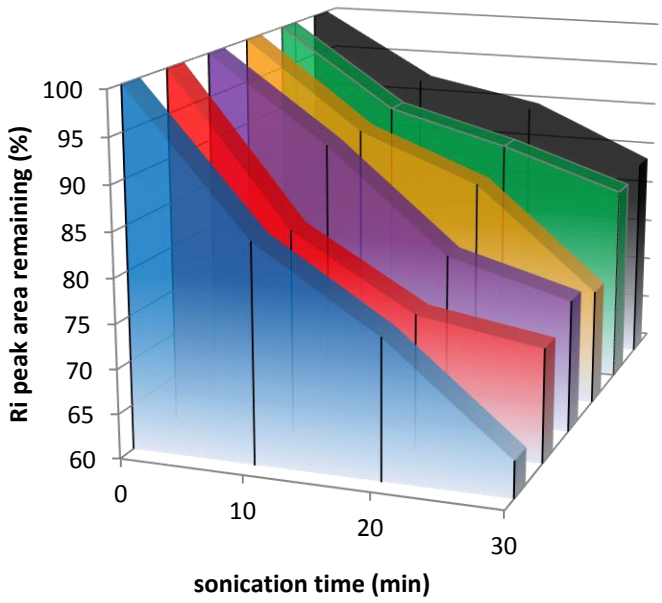

Figure 20. Plots of GPC-RI peak area versus sonication time: (blue) without a trapping agent, with (red) 50 equiv. indole, (purple) 50 equiv. 2-methylindole, (orange) 50 equiv. TFAA, (green) 250 equiv. 2-methylindole, (black) 50 equiv. TBS-Cl. Data points shown are an average of two runs.

3.3. Conclusions

In conclusion, we have explored the kinetics of mechanochemical depolymerization of PPA. After chain scission in the PPA backbone, rapid depolymerization of each resulting polymer fragment occurs such that lower molecular weight byproducts are not observed by GPC analysis. The clean degradation of PPA facilitated the determination of rate constants of mechanochemical activation as a function of molecular weights from a single polydisperse sample and sonication experiment. A heterolytic bond cleavage mechanism in combination with nucleophilic or

electrophilic trapping agents was used to modify the degradation kinetics through variation of the nature and amount of the chain-end trapping agent.

3.4. Experimental

3.4.1. General Considerations

Dry THF, DMF, pyridine, and CH_2Cl_2 were obtained from a Glass Contour solvent purification system. PA was recrystallized and dried according to literature procedures.[12] House N_2 was passed through a drying tube before use. All other reagents and solvents were used as obtained from commercial sources. ^{1}H and spectra were recorded on Bruker AVance 300 and 500 MHz spectrometers. Chemical shifts are reported in delta (δ) units, expressed in parts per million (ppm) downfield from tetramethylsilane using the residual protio-solvent as an internal standard ($CDCl_3$, ^{1}H: 7.26 ppm; THF-d_8, ^{1}H: 3.58 and 1.73 ppm). GPC setup consisted of: a Shimadzu pump, 3 in-line MZ Analysentechnik columns, DAWN Heleos II multi-angle laser light scattering and T-rEX refractive index detectors (Wyatt Technology Corporation), and DMF (0.01 M LiBr) as the mobile phase. Sonication experiments were conducted with a 20 kHz Sonics VSX series sonication probe (1.2 cm tip diameter) calibrated according to literature procedures.[13]

3.4.2. General Procedure for the Synthesis of Poly(phthalaldehyde).

Scheme 1. Synthesis of end-capped PPA.

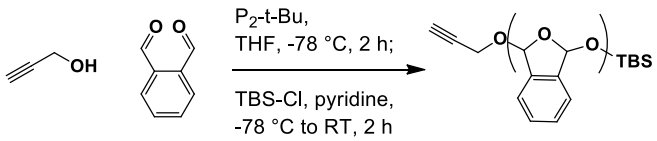

PA (see Table 7 below for specific quantities of reagents) and a stir bar were placed into a recovery flask in a glove box. The monomer was dissolved in anhydrous THF and propargyl alcohol was added via syringe. The flask was sealed with a septum and removed from the glove box. The solution was cooled to -78 °C in a dry ice/acetone bath. A solution of 2.0 M P_2-t-Bu in THF was added via syringe and the reaction solution was vigorously stirred for 2 h. At that point pyridine and TBS-Cl were added and then the mixture was stirred for 2 h while the bath expired and returned to RT. The polymer solution was then precipitated into diethyl ether (4-times the volume of THF) and collected on a sintered-glass Büchner funnel. The precipitate was redissolved in CH_2Cl_2 and reprecipitated into MeOH (10-times the volume of CH_2Cl_2), collected on a sintered-glass Büchner funnel, washed with MeOH, and dried under vacuum.

Table 7. The amounts of reagents used, yield, and GPC characterization data from the syntheses of PPA.

Entry	1	2	3
PA (mg, mmol)	500, 3.73	1000, 7.45	1000, 7.45
THF (mL)	6.2	12.4	12.4
propargyl acohol (µL, mmol)	14, 0.25	0.5, 0.009	0.4, 0.007
P_2-t-Bu (µL, mmol)	249, 0.49	35, 0.070	28, 0.054
pyridine (µL, mmol)	660, 8.18	39, 0.48	30, 0.37
TBS-Cl (g, mmol)	1.12, 7.44	0.07, 0.43	0.05, 0.34
Yield (%)	36	77	53
M_w (kDa)	4.3	41	51
PDI	1.2	1.5	1.6

3.4.3. General Procedure for Sonication Experiments

PPA (25 mg) was added to a Suslick flask under N_2, followed by addition of either DMF, THF, or CH_2Cl_2 via syringe (PPA at 5 mg/mL). The flask was then attached to the sonication probe and sonicated in a water bath in a cold room (13.7 W/cm^2). A pulse sequence of 1 sec on 9 sec off was used to keep the temperature from rising above 15 °C. The solution temperature was internally

monitored with a temperature probe. The polymer was sonicated for a pre-determined on-time at a specific power density. Samples were removed at various time points and the progress was monitored by GPC. A 200 kDa poly(styrene) standard was injected into the GPC (3 mg/mL) prior to the injection of the sonicated samples for normalization purposes.

3.4.4. Rate Constant for Scission of PPA.

Table 8 shows the average rate constant and standard deviations corresponding to the plot in Figure 19 in section 3.2.

Table 8. Rate constants with standard deviations for various molecular weight ranges for the degradation of a 27 kDa PPA in DMF and THF.

	DMF		**THF**	
M_n **range**	rate constant ($\times 10^{-2}$) (1/min)	std. dev. ($\times 10^{-2}$) (1/min)	rate constant ($\times 10^{-2}$) (1/min)	std. dev. ($\times 10^{-2}$) (1/min)
35-40	11.92	0.59	1.44	0.06
40-45	13.48	0.62	1.83	0.11
45-50	15.22	0.72	2.30	0.15
50-55	16.88	0.72	2.87	0.22
55-60	18.31	0.51	3.52	0.31
60-65	19.47	0.99	4.31	0.41
65-70	20.30	0.98	5.11	0.53
70-75	20.46	1.45	5.98	0.68

3.4.5. Confirmation That PPA Degradation Produces PA

After PPA (51 kDa) sonication in DMF for 60 min, the solvent was removed under reduced pressure and a ^{1}H NMR spectrum was collected. While a small amount of PA was present, the spectrum contained peaks that could not be attributed to PA. To better determine the origin of the impurities, PA was sonicated as in section 3.4.3. except GPC analysis was not conducted. After 60

min of sonication the solvent was removed under reduced pressure and a ^{1}H NMR spectrum was collected. As can be seen in Figure 21, the PPA and PA sonication in DMF each gave similar results, indicating that PA is not stable to sonication conditions in DMF or that PA is reacting with byproducts arising from prolonged DMF sonication.

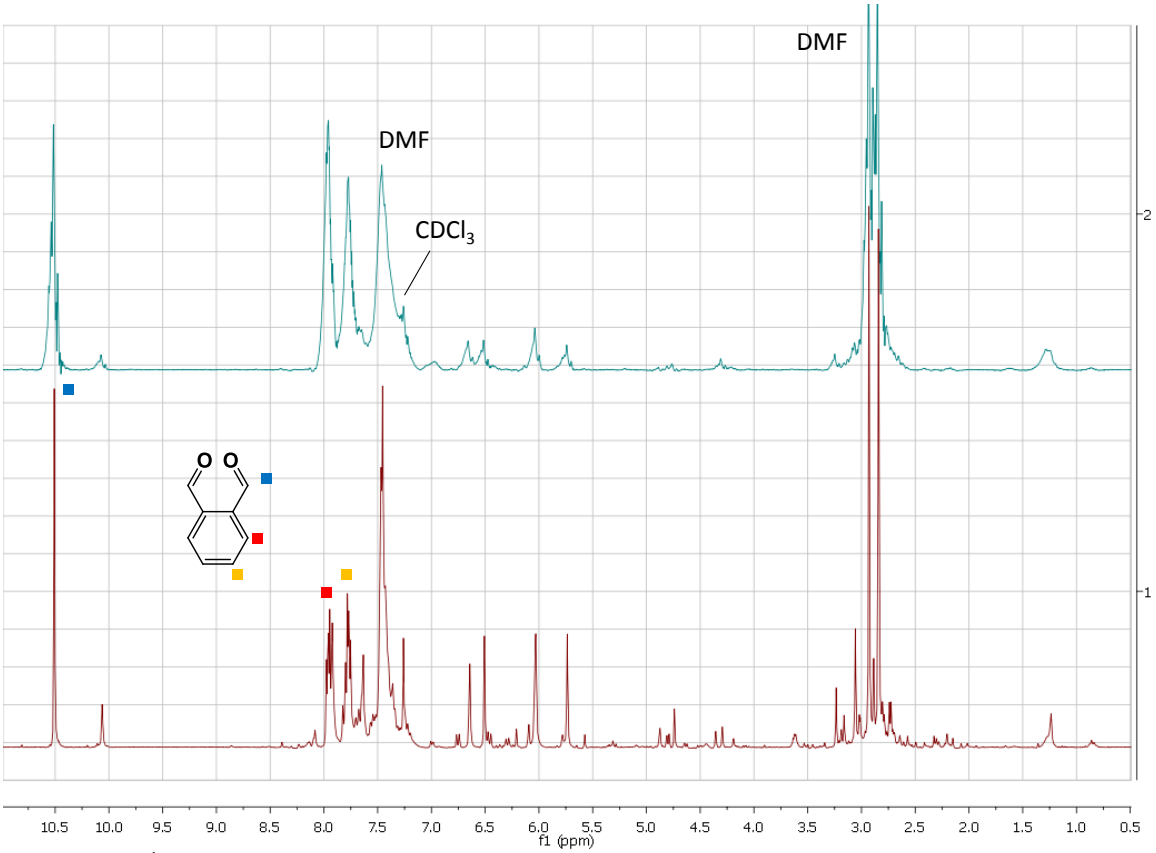

Figure 21. ^{1}H NMR spectra (in chloroform-*d*) of (top) PPA after 60 min and (bottom) PA after 60 min of sonication in DMF.

We next wanted to compare these results to the sonication of PPA in THF. PPA was sonicated in THF-d_8 as in section 3.4.3. except that samples were removed for NMR rather than GPC analysis. As shown in Figure 22, PA was cleanly produced without the byproducts that were observed in the DMF sonication.

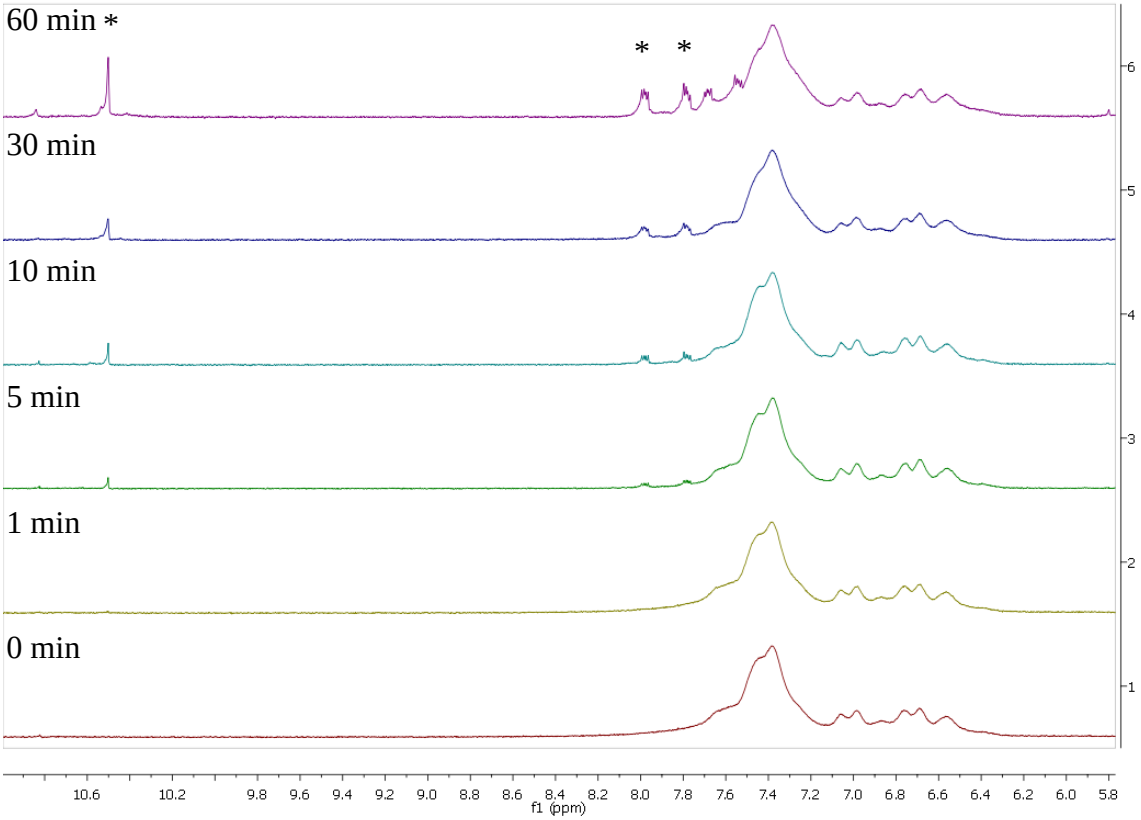

Figure 22. ^{1}H NMR spectra of PPA at various time points during sonication in THF-d_8. *Indicates peaks corresponding to PA.

3.4.6. Sonciation of PPA in CH_2Cl_2

PPA was sonicated in CH_2Cl_2 as in section 3.4.3. As can be seen in Figure 23, substantial polymer degradation was observed even after 1 min of sonication on-time. After 3 min, no polymer remained.

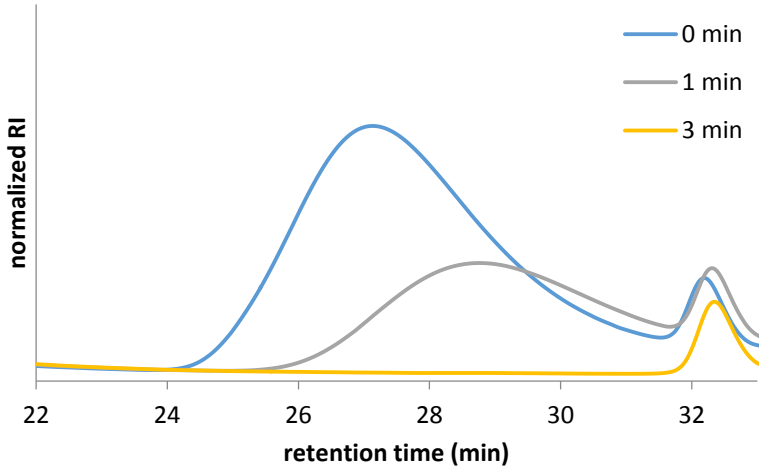

Figure 23. GPC chromatograms of PPA during sonication in CH_2Cl_2. The times indicate total "on time" of ultrasound using a duty cycle of 1 s on, 9 s off.

3.4.7. Sonciation With Trapping Agents

TBS-Cl: PPA was sonicated as in the section 3.4.3. with the addition of TBS-Cl (7mg, 50 mol. equiv. to PPA) and pyridine (4 µL, 55 mol. equiv. to PPA). TFAA: PPA was sonicated as in the *section 3.4.3* with the addition of TFAA (6.5 µl, 50 mol. equiv. to PPA) and pyridine (4 µL, 55 mol. equiv. to PPA). Indole: PPA was sonicated as in the *section 3.4.3* with the addition of indole (5 mg, 50 mol. equiv. to PPA). 2-methylindole: PPA was sonicated as in the *section 3.4.3* with the addition of 2-methylindole (26 mg, 250 mol. equiv. to PPA or 5mg, 50 mol. equiv. to PPA). All trapping experiments were completed in duplicate.

3.5. References

(1) For recent reviews, see: (a) Brantley, J. N.; Bailey, C. B.; Wiggins, K. M.; Keatinge-Clay, A. T.; Bielawski, C. W. *Polym Chem.* **2013**, *4*, 3916. (b) May, P. A.; Moore, J. S. *Chem. Soc. Rev.* **2013**, *42*, 7497. (c) Wiggins, K. M.; Brantley, J. N.; Bielawski, C. W. *Chem. Soc. Rev.* **2013**, *42*, 7130. (d) Groote, R.; Jakobs, R. T. M.; Sijbesma, R. P. *Polym. Chem.* **2013**, *4*, 4846. (e) Brantley,

J. N.; Wiggins, K. M.; Bielawski, C. W. *Polym. Int.* **2012**, *62*, 2. (f) Ariga, K.; Mori, T.; Hill, J. P. *Adv. Mater.* **2012**, *24*, 158. (g) Boulatov, R. *Pure Appl. Chem.* **2011**, *83*, 25. (h) Caruso, M. M.; Davis, D. A.; Shen, Q.; Odom, S. A.; Sottos, N. R.; White, S. R.; Moore, J. S. *Chem. Rev.* **2009**, *109*, 5755. (i) Beyer, M. K.; Clausen-Schaumann, H. *Chem. Rev.* **2005**, *105*, 2921.

(2) For recent examples, see: (a) Brantley, J. N.; Bailey, C. B.; Cannon, J. R.; Clark, K. A.; Vanden Bout, D. A.; Bodbelt, J. S.; Keatinge-Clay, A. T.; Bielawski, C. W. *Angew. Chem. Int. Ed.* **2014**, *53*, 5088. (b) Lee, C. K.; Diesendruck, C. E.; Lu, E.; Pickett, A. N.; May, P. A.; Moore, J. S.; Braun, P. V. *Macromolecules*, **2014**, *47*, 2690. (c) Grady, M. E.; Beiermann, B. A.; Moore, J. S.; Sottos, N. R *ACS Appl. Mater. Inter.* **2014**, *6*, 5350. (d) Larsen, M. B.; Boydston, A. J. *J. Am. Chem. Soc.* **2014**, *136*, 1276. (e) Gossweiler, G. R.; Hewage, G. B.; Soriano, G.; Wang, Q.; Welshofer, G. W.; Zhao, X.; Craig, S. L. *ACS Macro Lett.* **2014**, *3*, 216. (f) Beiermann, B. A.; Kramer, S. L. B.; May, P. A.; Moore, J. S.; White, S. R. and Sottos, N. R *Adv. Funct. Mater.* **2014**, *24*, 1529. (g) Larsen, M. B.; Boydston, A. J. *J. Am. Chem. Soc.* **2013**, 135, 8189. (h) Degen, C. M.; May, P. A.; Moore, J. S.; White, S. R.; Sottos, N. R. *Macromolecules*, **2013**, *46*, 8917. (i) Lee, C. K.; Beiermann, B. A.; Silberstein, M. N.; Wang, J.; Moore, J. S.; Sottos, N. R.; Braun, P. V. *Macromolecules*, **2013**, *46*, 3746. (j) Konda, S. S. M.; Brantley, J. N.; Varghese, B. T.; Wiggins, K. M.; Bielawski, C. W.; Makarov, D. E. *J. Am. Chem. Soc.* **2013**, *135*, 12722. (k) Brantley, J. N.; Wiggins, K. M.; Bielawski, C. W. *Angew. Chem. Int. Ed.* **2013**, *52*, 3806. (l) Klukovich, H. M.; Kouznetsova, T. B.; Kean, Z. S.; Lenhardt, J. M.; Craig, S. L. *Nat. Chem.* **2013**, *5*, 110. (m) Ramirez, A. L.; Black; K.; Z. S.; Orlicki, J. A.; Champhekar, M.; Elsakr, S. M.; Krause, W. E.; Craig, S. L. *Nat. Chem.* **2013**, *5*, 757. (n) Kean, Z. S.; Niu, Z.; Hewage, G. B.; Rheingold, A. L.; Craig, S. L. *J. Am. Chem. Soc.* **2013**, *135*, 13598.

(3) Diesendruck, C. E.; Peterson, G. I.; Kulik, H. J.; Kaitz, J. A.; Mar, B. D.; May, P. A.; White, S. R.; Martinez, T. J.; Boydston, A. J.; Moore, J. S. *Nat. Chem.* **2014**, *6*, 623.

(4) Random mid-chain scission is observed upon application of acid or thermal impetus: (a) Knoll, A. W.; Pires, D.; Coulembier, O.; Dubois, P.; Hedrick, J. L.; Frommer, J.; Duerig, U. *Adv. Mater.* **2010**, *22*, 3361. (b) Coulembier, O.; Knoll, A.; Pires, D.; Gotsmann, B.; Duerig, U.; Frommer, J.; Miler, R. D.; Dubois, P.; Hedrick, J. L. *Macromolecules* **2010**, *43*,572. (c) Kostler, S.; Zechner, B.; Trathnigg, B.; Fasl, H.; Kern, W.; Ribitsch, V. *J. Polym. Sci. Part A: Polym. Chem.* **2009**, *47*, 1499.

(5) Sequential head-to-depolymerization can be obtained for PPAs end cap functionalized with a stimuli responsive trigger, for recent reviews see: (a) Phillips, S. T.; DiLauro, A. M. *ACS Macro Lett.* **2014**, *3*, 298. (b) Peterson, G. I.; Larsen, M. B.; Boydston, A. J. *Macromolecules* **2012**, *45*, 7317.

(6) (a) Malhotra, S. *J. Macromol. Sci., Part A* **1986**, *23*, 729. (b) Malhotra, S. *J. Macromol. Sci., Part A* **1982**, *18*, 1055.

(7) Florea, M. *J. App. Polym. Sci.* **1993**, *50*, 2039.

(8) (a) Vijayalakshmi, S. P.; Madras, G. *Polym. Degrad. Stab.* **2005**, *90*, 116. (b) Kryger, M. J.; Munaretto, A. M.; Moore, J. S. *J. Am. Chem. Soc.* **2011**, *133*, 18992. (c) Basedow, A. M.; Ebert, K. H. *Adv. Poly. Sci.* **1977**, *22*, 83. (d) Jellinek, H. H. G.; *J. Polymer Sci.* **1959**, *37*, 485.

(9) (a) Nguyen, T. Q.; Liang, Q. Z.; Kausch, H. H. *Polymer* **1997**, *38*, 3783. (b) Taghizadeh, M. T.; Asadpour, T. *Ultrason. Sonochem.* **2009**, *16*, 280. (c) Thomas, J. R. *J. Phys. Chem.* **1959**, *63*, 1725.

(10) Kaitz, J. A.; Diesendruck, C. E.; Moore, J. S. *J. Am. Chem. Soc.* **2013**, *135*, 12755.

(11) (a) Lim, M.; Son, Y.; Yang, J.; Khim, J. *Jpn. J. Appl. Phys.* **2008**, *47*, 4123. (b) Colussi, A. J.; Hung, H.-M.; Hoffmann, M. R. *J. Phys. Chem. A* **1999**, *103*, 2969. (c) Korn, M.; Acevedo, M. S. F.; Borges, S. S.; Lima, J. L. F. C. *J. Braz. Chem. Soc.* **2005**, *16*, 988.

(12) DiLauro, A. M.; Abbaspourrad, A.; Weitz, D. A.; Phillips, S. T. *Macromolecules* **2013**, *46*, 2963.

(13) Potisek, S. L.; Davis, D. A.; Sottos, N. R.; White, S. R.; Moore, J. S. *J. Am. Chem. Soc.* **2007**, *129*, 13808.

Chapter 4 – 3D-Printed Mechanochromic Materials

Reproduced with permission from: Peterson, G. I.; Larsen, M. B.; Ganter, M. A.; Storti, D. W.; Boydston, A. J. 3D-Printed Mechanochrmoic Materials. *ACS Appl. Mater. Interfaces* **2014**, *7*, 577-583.

4.1. Introduction

Three-dimensional printing (3DP) is a method of additive manufacturing that enables the construction of 3D objects based upon a digital model. Although the basic methods for 3DP have been known for decades, the area has seen a recent surge of interest as researchers continue to develop new materials that enhance the capabilities of 3DP and as broader communities find new applications that benefit from software-reconfigurable rapid prototyping.[1-3] When a digital model is supplied to the printer, the printing system uses slicing software that converts the 3D model to 2D slice descriptions, and a G-code generator converts the slice descriptions into numerically controlled machine instructions. With this approach to manufacturing, the time and resources required for production of a single prototype of an envisioned object are streamlined. In contrast to traditional manufacturing techniques, such as injection or compression molding, the advantages of 3DP include increased customizability, ease of use, orthogonality to existing manufacturing techniques, and accessibility to the technique by a wide user base of a variety of backgrounds and skill levels. Fused filament fabrication (FFF), for instance, has become accessible in private homes for printing the likes of toys, housewares, art pieces, and accessories for portable electronics.

An exciting and potentially transformative area of growth is the integration of functional polymeric materials with 3DP technologies.[1,2] As these areas merge, the capabilities afforded by designer polymer synthesis can be incorporated into rapidly customizable objects and devices.[4,5] Examples of 3D-printed functional materials and devices include drug delivery platforms,[6,7] tissue

scaffolds,[8-11] energy storage devices,[12,13] electrically conductive materials,[14-17] and force-sensors.[18-20]

We envisioned the ability to incorporate mechanochemically-responsive units into materials amenable to 3DP techniques to produce printed objects with well-defined shapes and regions capable of chemo-mechanical coupling.[20] Recent advances in polymer mechanochemistry have given rise to systems that translate macroscopic mechanical force into specific chemical reactivity.[21-24] In the solid state, mechano-responsive polymers and materials have shown promise for applications including mechanochromic force sensors,[25-32] mechano-catalysis,[33] self-reinforcing materials,[33,34] and scaffolds for small molecule release.[25,35-37] Among the various mechanophores reported in the literature, we were particularly interested in the mechanochromic spiropyran systems that have been extensively studied in the field, as the ease of determining qualitative activation in this system is unmatched.[25-30] Upon application of force across the C_{spiro}-O bond (Figure 24), isomerization of the spiropyran to its highly colored purple merocyanine isomer can be accomplished, effectively enabling the self-reporting of stress accumulation within a macroscopic material via readily identifiable color change.

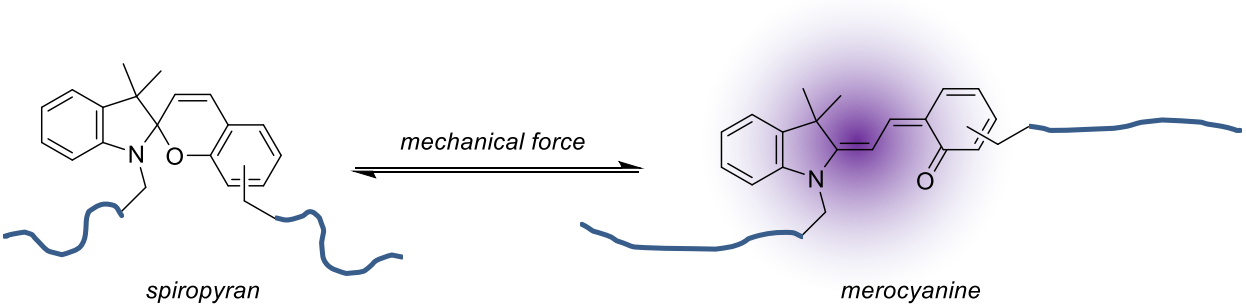

Figure 24. Generalized depiction of the mechanochemical isomerization of a spiropyran moiety to its merocyanine form.

Recently, we demonstrated the 3DP of poly(ε-caprolactone) (PCL) containing a chain-centered spiropyran and explored its basic mechano-responsive characteristics in a notched specimen and prototype force sensor.[20] In this manuscript, we characterize the mechanical properties of the printed materials and explore the extent to which polymer degradation occurs during filament formation and extrusion printing. We also examine the incorporation of different spiropyran moieties into 3D printed PCL. Specifically, we prepare multi-component specimens that display selective activation of specific regions in the materials, depending on the stimulus being applied. These results include the first demonstration of a spiropyran that is uniquely responsive to mechanical force without displaying the same photo-responsiveness observed from all previously reported spiropyran mechanophores. We also showcase the unique abilities of 3DP in contrast with other traditional manufacturing techniques by demonstrating rapid customization of the dynamic sensing range of a force sensor. The utility of this paradigm and its suitability for broad adoption is supported by presenting illustrative results obtained using only inexpensive entry-level 3DP technology and freely available software.

4.2. Results and Discussion

Three spiropyran containing polymers were prepared via ring opening polymerization of ε-caprolactone from spiropyran alcohol initiators (Scheme 2). Polymers **3** (M_w = 90.0 kDa, Đ = 1.16) and **8** (M_w = 82.5 kDa, Đ = 1.18) bear chain-centered spiropyrans such that elongation of the polymer results in stress accumulation across the desired C_{spiro}-O bond, and isomerization is activated. In contrast, polymer **4** (M_w = 64.9 kDa, Đ = 1.43) has a chain-end spiropyran moiety such that stress will not be accumulated across the necessary bond, and thus it should not be activated by mechanical stimulus. Notably, each of these polymers is of sufficient molecular

weight to accumulate tensile forces within the main chain that are great enough to induce mechanochemical activation.

Scheme 2. Synthesis of polymers **3**, **4**, and **8**.

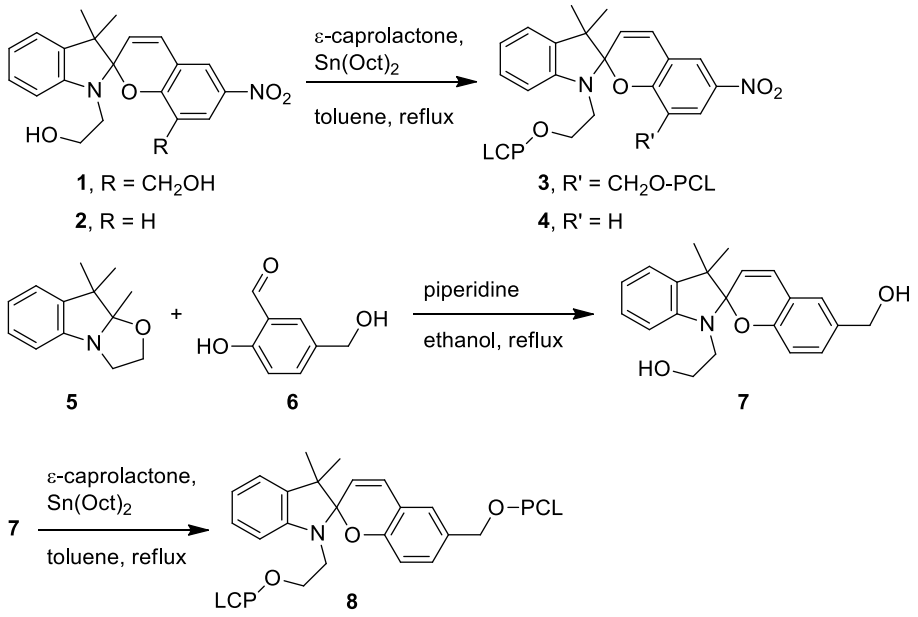

Each polymer was blended with commercial PCL (**C**) at various concentrations (Table 9). The wt % of each spiropyran-containing polymer is denoted by the subscript (e.g., $\mathbf{3}_{\mathbf{10}}$ is comprised of 10 wt % **3** and 90 wt % **C**). Filament was prepared using a single screw melt extruder. Average batch-to-batch filament diameters ranged from ca. 1.55 to 1.85 mm, with variation along the filament typically being less than ± 0.05 mm. The custom filaments were used to print tensile testing specimens using a commercial dual-extrusion head FFF printer. Printing was initially performed using only one of the extrusion heads set at a temperature of 110 °C, a non-heated build plate, and a relatively slow print speed of 20 mm/s (in comparison with 120 – 150 mm/s typically used for printing acrylonitrile-butadiene-styrene or poly(lactic acid) filament). Due to the

relatively flexible nature of the filament, retraction was disabled to avoid jamming of the filament during printing.

Table 9. Structure, molecular weight, and dispersity data for the synthesized and commercial polymer, and compositions of various filament types.

Filament	Polymer	M_w (kDa), Đ	Blend	Spiropyran % w/w
3$_{10}$	**3**	90.0, 1.16	10% w/w with **C**	0.05
3$_{50}$			50% w/w with **C**	0.25
3$_{100}$			none	0.50
4$_{50}$	**4**	64.9, 1.43	50% w/w with **C**	0.39
8$_{50}$	**8**	82.5, 1.18	50% w/w with **C**	0.43
C$_{100}$	**C**	62.7, 1.29	none	none

During the mixing and melt extrusion steps of the filament formation process, no color changes were observed from any of the spiropyran-containing materials. Additionally, no color changes were observed during printing, indicating no thermal activation of the spiropyran was taking place. To determine if any polymer degradation was occurring during the pre-print processing or printing, a printed specimen was subjected to GPC analysis. No detectable changes in polymer molecular weight or dispersity were observed as compared to the virgin polymer (Figure 25).

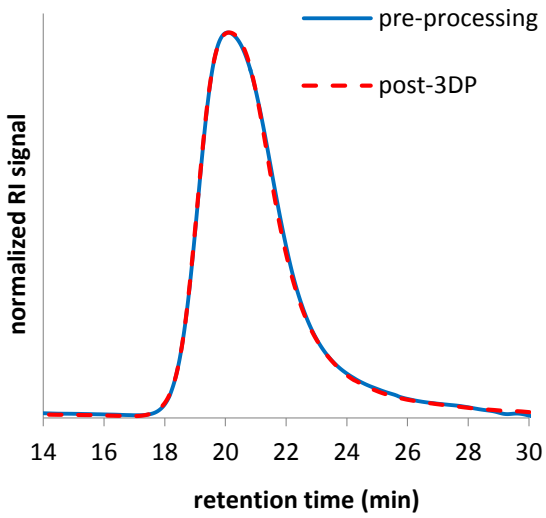

Figure 25. GPC chromatograms of polymer 3 prior to any filament or print processing and after 3DP.

To examine the basic mechanochemical reactivity and mechanical properties of the materials and to ensure a controlled environment for elongation, tensile testing of "dog bone" shaped specimens was performed on an Instron load frame. In all cases in which **3** was present, color change from brown to purple was observed upon elongation and necking of the sample, signifying mechanochemical activation of the spiropyran in accordance with previous studies.[25-30] While the intensity of the resulting color was directly related to the amount of **3** used in the blend (Figure 26), the most apparent contrast between virgin and elongated (activated) materials was observed for blends having lower loading of spiropyran, due to the lighter color of the unactivated material. No spiropyran activation was observed in the test specimens made from $\mathbf{4}_{50}$ in which the mechanophore is located at a chain end, thus confirming the mechanical origin of the color change. Although the Young's modulus and yield strength of each blended material were found to be lower

than that of the non-blends (Table 10), all are in good agreement with reported values for PCL.[38] Re-filamentizing the commercial material **C** also led to a decrease in Young's modulus and yield strength. As GPC analysis showed no polymer degradation occurring during the processing/printing process (*vide supra*), a possible explanation in the differences of materials properties between $\mathbf{C_{100}}$ and re-extruded $\mathbf{C_{100}}$ could be the variation in diameter of the filament made in-house, leading to heterogeneity in the structure of the printed objects.

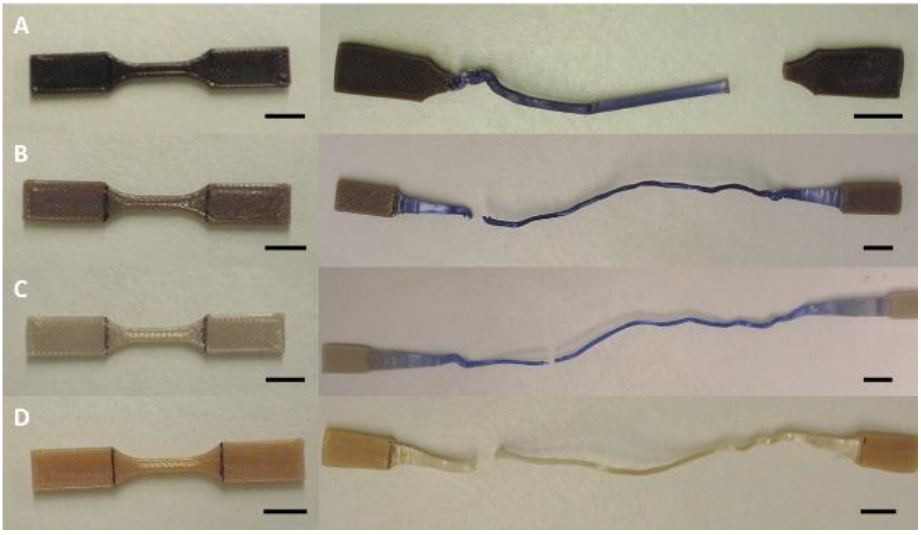

Figure 26. Tensile test specimens made from (A) $\mathbf{3_{100}}$, (B) $\mathbf{3_{50}}$, (C) $\mathbf{3_{10}}$, and (D) $\mathbf{4_{50}}$ pre- and post-elongation. The vertical marks on the specimen indicate the position of the load frame clamps. Scale bars = 10 mm.

Table 10. Summary of the materials properties of the test specimens prepared from the various filament types. Values are an average of three experiments ± one standard deviation.

Filament Type	Modulus (GPa)	Yield Strength (MPa)	Tensile Strength (MPa)	% elongation to break
C$_{100}$	0.336 ± 0.042	16.57 ± 0.20	33.24 ± 1.15	709 ± 25
C$_{100}$ (re-extruded)	0.225 ± 0.011	13.3 ± 0.10	n. d.[a]	n. d.[a]
3$_{10}$	0.268 ± 0.029	13.32 ± 0.42	29.50 ± 1.12	750 ± 81
3$_{50}$	0.300 ± 0.003	14.56 ± 0.48	27.17 ± 1.94	664 ± 37
3$_{100}$	0.351 ± 0.030	17.49 ± 0.24	14.86 ± 1.71	302 ± 12
4$_{50}$	0.300 ± 0.067	15.00 ± 0.21	26.82 ± 0.31	651 ± 12
3$_{50}$ encased in **C$_{100}$**	0.308 ± 0.045	15.96 ±0.83	33.15 ±1.61	716 ±56

[a]Not determined. Samples necked into the grip region and slipped from the grips in all samples measured.

We next prepared multi-component specimens that highlight the capabilities of 3DP in contrast with other types of traditional manufacturing methods, such as injection or compression molding. A tensile test specimen comprised of discrete regions of photo- and mechano-responsive **3$_{50}$** and photo-responsive **4$_{50}$** was printed in a single session by using two extrusion heads, each loaded with one of the filament types. In this particular dual extrusion technique, the active print head alternates such that only one head is printing at a time. The test specimen body was comprised mainly of **4$_{50}$** which was used as a housing around two surface channels of **3$_{50}$** that spanned the length of the printed specimen (Figure 27). Upon elongation of the sample, only the regions containing **3$_{50}$** were activated, signifying the spatio-control over the material's response to external force. Notably, the spiropyran moieties in both materials were still susceptible to UV-triggered

isomerization and confirmation of spiropyran content throughout the materials was confirmed upon illumination with 365 nm light from a handheld UV lamp.

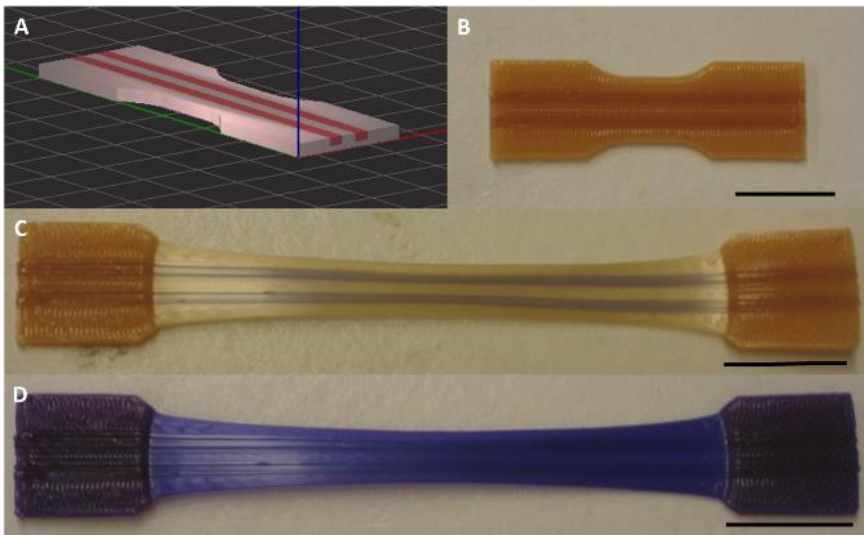

Figure 27. (A) Computer aided design (CAD) representation of a multi-component tensile test specimen, with red stripe indicating the location of the mechano-responsive filament **3**$_{50}$ (specimen body comprised of **4**$_{50}$), (B) test specimen pre-elongation, (C) test specimen post-elongation showing the mechanochromic response of the **3**$_{50}$ regions, and (D) test specimen post-elongation after 365 nm UV irradiation showing activation of both the **3**$_{50}$ and **4**$_{50}$ regions. Scale bars = 20 mm.

We next considered a system in which the chromic response could be selectively activated with mechanical impetus. Absent the electron-withdrawing nitro functionality, the photostationary state of UV-irradiated spiropyrans contains a negligible amount of the corresponding merocyanine isomer, and thus no photochromism is observed.[39,40,41] However, we found that application of stress across the C_{spiro}-O bond still resulted in mechanochromism in this spiropyran. To

demonstrate this in a 3D printed specimen, we prepared a multi-component specimen similar to the one depicted in Figure 27, but with a body composed of $\mathbf{8}_{50}$ (mechano-responsive, but not photo-responsive), and the surface channels composed of $\mathbf{4}_{50}$, (photo-responsive, but not mechano-responsive) (Figure 28A). Irradiation of the specimen with 365 nm UV radiation only led to activation of the regions containing $\mathbf{4}_{50}$ (Figure 28B). On the other hand, elongation of the specimen led to activation of the $\mathbf{8}_{50}$ regions but not of the $\mathbf{4}_{50}$ regions (Figure 28C), consistent with the results in Figure 4. Visually detectable activation of polymer **8** was only readily observed when the polymer was under load; upon relieving the tension on the specimen, the purple color rapidly disappeared. For example, within the ca. 30 s required to remove the sample from the grips in the load frame, nearly all of the purple color had disappeared (Figure 28D). The reactivity of polymer **8** is significant as it enables the use of these mechanochromic materials in outdoor applications, whereas polymers **3** and **4**, which are both photo-responsive, are rapidly converted to the merocyanine form in direct sunlight.

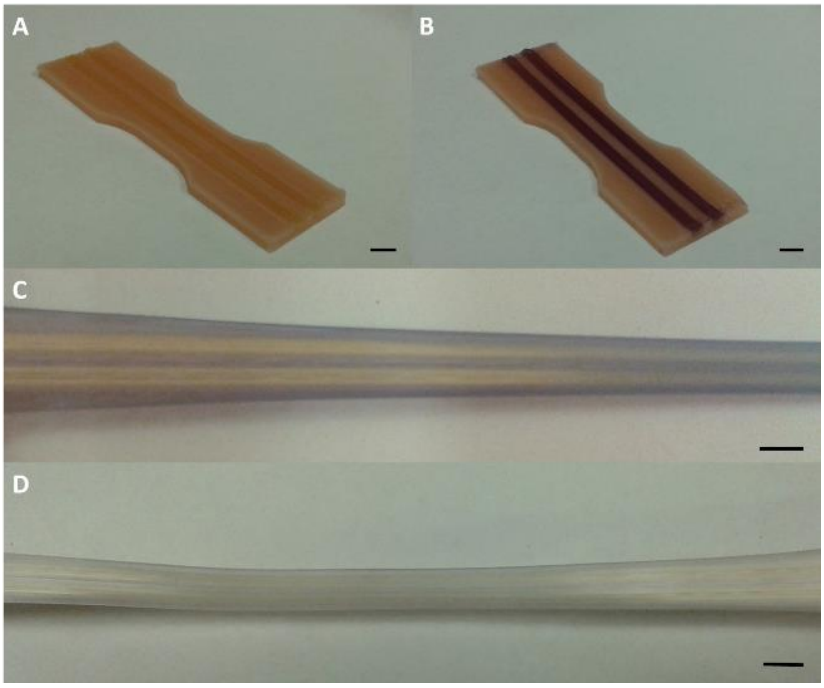

Figure 28. (A) Test specimen composed of **8**$_{50}$ with stripes of **4**$_{50}$, (B) test specimen after 365 nm UV irradiation showing the photochromic response of the **4**$_{50}$ regions, (C) test specimen under load in the load frame showing the mechanochromic response of the **8**$_{50}$ regions, and (D) test specimen ca. 30 s after removal of load showing almost complete loss of the purple color in the **8**$_{50}$ regions. Scale bars = 5 mm.

We next explored the use of 3DP to prepare objects in which a center region of mechano-responsive **3**$_{50}$ was completely encased by **C**$_{100}$ (Figure 29), a type of structure that would be difficult (if not impossible) to prepare in a single operation via most other manufacturing techniques. Using the dual extrusion method, the target configuration was printed in a single session and then subjected to elongation as before. The **3**$_{50}$ region was again activated and the color change was visible from the exterior of the material. The mechanical properties of this specimen design were similar to the specimens comprised solely of **C** (Table 10), indicating that the stimuli-responsive properties of **3**$_{50}$ can be imparted to larger prints without affecting the bulk properties

of the material. Using the same print code and replacing **C** with control filament $\mathbf{4_{50}}$ as the exterior material resulted in a sample in which the $\mathbf{3_{50}}$ region was not visible prior to elongation (Figure 30). Upon tensile testing, the mechano-responsive core became clearly distinguishable from the encasing filament.

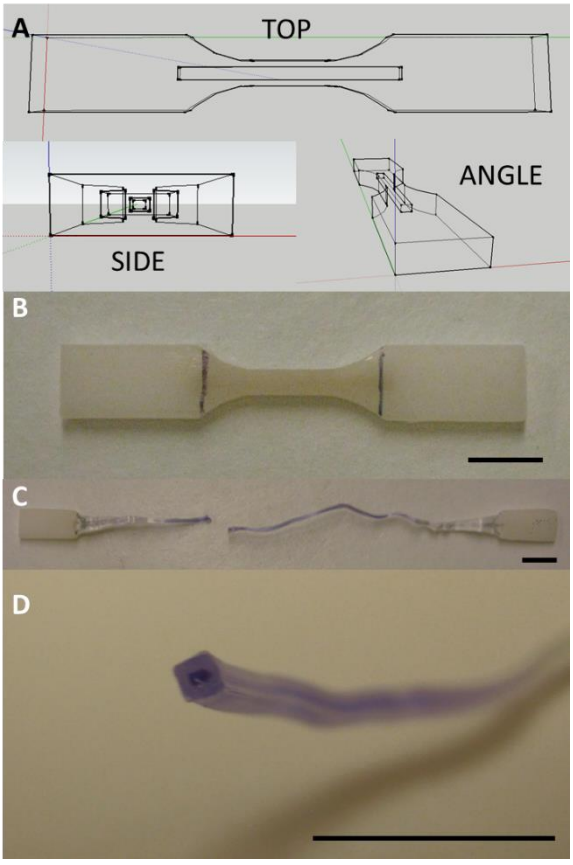

Figure 29. (A) CAD representations of the tensile test specimen in which the mechano-responsive region is encased by non-mechano-responsive filament, (B) test specimen in which $\mathbf{3_{50}}$ is encased by $\mathbf{C_{100}}$ (the vertical lines on the specimen indicate the position of the load frame clamps), (C) test specimen post-elongation showing the mechanochromism of the $\mathbf{3_{50}}$ region, and (D) elongated and cut specimen showing the encased filament. Scale bars = 10 mm.

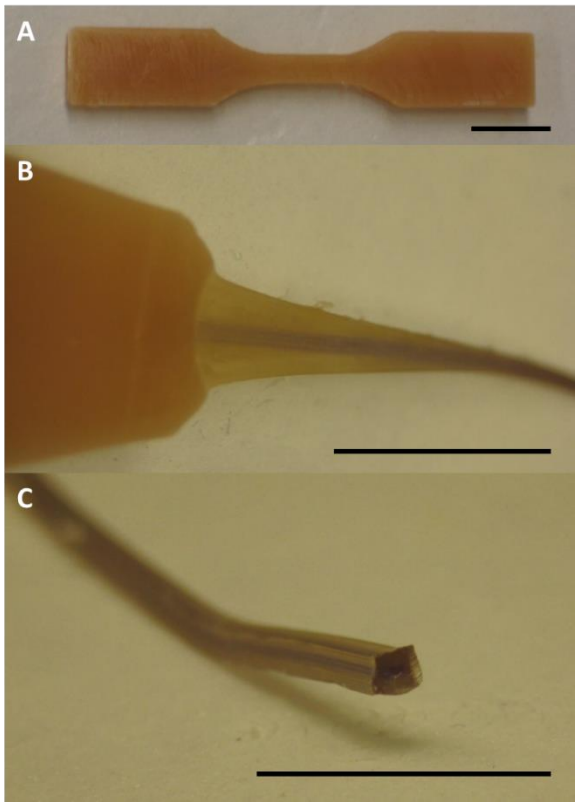

Figure 30. (A) Tensile test specimen in which **3**$_{50}$ is encased by **4**$_{50}$, (B) test specimen post-elongation showing the mechanochromism of the **3**$_{50}$ region, and (C) elongated and cut specimen showing the encased filament. Scale bars = 10 mm.

Prototype force sensors were developed to demonstrate the potential engineering applications that can be accessed by integrating mechano-responsive polymers and 3DP technology. An asymmetric tensile test specimen was prepared with multiple embedded regions of **3**$_{50}$ spaced evenly within the gauge section (Figure 31). Initial testing of dog bones with constant cross-section produced force-extension curves that were flat between initial necking and eventual strain hardening (see Figure 34 in section 4.4.8.). This led us to pursue an asymmetric dog bone with a variable cross-section. Introducing a section width that varies linearly with displacement

along the axis of symmetry resulted in a relationship between the extension and the force required to draw the material that is linear over a broad domain of extension. By controlling the initial location and direction in which the material necks, the design ensures sequential and predictable activation of each mechano-responsive region (see Figure 35 in section 4.4.9.). The onset of activation of each region is directly related to a specific force that was applied to the specimen (Figure 32). By simply counting the number of activated regions, the amount of peak force applied to the material could be quickly estimated with no additional characterization or analysis. Good reproducibility of the force required to activate each region in the sensor is highlighted by the small standard deviations obtained after three test runs (see Table 11 in the section 4.4.9.).

One of the advantages of using 3DP to prepare prototypes and end-user products is the ability to quickly modify and optimize designs for a given application. To demonstrate the ease with which this can be accomplished, we modified the thickness of our force sensor to expand the range of detectable loads. By simply changing the thickness dimension in our computer aided design (CAD) model we could quickly print different variations of the sensor without any additional tooling. In contrast, a similar process via injection molding would require preparation of a new mold for each design. By changing the thickness of the specimens, different dynamic ranges were able to be accessed. Specifically, increasing the specimen thickness from 1 mm to 7 mm led to nearly an order of magnitude increase in the forces detectable by the sensor. Furthermore, the number, shape, spacing, and composition of mechano-responsive regions could also be customized based on the needs of the application. Obtaining this level of customizability would be extremely difficult without using 3DP technologies.

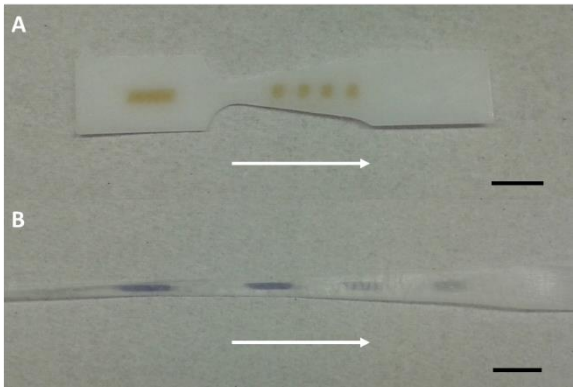

Figure 31. (A) 1 mm thick force sensor before elongation, and (B) post-elongation. The white arrows indicate the direction of necking. Scale bars = 10 mm.

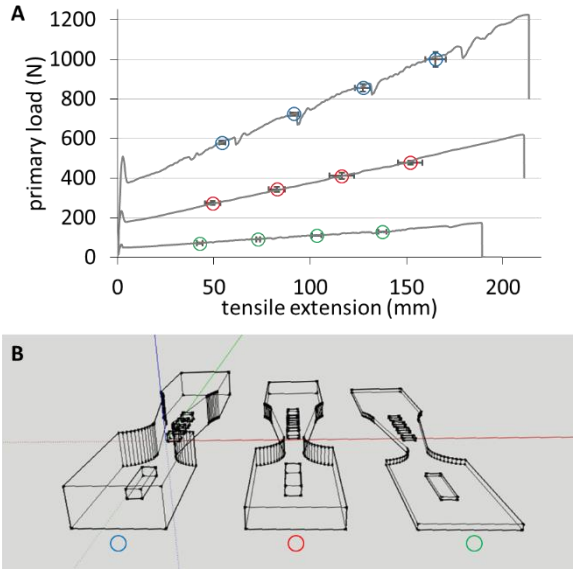

Figure 32. (A) Representative plots of tensile extension vs load for force sensors of ca. 1 (○), 4 (○), and 7 (○) mm thickness. The markers indicate the onset of the activation of each mechano-responsive region (average of three runs). Error bars represent ± one standard deviation. (B) CAD representation of each of the force sensors.

4.3. Conclusions

In summary, we have demonstrated the successful 3D printing of a variety of stimuli-responsive polymers and the development of a new spiropyran mechanophore that exhibits selectivity toward mechanical activation by not exhibiting a photochromic response to either natural sunlight or 365 nm UV irradiation. The basic mechanical properties of the different structures prepared with various filament formulations showed some variation, but were within the range of reported values for PCL. The use of 3DP enabled rapid production of multi-component materials such as encased mechano-responsive materials within commercial or control polymers. These materials would generally be difficult or impossible to prepare with other manufacturing techniques. Additionally, rapid modification of a prototype force sensor was demonstrated to show its tunability and the advantages of using 3DP. These demonstrations were borne out through integration of mechano-responsive polymer technology and the unique features of 3DP. The ability to produce these materials using consumer level equipment is expected to facilitate adoption, use, and exploration by a wide audience.

4.4. Experimental

4.4.1. General Considerations

Dry toluene was obtained from a Glass Contour solvent purification system. The monomer, ε-caprolactone, was dried over 4 Å molecular sieves for 48 h prior to use. House N_2 was passed through a drying tube before use. All other reagents and solvents were used as obtained from commercial sources. ^{1}H and ^{13}C spectra were recorded on Bruker AVance 300 and 500 MHz spectrometers. Chemical shifts are reported in delta (δ) units, expressed in parts per million (ppm) downfield from tetramethylsilane using the residual protio-solvent as an internal standard ($CDCl_3$,

^{1}H: 7.26 ppm, ^{13}C: 77.0 ppm). MS was performed on a Bruker Esquire equipped with an electrospray ionization (ESI) source. GPC setup consisted of: a Shimadzu pump, three in-line MZ Analysentechnik columns, DAWN Heleos II multi-angle laser light scattering and T-rEX refractive index detectors (Wyatt Technology Corporation), and DMF (0.01 M LiBr) as the mobile phase. UV-VIS spectroscopy was completed using an Agilent 8453 Diode Array UV-VIS Spectrometer.

4.4.2. Synthesis of Polymer 3.

Initiator **1** and polymer **3** were prepared following a reported procedure.[29]

4.4.3. Synthesis of Polymer 4.

A flame-dried and N_2-purged three-neck round bottom flask fitted with a reflux condenser was charged with initiator **2** (prepared as previously reported,[42] 268 mg, 0.76 mmol, 1.0 mol. equiv.) and a stir bar. To the reaction flask was then added ε-caprolactone (29.4 mL, 265 mmol, 350 mol. equiv.) and dry toluene (30.0 mL). Finally, $Sn(Oct)_2$ (80 μL, 0.251 mmol, 0.33 mol. equiv.) was added and the reaction solution was brought to refluxing temperature. After 24 h, the reaction solution was brought to 40 °C, diluted with toluene (~150 mL), and stirred until the polymer was fully dissolved. The polymer solution was then precipitated into an excess of cold MeOH, after which the precipitate was collected via vacuum filtration and then dried under reduced pressure. The PCL product was obtained as a brown solid in 96% yield (29.0 g).

4.4.4. Synthesis of Initiator 7.

Indole **5** (prepared as previously reported,[29] 266 mg, 1.31 mmol, 1.0 mol. equiv.) and salicylaldehyde **6** (prepared as previously reported,[43] 200 mg, 1.31 mmol, 1.0 mol. equiv.) were

dissolved in 5 mL of absolute ethanol. Piperidine (0.26 mL, 2.63 mmol, 2.0 mol. equiv.) was added and the solution brought to reflux. After 6 h the reaction was judged to be complete by TLC. The reaction was cooled to room temperature and diluted with 20 mL of ethyl acetate and washed successively with water (3 × 20 mL) and brine (1 × 10 mL). The organic layer was dried over $MgSO_4$ and concentrated under reduced pressure to yield **7** as a black crystalline solid in 91% yield (401 mg). ^{1}H NMR (300 MHz, $CDCl_3$) δ 7.17 (td, *J* = 7.7, 1.3 Hz, 1H), 7.11 – 7.05 (m, 3H), 6.86 (td, *J* = 7.4, 0.8 Hz, 1H), 6.83 (d, *J* = 10.2 Hz, 1H), 6.68 (d, *J* = 7.9 Hz, 1H), 6.63 (d, *J* = 7.8 Hz, 1H), 5.69 (d, *J* = 10.2 Hz, 1H), 4.57 (s, 2H), 3.79 – 3.70 (m, 2H), 3.56 – 3.45 (m, 1H), 3.40 – 3.26 (m, 1H), 1.30 (s, 3H), 1.17 (s, 3H). ^{13}C NMR (126 MHz, $CDCl_3$) δ 153.5, 147.3, 136.3, 132.9, 129.3, 129.0, 127.6, 125.9, 121.8, 119.9, 119.3, 118.6, 115.1, 106.6, 104.7, 64.9, 60.8, 52.3, 46.0, 25.8, 20.3. MS (ESI): $[M+H]^+$ calculated for $C_{21}H_{24}NO_3$, 338.18; found 338.4.

4.4.5. Synthesis of Polymer 8.

Polymer **8** was prepared in the same manner as described in *Synthesis of Polymer 4*, except using **7** as an initiator (**7** = 164 mg, 0.49 mmol,; ε-caprolactone = 18.84 mL, 170.1 mmol, 350 mol. equiv.; toluene = 20 mL; $Sn(Oct)_2$ = 0.05 mL, 0.16 mmol, 0.33 mol. equiv.). The polymer was obtained in 96% yield (18.7 g).

4.4.6. Filament Production.

Polymers **3** and **4** were mixed with Makerbot Flexible Filament (**C**) cut into small pieces, melted with a heat gun, and manually mixed with a spatula. After cooling, the resulting solid mixture was cut into small pieces with scissors and put into an electronically controlled burr mill with dry ice. The polymer was ground into particles no larger than 5 mm in diameter, and then made into

filament via melt extrusion (at 63 °C) with a Filabot Wee filament extruder. The filament $\mathbf{3}_{100}$ was produced without blending in any commercial filament **C**.

4.4.7. 3D Printing.

3D structures were designed and converted to .STL files using Sketchup 2013 CAD software. The .STL files were imported into Replicator G (version 0040) and G-code (for Makerbot class machines) was generated using either Slic3r 0.X (for single material prints) or Skeinforge 50 (for multi-material prints) slicing programs. Multi-material prints required generation of G-code for each component individually, followed by their merger using Replicator G. A Flashforge Creator dual-head FFF 3D printer (firmware 7.2) was used to read the G-code and print the 3D object. Objects were printed centered on a non-heated Plexiglas build plate with the long axis of the specimen aligned with the y-axis of the build plate (build space axes shown in Figure 33). Objects were built up in the vertical z-axis (as indicated for all parts in the Supporting Information). The outline of the specimen was printed first with its thickness depending on the number of shells. For the first layer, the extruded polymer was laid in alignment with the y-axis. For the second, the polymer was laid in alignment with the x-axis. The fill alignment continually alternates such that the layers above or below any one layer are perpendicular to each other. Extrusion nozzles were heated to 110 °C (filament was more prone to jamming at lower temperatures). Additional print parameters included: print speeds set to 20 mm/s, travel speed set to 50 mm/s, retraction disabled when applicable (i.e. when using Slic3r), 2 shells, fill density of 1 (i.e. 100% fill), and layer height of 0.25 mm. To ensure the most accurate filament diameter, each sample of filament was measured with calipers in multiple places along the section to be used for printing and the average diameter

was used in the print parameters. Dimensions of each printed specimen are provided in the Supporting Information.

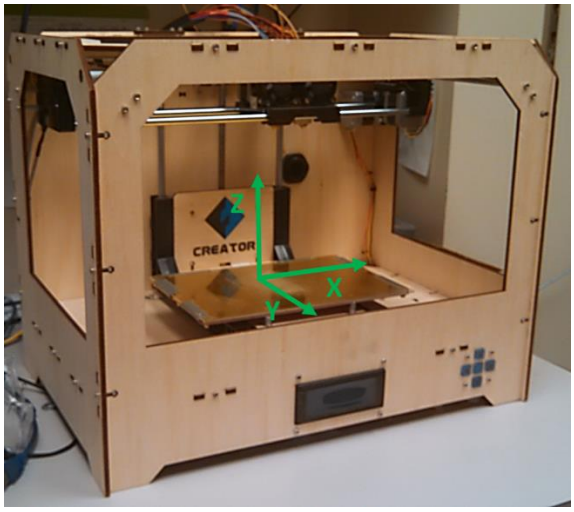

Figure 33. Flashforge Creator 3D printer. Axes of the build space are indicated by green arrows.

4.4.8. Mechanical Testing.

Tensile testing of printed specimens was performed on an Instron 5500R load frame with a 5 kN load cell controlled using Bluehill 3.0 software. All tests were conducted using a crosshead rate of 100 mm/min. Dimensions of each specimen were measured with calipers prior to testing to ensure accurate calculation of stress and strain for each sample. Three specimens were tested for a given filament type. Figure 34 shows a representative load versus extension curve for the tensile test specimens shown in Figure 26 in section 4.2.

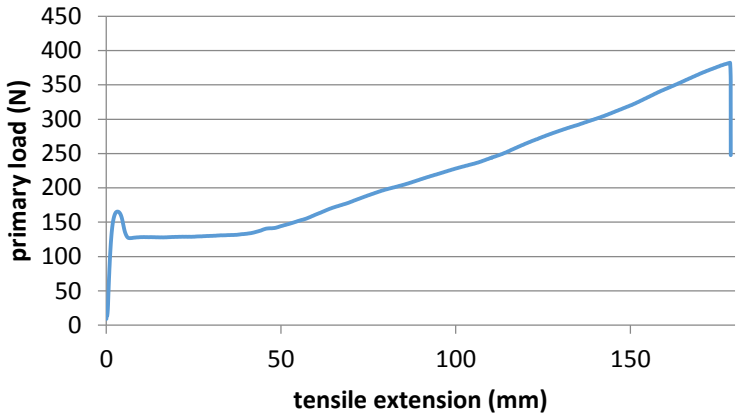

Figure 34. Plot of load versus extension for a representative symmetric tensile test specimen.

4.4.9. Force Sensor Testing

The force sensor was tested as in section 4.4.8. Sequential and predictable activation of each mechano-responsive region was observed within the specimen (Figure 35). As shown in Table 11, the onset of activation and the force corresponding to that activation was highly reproducible.

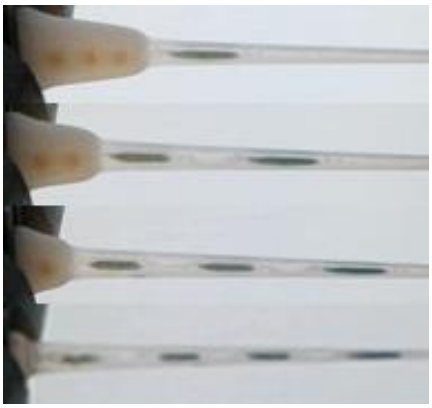

Figure 35. Images of the 4 mm force sensor undergoing elongation and sequential activation of the mechanoresponsive regions. The image at the top shows activation of the first region and the bottom image shows activation of the last region.

Table 11. Extension and load values for the onset of activation of each mechanoresponsive region. Values are an average of three runs ± one standard deviation.

Specimen Thickness (mm)	Mechanoresponsive Region Number	Average Extension (mm)	Average Primary Load (N)
1	1	42.7 ± 1.5	70.3 ± 2.5
	2	73.0 ± 1.0	89.3 ± 1.5
	3	103.3 ± 2.5	109.3 ± 1.5
	4	137.3 ± 2.1	127.7 ± 1.5
4	1	49.3 ± 4.0	272.7 ± 9.3
	2	82.7 ± 4.2	342.7 ± 11.4
	3	116.3 ± 6.4	411.0 ± 14.7
	4	152.0 ± 6.2	477.0 ± 9.0
7	1	54.3 ± 1.5	579.0 ± 10.0
	2	91.7 ± 2.1	722.3 ± 7.5
	3	127.3 ± 4.2	855.0 ± 18
	4	165.0 ± 5.3	998.7 ± 38.2

4.5. References

(1) Hofmann, M. *ACS Macro Lett.* **2014**, *3*, 382.

(2) Gross, B. C.; Erkal, J. L.; Lockwood, S. Y.; Chen, C.; Spence, D. M. *Anal. Chem.* **2014**, *86*, 3240.

(3) Jones, N. *Nature* **2012**, *487*, 22.

(4) Wang, X.; Guo, Q.; Cai, X.; Zhou, S.; Kobe, B.; Yang, J. *ACS Appl. Mater. Interfaces* **2014**, *6*, 2583.

(5) Bakarich, S. E.; Gorkin III, R.; in het Panhuis, M.; Spinks, G. M. *ACS Appl. Mater. Interfaces* **2014**, *6*, 15998.

(6) Khaled, S. A.; Burley, J. C.; Alexander, M. R.; Roberts, C. J. *Int. J. Pharm.* **2014**, *461*, 105.

(7) Yu, D.-G.; Shen, X.-X.; Branford-White, C.; Zhu, L.-M.; White, K.; Yang, X. L. *J. Pharm. Pharmacol.* **2009**, *61*, 323.

(8) Derby, B. *Science* **2012**, *338*, 921.

(9) Melchels, F. P. W.; Domingos, M. A. N.; Klein, T. J.; Malda, J.; Bartolo, P. J.; Hutmacher, D. W. *Prog. Polym. Sci.* **2012**, *37*, 1079.

(10) Billiet, T.; Vandenhaute, M.; Schelfhout, J.; Van Vlierberghe, S.; Dubruel, P. *Biomaterials* **2012**, *33*, 6020.

(11) Xu, N.; Ye, X.; Wei, D.; Zhong, J.; Chen, Y.; Xu, G.; He, D. *ACS Appl. Mater. Interfaces* **2014**, *6*, 14952.

(12) Zhao, C.; Wang, C.; Gorkin III, R.; Beirne, S.; Shu, K.; Wallace, G. G. *Electrochem. Commun.* **2014**, *41*, 20.

(13) Sun, K.; Wei, T.-S.; Ahn, B. Y.; Seo, J. Y.; Dillon, S. J.; Lewis, J. A. *Adv. Mater.* **2013**, *25*, 4539.

(14) Mannoor, M. S.; Jiang, Z.; James, T.; Kong, Y. L.; Malatesta, K. A.; Soboyejo, W. O.; Verma, N.; Gracias, D. H.; McAlpine, M. C. *Nano Lett.* **2013**, *13*, 2634.

(15) Leigh, S. J.; Bradley, R. J.; Purssell, C. P.; Billson, D. R.; Hutchins, D. A. *PLoS ONE* **2012**, *7*, e49365;

(16) Czyzewski, J.; Burzynski, P.; Gawel, K.; Meisner, J. *J. Mater. Process. Tech.* **2009**, *209*, 5281.

(17) Espalin, D.; Muse, D.; MacDonald, E.; Wicker, R. *Int. J. Adv. Manuf. Technol.* **2014**, *72*, 963.

(18) Muth, J. T.; Vogt, D. M.; Truby, R. L.; Menguc, Y.; Kolesky, D. B.; Wood, R. J.; Lewis, J. A. *Adv. Mater.* **2014**, *26*, 6307.

(19) Kim, K.; Zhu, W.; Qu, X.; Aaranson, C.; McCall, W. R.; Chen, S.; Sirbuly, D. J. *ACS Nano.* **2014**, *8*, 9799.

(20) Peterson, G. I.; Yurtoglu, M.; Larsen, M. B.; Craig, S. L.; Ganter, M. A.; Storti, D. W.; Boydston, A. J. Additive Manufacturing of Mechanochromic Polycaprolactone on Entry-Level Systems. *Rapid Prototyping J.* **2014**, accepted.

(21) Wiggins, K. M.; Brantley, J. N.; Bielawski, C. W. *Chem. Soc. Rev.* **2013**, *42*, 7130.

(22) Brantley, J. N.; Wiggins, K. M.; Bielawski, C. W. *Polym. Int.* **2012**, *62*, 2.

(23) Caruso, M. M.; Davis, D. A.; Shen, Q.; Odom, S. A.; Sottos, N. R.; White, S. R.; Moore, J. S. *Chem. Rev.* **2009**, *109*, 5755.

(24) Beyer, M. K.; Clausen-Schaumann, H. *Chem. Rev.* **2005**, *105*, 2921.

(25) Gossweiler, G. R.; Hewage, G. B.; Soriano, G.; Wang, Q.; Welshofer, G. W.; Zhao, X.; Craig, S. L. *ACS Macro Lett.* **2014**, *3*, 216.

(26) Grady, M. E.; Beiermann, B. A.; Moore, J. S.; Sottos, N. R. *ACS Appl. Mater. Interfaces* **2014**, *6*, 5350.

(27) Lee, C. K.; Beiermann, B. A.; Silberstein, M. N.; Wang, J.; Moore, J. S.; Sottos, N. R.; Braun, P. V. *Macromolecules* **2013**, *46*, 3746.

(28) Beiermann, B. A.; Kramer, S. L. B.; Moore, J. S.; White, S. R.; Sottos, N. R. *ACS Macro Lett.* **2012***, 1*, 163.

(29) O'Bryan, G.; Wong, B. M.; McElhanon, J. R. *ACS Appl. Mater. Interfaces* **2010**, *2*, 1594.

(30) Davis, D. A.; Hamilton, A.; Yang, J.; Cremar, L. D.; Van Gough, D.; Potisek, S. L.; Ong, M. T.; Braun, P. V.; Martinez, T. J.; White, S. R.; Moore, J. S.; Sottos, N. R. *Nature* **2009**, *459*, 68.

(31) Chen, Y.; Spiering, A. J. H.; Karthikeyan, S.; Peters, G. W. M.; Meijer, E. W.; Sijbesma, R. P. *Nat. Chem.* **2012**, *4*, 559.

(32) Ducrot, E.; Chen, Y.; Bulters, M. J. H.; Sijbesma, R. P.; Creton, C. *Science* **2014**, *344*, 186.

(33) Jakobs, R. T. M.; Ma, S.; Sijbesma, R. P. *ACS Macro Lett.* **2013**, *2*, 613.

(34) Black Ramirez, A. L.; K.; Z. S.; Orlicki, J. A.; Champhekar, M.; Elsakr, S. M.; Krause, W. E.; Craig, S. L. *Nat. Chem.* **2013**, *5*, 757.

(35) Larsen, M. B.; Boydston, A. J. *J. Am. Chem. Soc.* **2014**, *136*, 1276.

(36) Larsen, M. B.; Boydston, A. J. *J. Am. Chem. Soc.* **2013**, *135*, 8189.

(37) Diesendruck, C. E.; Steinberg, B. D.; Sugai, N.; Silberstein, M. N.; Sottos, N. R.; White, S. R.; Braun, P. V.; Moore, J. S. *J. Am. Chem. Soc.* **2012**, *134*, 12446.

(38) Eshraghi, S.; Das, S. *Acta Biomater.* **2010**, *6*, 2467.

(39) Keum, S.-R.; Lee, K.-B.; Kazmaier, P. K.; Buncel, E. *Tetrahedron Lett.* **1994**, *35*, 1015.

(40) Keum, S.-R.; Lee, M.-J. *Bull. Korean Chem. Soc.* **1999**, *20*, 1464.

(41) Aramaki, S.; Atkinson, G. H. *J. Am. Chem. Soc.* **1992**, *114*, 438.

(42) Raymo, F. M.; Giordani, S. *J. Am. Chem. Soc.* **2001**, *123*, 4651.

(43) Frédérick, R.; Robert, S.; Charlier, C.; de Ruyck, J.; Wouters, J.; Pirotte, B.; Masereel, B.; Pochet, L. *J. Med. Chem.* **2005**, *48*, 7592.

Chapter 5 – 1,2-Oxazine Linker as a Thermal Trigger for Self-Immolative Polymers

5.1. Introduction

Self-immolative polymers (SIPs) comprise an exciting class of functional macromolecules capable of head-to-tail depolymerization in response to an external stimulus.[1-3] The single triggering event that typically occurs at the chain end results in an amplified response as multiple repeat units are sequentially released from the activated polymer (Figure 36). The selectivity and efficiency of triggering reactions are key to the successful deployment of SIPs in diverse applications including their potential use in sensory materials, drug delivery platforms, and lithographic plastics. Moreover, incorporation of triggering groups enables site-specificity during activation and potential tunability in the rate of activation. The variety of trigger designs for self-immolative polymers, dendrimers, and oligomers collectively utilize pH-, redox-, enzyme-, nucleophile-, and photo-mediated activation.[1c] While general thermal triggers for chemical reactions are well established,[4] many are not capable of activating SIPs and, to our knowledge, none have been demonstrated for this purpose.

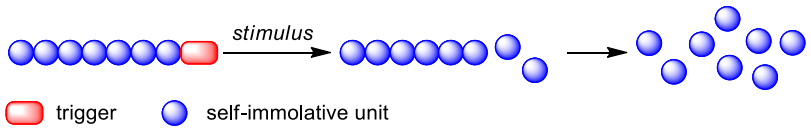

Figure 36. Generalized process for a SIP undergoing stimulus-triggered depolymerization.

Thermally-activated SIPs may have practical advantages in the biomedical arena considering the techniques that are available for controlled localized heating. For example, photothermal[5] or magnetothermal[6] transduction, or focused ultrasound[7] may be viable methods for triggering depolymerization of SIPs with excellent spatiotemporal control. Additionally, passive activation at physiological temperatures may provide a simplified method for accomplishing sustained release of therapeutics, potentially mimicking continuous infusion with single, infrequent injections of drug-releasing SIPs.

Amidst relatively broad structural variations and sensitivities to stimuli, a unifying theme for SIP trigger reactivity is to unveil an electron-releasing functional group at the chain end of the SIP. The electron-releasing nature of the active chain end typically initiates a cascade of elimination or substitution reactions that depolymerize the macromolecule in a unidirectional, head-to-tail fashion. This mechanism of activation contrasts that of the thermal activation of low ceiling temperature polymers. For instance, when heated above ca. 150 °C, poly(phthalaldehyde) undergoes random mid-chain thermolysis and bidirectional depolymerizaiton.[8]

Inspired by the investigations of Kirby and King involving hydroxyurea and oxidized derivatives thereof, we envisioned substituted 1,2-oxazines may be good candidates for thermal triggers.[9] We anticipated the cycloreversion of a substituted 1,2-oxazine on the chain end of a SIP (e.g., **1**, Scheme 3) would result in a hydrolytically unstable carbamoylnitroso intermediate (**2**), as demonstrated for small molecule 1,2-oxazines.[9] Following hydrolysis of **2** and rapid decarboxylation of carbamic acid **3**, a free amine would be generated at the SIP chain end (e.g., **4**). A practical approach to installing oxazines involves oxidation of hydroxyureas and in situ trapping via [4+2] cycloaddition reactions with various dienes.[9,10] This cycloaddition was also recently shown to be a useful reaction for the conjugation of carbonylnitroso and diene end group-

functionalized polymers.[11] Herein, we describe the synthesis and evaluation of a viable thermal trigger for a versatile class of SIPs.

Scheme 3. Proposed mechanism of action of a thermally-activated SIP trigger.

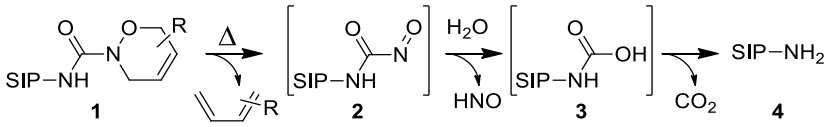

5.2. Results and Discussion

We considered polyurethane-based SIPs derived from *p*-aminobenzyl alcohol to be an attractive and versatile platform since they can be readily adapted for small-molecule release from side chain functionalities, turn-on fluorescence reporting, and solubility in water.[1] Thus, our first synthetic target was a polyurethane-based SIP with a hydroxyurea end cap. Beginning from phenyl carbamate **5** (Scheme 4), polymerization was conducted using Et_3N as a mediator at 60 °C in dry dimethylsulfoxide (DMSO). We found these polymerization conditions to be more successful for our particular end group functionalization than Sn(IV)-mediated polymerizations,[2] albeit at the expense of slightly longer polymerization times. The hydroxyurea moiety was incorporated into the polymer by capping with NH_2OH after complete monomer consumption was observed as determined by ^{1}H NMR spectroscopy. Analysis via ^{1}H NMR spectroscopy of various experiments revealed the resulting SIP **6** to have average degrees of polymerization (DPs) of 8 – 12.

Scheme 4. Synthesis of SIP **6.**

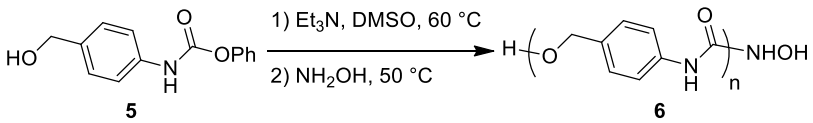

We next determined the extent to which formation and subsequent decomposition of the carbamoylnitroso end group would lead to SIP depolymerization. Toward this end, SIP **6** was subjected to conditions known to oxidize hydroxyureas directly to carbamoylnitroso intermediates.[10-12] Specifically, wet DMSO-d_6 (10% D_2O by volume) solutions of SIP **6** were treated with tetrabutylammonium periodate (TBAP) or CuCl and pyridine and monitored by ^1H NMR spectroscopy; key data are summarized in Table 12. Upon exposure to oxidizing conditions, we observed gradual depletion of the SIP **6** repeat units (entries 1 through 4). As expected, using anhydrous DMSO-d_6 resulted in depolymerization to a lesser extent (entries 5 through 8). Control experiments confirmed the need for oxidative conditions, indicating that hydrolysis was not occurring directly on the polymer main chain or end group (entries 9 and 10). These results indicated to us that if the carbamoylnitroso species could be liberated by cycloreversion of an oxazine on the chain end of a SIP, then thermally triggered depolymerization could be achieved. It is noteworthy that while a variety of hydroxyureas have been shown to undergo oxidative decomposition,[12] we are unaware of any reports on this reactivity being demonstrated for the activation of SIPs.

Table 12. Oxidation and depolymerization of SIP **6.**

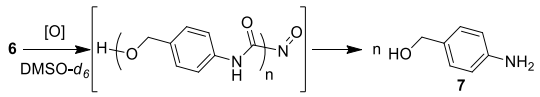

entry	conditions	time (h)	% depolymerization[a]
1	TBAP, D_2O	25	50
2	TBAP, D_2O	100	67
3	CuCl, pyridine, D_2O	25	42
4	CuCl, pyridine, D_2O	100	69
5	TBAP	25	11
6	TBAP	100	24
7	CuCl, pyridine	25	0
8	CuCl, pyridine	100	2
9	D_2O	25	1
10	D_2O	100	6

[a]The % depolymerization = 100 - % SIP repeat units remaining, as determined by ^{1}H NMR spectroscopy using 1,4-dicyanobenzene as an internal standard.

We next focused on installing the oxazine at the triggering position of the SIP (Scheme 5). We targeted a cyclopentadiene derivative as the diene constituent of the oxazine as they are known to provide good stability and mild cycloreversion temperaures.[9,11] Initiator **9** was prepared from pentamethylcyclopentadiene and used for atom-transfer radical polymerization of *N*,*N*-dimethylacrylamide (DMA), providing poly(*N*,*N*-dimethylacrylamide) (PDMA) **10**. A diblock was prepared in order to aid with purification, as the product would have disparate solubility from any free SIP. Treatment of **10** with **6** in a 1:2 ratio under oxidative conditions provided complete end capping of **10** to yield diblock copolymer **11**. Attempted coupling with a 1:1 ratio of the two resulted in mixtures of free SIP and PDMA in addition to **11**. Removal of residual **6** was accomplished by precipitation into CH_2Cl_2 followed by filtration through Celite/alumina. Notably, the selective precipitation of the unreacted SIP circumvents issues associated with incomplete chain end functionalization or oxidation to the carbamoylnitroso species. GPC and ^{1}H NMR

analysis supported the successful 1:1 conjugation of the SIP and PDMA blocks. To evaluate the extent to which hydrolysis may be giving rise to background triggering of the SIP, we prepared control polymer **14** in which the trigger moiety is absent.

Scheme 5. Synthesis of diblock copolymers **11** and **14.**

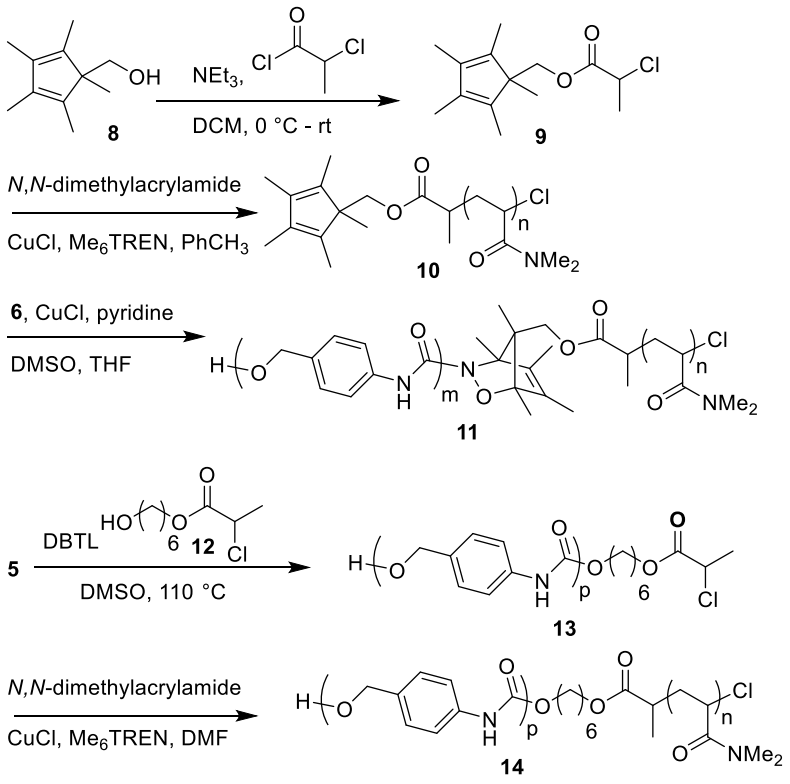

To avoid complications arising from insolubility of the SIP block after detachment from the PDMA, we conducted thermal triggering and depolymerization experiments in DMSO-d_6/D_2O mixtures (9:1 v/v). Figure 37 shows the amount of SIP depolymerization over time as **11** and **14** were heated at various temperatures. At a long-term storage temperature of 4 °C we saw negligible activity from **11** in solution over the course of 50 d. At room temperature (RT), however, we observed gradual activation leading to 22% depolymerization after 65 d. As expected, at 40 °C

more rapid activation and depolymerization was observed, reaching 61% depolymerization after ca. 71 d. At 60 and 85 °C, nearly full depolymerization was observed after ca. 47 and 5 d, respectively. We observed only 17% or 18% depolymerization when **14** was heated at RT or 40 °C for 81 d, respectively. At 60 and 85 °C, the rate of depolymerization was clearly much less for **14** than for the oxazine trigger variant (**11**), consistent with different mechanisms of activation between the two. The results from the control polymer suggest that hydrolysis plays a fairly significant role in the degradation of the SIP above 60 °C.

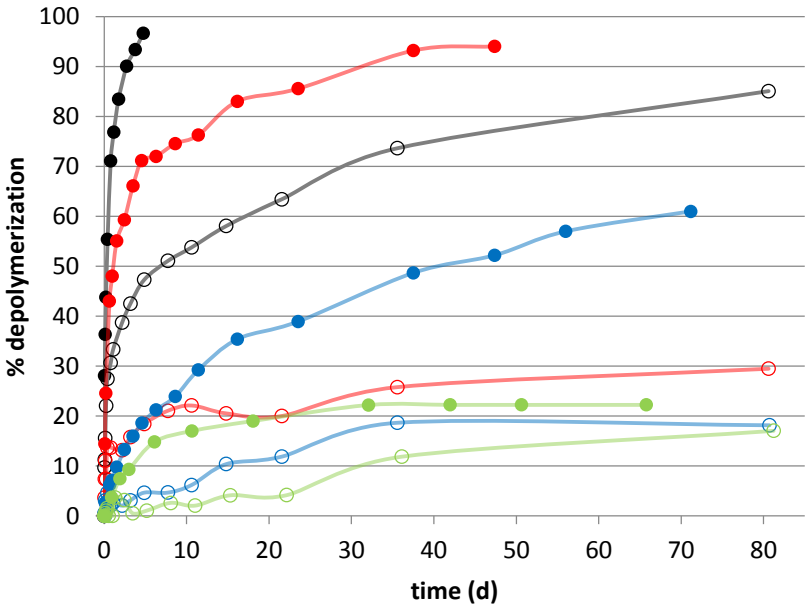

Figure 37. Thermal activation and depolymerization of SIPs **11** (filled circles) and **14** (empty circles) in DMSO-d_6/D_2O (9:1 v/v) at 85 °C (●,○), 60 °C (●,○), 40 °C (●,○), and RT (●,○1). The % depolymerization = 100 - % SIP repeat units remaining, as determined by ^{1}H NMR spectroscopy using 1,4-dicyanobenzene as an internal standard. Average of two runs. The colored lines are for visual aid only.

Additional confirmation of the oxazine trigger reactivity was obtained from thermolysis of **11** in the presence of excess 1,3-cyclohexadiene (Scheme 6). Specifically, heating **11** at 60 °C in DMSO-d_6/D_2O (9:1 v/v) containing 300 equivalents (ca. 1.7% by volume) of 1,3-cyclohexadiene relative to oxazine trigger significantly suppressed the rate of depolymerization (see Figure 38 in section 5.4.13.). Only 20% depolymerization was observed after 2 d, versus nearly 60% for **11** at the same time and temperature. These results are consistent with the intermediacy of a carbamoylnitroso species and formation of the more thermally stable cyclohexadiene adduct. ^{1}H NMR analysis also revealed increasing intensities of resonances centered at $\delta = 4.80$ ppm that were consistent with bridgehead protons of the cyclohexadiene-based oxazine (see Figure 39 in section 5.4.13.).

Scheme 6. Diene transfer supports carbamoylnitroso intermediate.

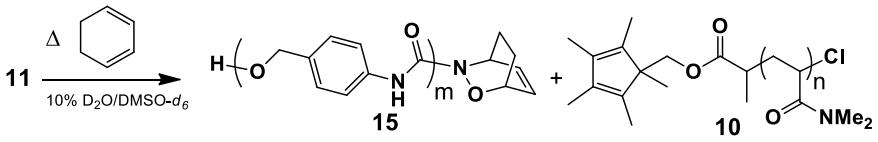

5.3. Conclusions

In summary, we have demonstrated a new class of SIP trigger that is responsive to mild thermal impetus. Our trigger comprises a bicyclic oxazine that is an efficient source of an electron rich functionality necessary for initiating depolymerization. Diene transfer studies support the proposed mechanism of a carbamoylnitroso intermediate. The temperature-dependent triggering provides an exciting approach for future on-demand SIP activation.

5.4. Experimental

5.4.1. Materials

Dry DMSO, tetrahydrofuran (THF), toluene, and CH_2Cl_2 were obtained from a Glass Contour solvent purification system. Et_3N and DMA were distilled after drying over CaH_2 overnight. TBAP was dried with P_2O_5 overnight before use. House N_2 was passed through a drying tube before use. Self-immolative monomer **5** was prepared as previously described.[2] All other reagents and solvents were used as obtained from commercial sources.

5.4.2. Synthesis of 6

A flame-dried round-bottom flask under N_2 was charged with 6 g (24.6 mmol, 1.0 mol. equiv.) of **5** and a stir bar. Dry DMSO (12.3 mL, **5** at 2.0 M) and dry Et_3N (3.5 mL, 24.7 mmol, 1.0 mol. equiv.) were then added. The solution was heated at 60 °C for 2.5 h. At that time, a small aliquot was removed and the DP was determined by ^1H NMR spectroscopy by comparing the areas of the peaks corresponding to end groups and repeat units. To the reaction mixture was then added hydroxylamine (16.8 mmol, 5.0 mol. equiv. relative to end group) from a 1.0 M stock solution prepared in dry DMSO. The resulting mixture was stirred for 6 h at 50 °C. The reaction mixture was then poured into MeOH (approximately 10 times the volume of DMSO) and cooled in a refrigerator causing precipitation of the polymer. The precipitate was collected on a sintered-glass Büchner funnel and dried under vacuum. The yield was 89% by mass recovery. An average run yields 90-100% capped SIP. Technical note: The hydroxylamine solution was prepared by combining hydroxylamine hydrochloride (20 mmol) with anhydrous K_2CO_3 (40 mmol) in dry DMSO (20 mL, hydroxylamine at 1.0 M). The mixture was stored at RT for 12 h prior to use.

5.4.3. Synthesis of 8

To a flame-dried, N_2-purged three neck round-bottom flask, fit with a condenser, was added paraformaldehyde (580 mg) and dry THF (10.5 mL). The resulting suspension was refluxed under N_2 for 2 h and then cooled to RT. To a separate flame-dried, N_2-purged round bottom flask was added 1,2,3,4,5-pentamethylcyclopentadiene (0.6 mL, 3.83 mmol, 1.0 mol. equiv.), tetrabutylammonium iodide (140 mg, 0.38 mmol, 0.1 mol. equiv.), dry THF (8.0 mL), and a stir bar. The solution was cooled to 0 °C and n-butyllithium (2.33 M, 4.6 mmol, 1.2 equiv) was added dropwise. A white precipitate immediately began to form. The suspension was stirred for 45 min at 0 °C, then paraformaldehyde from the previously refluxed solution (230 mg, 7.66 mmol, 2.0 mol. equiv.) was added and stirred for 18 h, letting the ice bath expire. The solvent was then removed under reduced pressure and the solids were redissolved/resuspended in diethyl ether. This mixture was washed sequentially with 1.0 M HCl, sat. $NaHCO_3$ aq., and H_2O. The organic solution was dried over Na_2SO_4 and the solvent was removed under reduced pressure. The crude mixture was then purified by flash column chromatography to give a transparent light yellow oil in 56% yield. ^{1}H NMR (300 MHz, $CDCl_3$) δ 3.50 (s, 2H), 1.77 (d, J = 18.8 Hz, 12H), 0.87 (s, 3H). ^{13}C NMR (126 MHz, $CDCl_3$) δ 138.03 (s), 136.22 (s), 65.27 (s), 58.40 (s), 16.80 (s), 11.28 (s), 9.70 (s).

5.4.4. Synthesis of 9

A flame-dried round bottom flask under nitrogen was charged with **8** (679 mg, 4.08 mmol, 1.0 mol. equiv.), dry CH_2Cl_2 (18.0 mL), and a stir bar. The solution was cooled to 0 °C and Et_3N (0.63 mL, 4.49 mmol, 1.1 mol. equiv.) was added. A solution of 2-chloropropionyl chloride (0.44 mL, 4.49 mmol, 1.1 mol. equiv.) in dry CH_2Cl_2 (6.0 mL) was made prepared under a N_2 atmosphere

and added dropwise to the solution containing **8**. The reaction mixture was stirred for 18 h, letting the ice bath expire. The reaction solvent was then removed under reduced pressure and the solids were redissolved/resuspended in diethyl ether. This mixture was washed sequentially with sat. $NaHCO_3$ aq., and H_2O. The organic solution was dried over Na_2SO_4 and the solvent was removed under reduced pressure to give a yellow/brown oil. The product was isolated by flash column chromatography to obtain a transparent yellow oil in 71% yield. ^{1}H NMR (300 MHz, $CDCl_3$) δ 4.31 (m, *J* = 13.9, 7.0 Hz, 1H), 4.05 (q, *J* = 10.7 Hz, 2H), 1.75 (s, 12H), 1.59 (d, *J* = 7.0 Hz, 3H), 0.96 (s, 3H). ^{13}C NMR (75 MHz, $CDCl_3$) δ 170.00 (s), 138.35 (s), 135.41 (s), 68.89 (s), 55.70 (s), 52.90 (s), 21.72 (s), 16.81 (s), 11.18 (s), 10.30 (s).

5.4.5. Synthesis of 10

Freshly distilled DMA (11.2 mL, 109 mmol, 350 mol. equiv. to initiator), CuCl (92 mg, 0.93 mmol, 3.0 mol. equiv.), and dry toluene (10.0 mL) were added to a Schlenk tube in a glove box. The reaction solution underwent three freeze-pump-thaw cylces, after which tris[2-(dimethylamino)ethyl]amine (Me_6TREN) (0.25 mL, 0.93 mmol, 3.0 mol. equiv.) was added and stirred for 30 min. Lastly, **9** (82 mg, 0.31 mmol, 1.0 mol. equiv.) was added and the polymerization was stirred for 5 h at RT. The reaction solution was diluted with THF and put through an alumina plug. The polymer solution was concentrated under vacuum and redissolved in approximately 4 mL of CH_2Cl_2. A sat. ethylenediaminetetraacetic acid (EDTA) aq. solution (1.0 mL) was added and the layers were stirred vigorously so that remaining copper would be absorbed into the aqueous layer. Na_2SO_4 was then added to dry the solution. The remaining solids were removed by filtration and the solvent was removed from the solution under reduced pressure. The resulting oily polymer residue was then redissolved in a minimal volume of pyridine and precipitated into ether

(approximately 10 times the volume of the polymer solution). The precipitate was collected on a sintered-glass Büchner funnel and dried under vacuum. An off-white powder was recovered in 65% yield (7.0 g). M_n =26.5 kDa, PDI = 1.07.

5.4.6. Synthesis of 11

A flame-dried round-bottom flask was charged with SIP **6** (138 mg, 0.086 mmol, 2.0 mol. equiv.) and dry DMSO (10.0 mL). Once the SIP fully dissolved, **10** (1.08 g, 0.043 mmol, 1.0 mol. equiv.) and THF (10.0 mL) were added followed by CuCl (34 mg, 0.34 mmol, 0.8 mol. equiv.) and pyridine (7 μL, 0.086 mmol, 0.2 mol. equiv.). The reaction solution was stirred (open to air) for 24 h at RT. The solution was then precipitated into CH_2Cl_2 and filtered through a celite/alumina plug in a sintered-glass Büchner funnel. The CH_2Cl_2 was then removed under reduced pressure and the remaining DMSO/polymer solution was added into diethyl ether. The polymer oiled out on bottom of flask. After decanting away the ether solution, the polymer was dissolved in a minimal volume of CH_2Cl_2 and precipitated into ether. The precipitate was collected on a sintered-glass Büchner funnel then dried under vacuum. A slightly off-white powder was recovered in 37% yield (402 mg). M_n =31.3 kDa, PDI = 1.03.

5.4.7. Synthesis of 12

A flame-dried round bottom flask under N_2 atmosphere was charged with 1,6-hexanediol (4.0 g, 33.84 mmol, 6.0 mol. equiv.), dry CH_2Cl_2 (24.0 mL), and a stir bar. The solution was cooled to 0 °C and Et_3N (0.79 mL, 5.64 mmol, 1.0 mol. equiv.) was added. A solution of 2-chloropropionyl chloride (0.55 mL, 5.64 mmol, 1.0 mol. equiv.) in dry CH_2Cl_2 (6.0 mL) was prepared under N_2 atmosphere and added dropwise to the solution containing the diol. The reaction mixture was

stirred for 18 h, letting the ice bath expire. The reaction solvent was then removed under reduced pressure and the solids were redissolved/resuspended in diethyl ether. This mixture was washed sequentially with sat. $NaHCO_3$ aq., and H_2O. The organic solution was dried over Na_2SO_4 and the solvent was removed under reduced pressure. The product was isolated by flash column chromatography (50% EtOAc/Hex) to obtain a transparent colorless oil in 52% yield. ^{1}H NMR (300 MHz, DMSO) δ 4.70 (q, *J* = 6.8 Hz, 1H), 4.33 (t, *J* = 5.2 Hz, 1H), 4.12 (t, *J* = 6.6 Hz, 2H), 3.37 (dd, *J* = 11.6, 6.3 Hz, 2H), 1.58 (m, 5H), 1.41 (m, 2H), 1.31 (m, 4H). ^{13}C NMR (126 MHz, DMSO) δ 169.54 (s), 65.41 (s), 60.56 (s), 52.77 (s), 32.34 (s), 27.93 (s), 25.07 (s), 25.05 (s), 21.18 (s).

5.4.8. Synthesis of 13

A flame-dried round bottom flask under N_2 atmosphere was charged with self-immolative monomer **5** (300.0 mg, 1.23 mmol, 1.0 mol. equiv.), dry DMSO (0.6 mL), and a stir bar. Alcohol **12** (31.0 mg, 0.12 mmol, 0.1 mol. equiv.) and dibutyltin dilaurate (DBTL) (36.0 µL, 0.06 mmol, 0.06 mol. equiv.) were added. The reaction mixture was then placed on heat at 110 °C for 2 hours. The reaction mixture was then poured into MeOH (approximately 10 times the volume of DMSO) and cooled in a refrigerator causing precipitation of the polymer. The precipitate was collected on a sintered-glass Büchner funnel and dried under vacuum. The yield was 56% by mass recovery. The SIP was ca. 81% capped with alcohol **12** and had a DP of ca. 10.

5.4.9. Synthesis of 14

Freshly distilled DMA (1.5 mL, 15.0 mmol, 300 mol. equiv. to initiator), CuCl (14.8 mg, 0.15 mmol, 3.0 mol. equiv.), and dry DMF (1.5 mL) were added to a Schlenk tube in a glove box. The

reaction solution underwent three freeze-pump-thaw cycles, after which Me_6TREN (40.2 µL, 0.15 mmol, 3.0 mol. equiv.) was added and stirred for 30 min. Lastly, **13** (87.2 mg, 0.05 mmol, 1.0 mol. equiv.) was added and the polymerization was stirred for 14 h at RT. The solution was then precipitated into diethyl ether. The solids were collected and redissolved in CH_2Cl_2. This solution was filtered through a Celite/alumina plug in a sintered-glass Büchner funnel. The solution was then concentrated and again precipitated into diethyl ether. The precipitate was collected on a sintered-glass Büchner funnel and dried under vacuum. The polymer was obtained in 60% yield. M_n=14.9 kDa, PDI = 1.33.

5.4.10. Synthesis of 15

A flame-dried round-bottom flask was charged with SIP **6** (100 mg, 0.091 mmol, 1.0 mol. Equiv.), 1,3-cyclohexadiene (0.36 mL, 4.55 mmol, 50 mol. Equiv.) and a stir bar. The mixture was dissolved in dry DMSO (1.6 mL) and THF (0.4 mL). CuCl (7.12 mg, 0.072 mmol, 0.8 mol. Equiv.) and pyridine (1.45 µL, 0.2 mol. Equiv.) were then added. After 16 h of stirring (open to air) at RT, the reaction mixture was poured into MeOH (approximately 10 times the volume of DMSO) and cooled in a refrigerator causing precipitation of the polymer. The precipitate was collected on a sintered-glass Büchner funnel, washed with CH_2Cl_2 and dried under vacuum. The product (shown in Scheme 7) was obtained in 65% yield with 60% of the chain ends bearing the desired adduct.

Scheme 7. Synthesis of **15**.

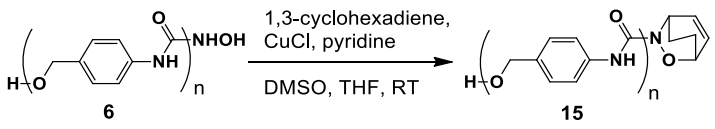

5.4.11. General Method for Oxidation Experiments With SIP 6

SIP **6** (20 mg, 0.0083 mmol, 1.0 mol. Equiv.) was dissolved in anhydrous DMSO-d_6 (0.45 mL) under a N_2 atmosphere and transferred to a NMR tube. Next, either TBAP (5.4 mg, 0.012 mmol, 1.5 mol. Equiv.) or CuCl (0.4 mg, 0.004 mmol, 0.5 mol. Equiv.) and pyridine (0.2 µL, 0.002 mmol, 0.25 mol. Equiv.) were added. Lastly, 1,4-dicyanobenzene (ca. 0.7 mg as an internal standard), and D_2O (0.05 mL) were added and the NMR tube was capped and sealed with electrical tape. The sample was then heated at 40 °C and the depolymerization was monitored by ^{1}H NMR spectroscopy. The % of SIP repeat units remaining was determined by monitoring the benzylic protons of the carbamate repeat unit (δ = 5.05 ppm) versus the internal standard. Control experiments without D_2O (using 0.5 mL of DMSO-d_6) and with only the SIP and D_2O were also completed under the same conditions.

5.4.12. General Method for Monitoring the Thermally Triggered Depolymerization of 11

Diblock copolymer **11** (20 mg) was dissolved in anhydrous DMSO-d_6 (0.9 mL, SIP repeat units at 7 mM concentration) and transferred to a screw-cap NMR tube. D_2O (0.1 mL) and 1,4-dicyanobenzene (1 mg as an internal standard) were then added. A time-zero ^{1}H NMR spectrum was collected. The NMR tube was then immersed in a pre-heated oil bath set to the desired temperature and the depolymerization progress was monitored at various time points by ^{1}H NMR spectroscopy.

5.4.13. Diene Transfer With 11

Diblock copolymer **11** (20 mg, 1.0 mol. equiv.) was dissolved in anhydrous DMSO-d_6 (0.88 mL) and transferred to a screw cap NMR tube. D_2O (0.1 mL), 1,3-cyclohexadiene (0.019 mL, 300 mol.

equiv.) and 1,4-dicyanobenzene (1 mg as an internal standard) were then added. A time-zero ^{1}H NMR spectrum was collected. The NMR tube was then immersed in a pre-heated oil bath set to 60 °C and the depolymerization progress was monitored at various time points by ^{1}H NMR spectroscopy. As shown in Figure 38, the rate of depolymerization for diblock copolymer **11** was significantly decreased with the addition of 1,3-cyclohexadiene at 60 °C. The stacked NMR spectra for the diene transfer experiment are shown in Figure 39. The spectra show the benzylic CH_2 end group of the SIP at 4.37 ppm, the benzylic CH_2 repeat unit of the SIP at 5.03 ppm, and the bridgehead CH protons of the 1,3-cyclohexadiene adduct at 4.80 ppm (if present). The appearance of the peaks at 4.80 ppm in the middle plot confirms that the adduct has been produced in the diblock diene transfer experiment.

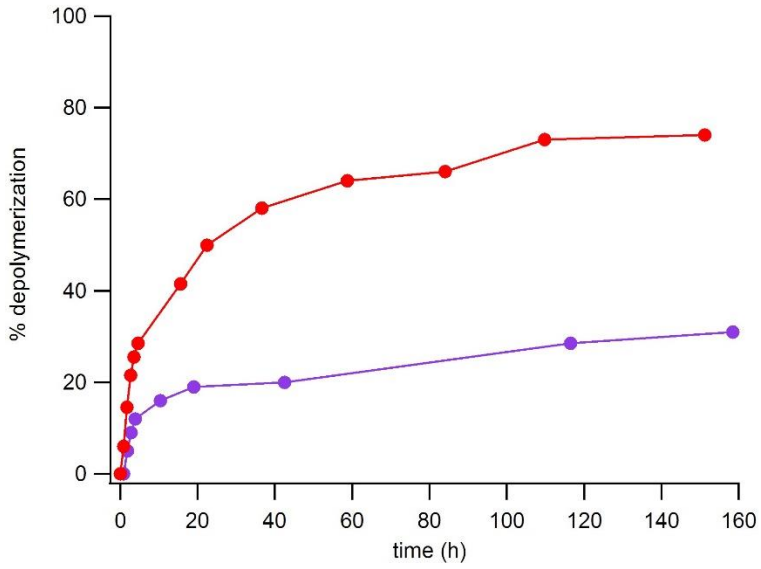

Figure 38. Thermal activation and depolymerization of SIP **11** in DMSO-d_6/D_2O (9:1 v/v) at 60 °C with (●) or without (●) 1,3-cyclopentadiene. The % depolymerization = 100 - % SIP repeat units remaining, as deter-mined by ^{1}H NMR spectroscopy using 1,4-dicyanobenzene as an internal standard. The colored lines are for visual aid only.

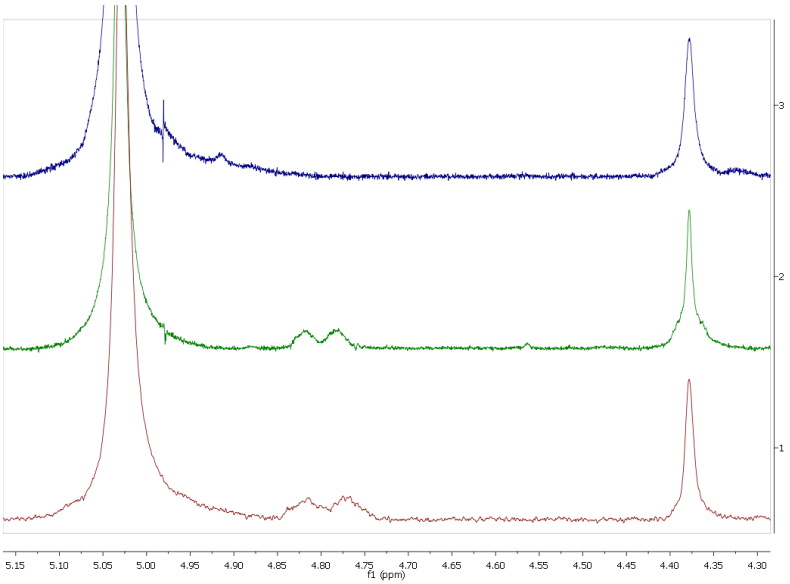

Figure 39. ^{1}H NMR spectra of the diblock copolymer **11** prior to the diene transfer experiment (top), **11** after heating in the presence of 1,3-cyclohexadiene for 19 h (middle), and SIP **15** (bottom).

5.5. References

(1) For recent reviews, see: (a) Phillips, S. T.; Robbins, J. S.; DiLauro, A. M.; Olah, M. G. *J. Appl. Polym. Sci.* **2014**, DOI: 10.1002/APP.40992. (b) Phillips, S. T.; DiLauro, A. M. *ACS Macro Lett.* **2014**, *3*, 298. (c) Peterson, G. I.; Larsen, M. B.; Boydston, A. J. *Macromolecules* **2012**, *45*, 7317.

(2) For the first example of a SIP, see: Sagi, A.; Weinstain, R.; Karton, N.; Shabat, D. *J. Am. Chem. Soc.* **2008**, *130*, 5434.

(3) For recent SIP examples, see: (a) Fan, B.; Trant, J. F.; Wong, A. D.; Gillies, E. R. *J. Am. Chem. Soc.* **2014**, *136*, 10116. (b) Liu, G.; Wang, X.; Hu, J.; Zhang, G.; Liu, S. *J. Am. Chem. Soc.* **2014**, *136*, 7492. (c) Zhang, L.-J.; Deng, X.-X.; Du, F.-S.; Li, Z.-C. *Macromolecules* **2013**, *46*,

9554. (d) McBride, R. A.; Gillies, E. R. *Macromolecules* **2013**, *46*, 5157. (e) DiLauro, A. M.; Zhang, H.; Baker, M. S.; Wong, F.; Sen, A.; Phillips, S. T. *Macromolecules* **2013**, *46*, 7257. (f) Olah, M. G.; Robbins, J. S.; Baker, M. S.; Phillips, S. T. *Macromolecules* **2013**, *46*, 5924. (g) Lewis, G. G.; Robbins, J. S.; Phillips, S. T. *Macromolecules* **2013**, *46*, 5177. (h) DiLauro, A. M.; Abbaspourrad, A.; Weitz, D. A.; Phillips, S. T. *Macromolecules* **2013**, *46*, 3309. (i) Robbins, J. S.; Schmid, K. M.; Phillips, S. T. *J. Org. Chem.* **2013**, *78*, 3159. (j) DiLauro, A. M.; Robbins, J. S.; Phillips, S. T. *Macromolecules* **2013**, *46*, 2963.

(4) Sabongi, G. J. *Chemical Triggering: Reactions of Potential Utility in Industrial Processes*; Plenum Press: New York, 1987.

(5) Alkilany, A. M.; Thompson, L. B.; Boulos, S. P.; Sisco, P. N.; Murphy, C. J. *Adv. Drug Del. Rev.* **2012**, *64*, 190.

(6) Kumar, C. S. S. R.; Mohammad, F. *Adv. Drug Del. Rev.* **2011**, *63*, 789.

(7) (a) Grüll, H.; Langereis, S. *J. Control. Release* **2012**, *161*, 317. (b) Haar, G.; Coussios, C. *Int. J. Hyperthermia* **2006**, *23*, 89.

(8) (a) Coulembier, O.; Knoll, A.; Pires, D.; Gotsmann, B.; Duerig, U.; Frommer, J.; Miler, R. D.; Dubois, P.; Hedrick, J. L. *Macromolecules* **2010**, *43*, 572. (b) Knoll, A. W.; Pires, D.; Coulembier, O.; Dubois, P.; Hedrick, J. L.; Frommer, J.; Duerig, U. *Adv. Mater.* **2010**, *22*, 3361. (c) Kostler, S.; Zechner, B.; Trathnigg, B.; Fasl, H.; Kern, W.; Ribitsch, V. *J. Polym. Sci. Part A: Polym. Chem.* **2009**, *47*, 1499.

(9) (a) Zeng, B.; Huang, J.; Wright, M. W.; King, S. B. *Bioorg. Med. Chem. Lett.* **2004**, *14*, 5565. (b) Xu, Y.; Alavanja, M.; Johnson, V. L.; Yasaki, G.; King, S. B. *Tetrahedron Lett.* **2000**,

41, 4265. (c) Christie, C. C.; Kirby, G. W.; McGuigan, H.; Mackinnon, J. W. M. *J. Chem. Soc. Perkin Trans.* **1985**, *1*, 2469.

(10) (a) Frazier, C.; Bugarin, A.; Engelking, J.; Read de Alaniz, J. *Org. Lett.* **2012**, *14*, 3620. (b) Chaiyaveij, D.; Cleary, L.; Batsanov, A.; Marder, T.; Shea, K.; Whiting, A. *Org. Lett.* **2011**, *13*, 3442.

(11) Samoshin, A. V.; Hawker, C. J.; Read de Alaniz, J. *ACS Macro Lett.* **2014**, *3*, 753.

(12) King, S. B. *Curr. Med. Chem.* **2003**, *10*, 437.

Appendix A – Determination of Rate Constants

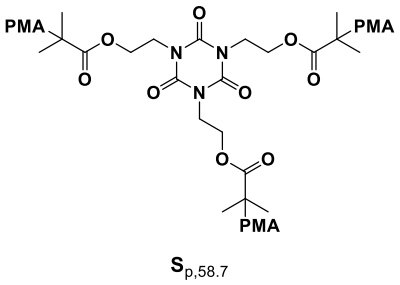

$S_{p,58.7}$

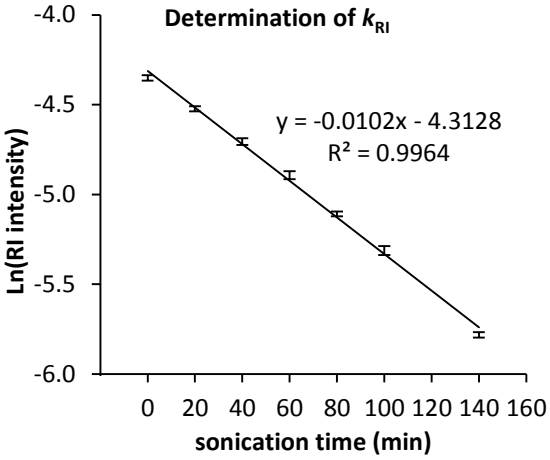

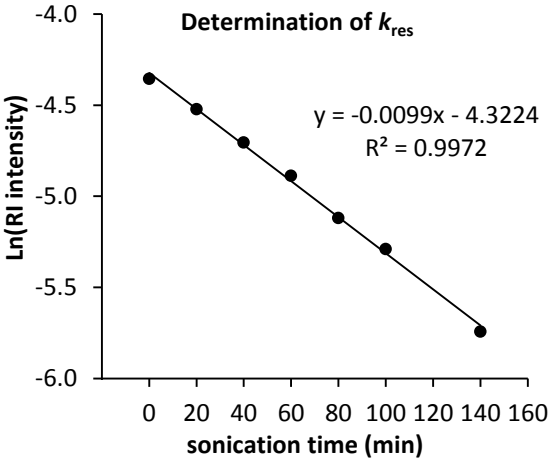

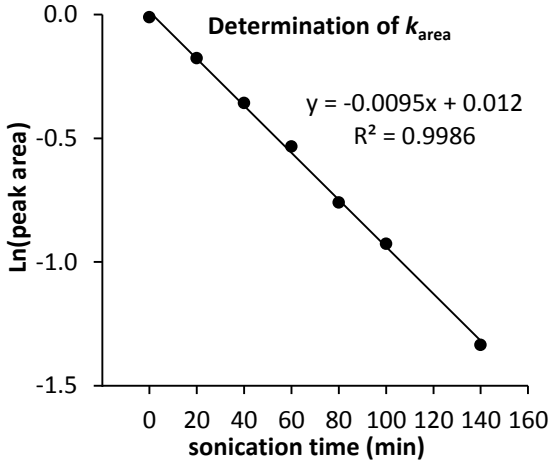

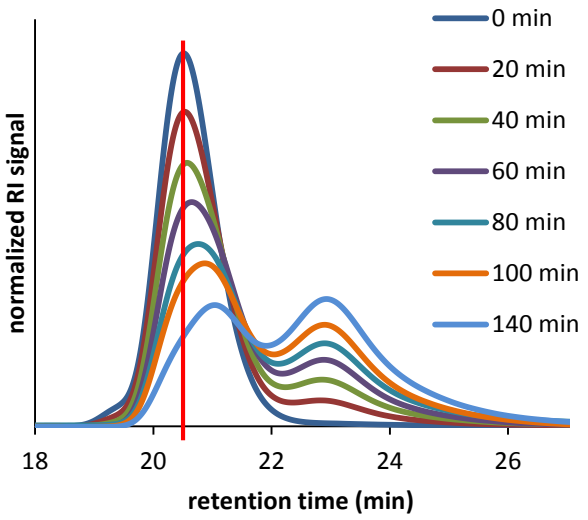

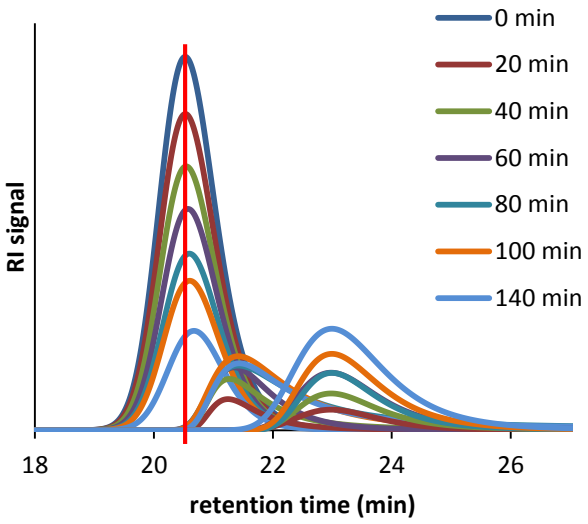

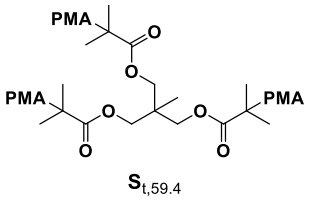
PMA
PMA
PMA
O
O
O
O
O
O
$S_{t,59.4}$

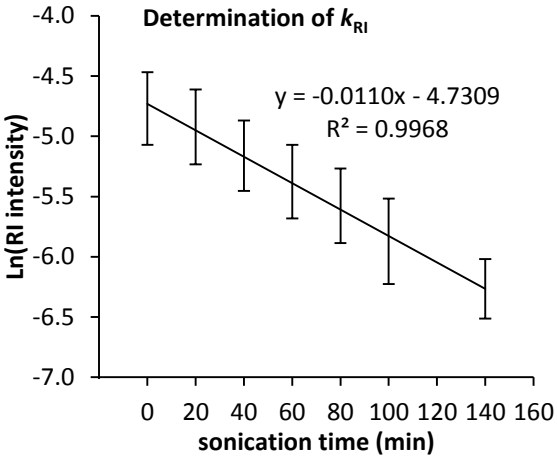
Determination of k_{RI}
y = -0.0110x - 4.7309
R² = 0.9968
Ln(RI intensity)
-4.0
-4.5
-5.0
-5.5
-6.0
-6.5
-7.0
0 20 40 60 80 100 120 140 160
sonication time (min)

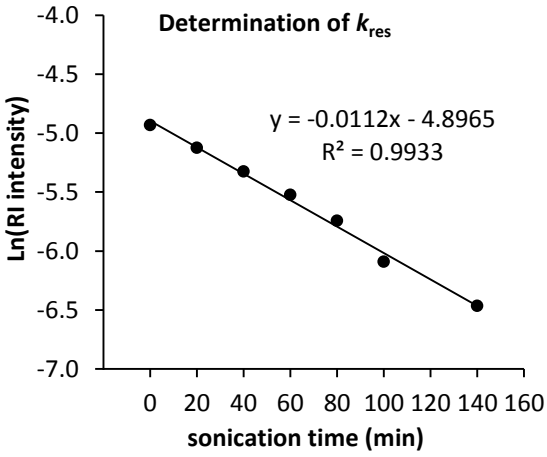
Determination of k_{res}
y = -0.0112x - 4.8965
R² = 0.9933
Ln(RI intensity)
-4.0
-4.5
-5.0
-5.5
-6.0
-6.5
-7.0
0 20 40 60 80 100 120 140 160
sonication time (min)

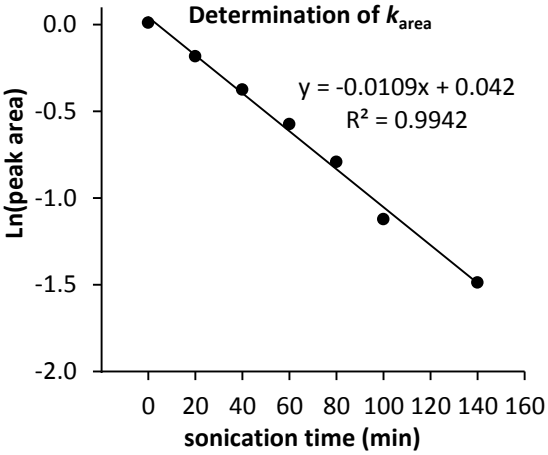
Determination of k_{area}
y = -0.0109x + 0.042
R² = 0.9942
Ln(peak area)
0.0
-0.5
-1.0
-1.5
-2.0
0 20 40 60 80 100 120 140 160
sonication time (min)

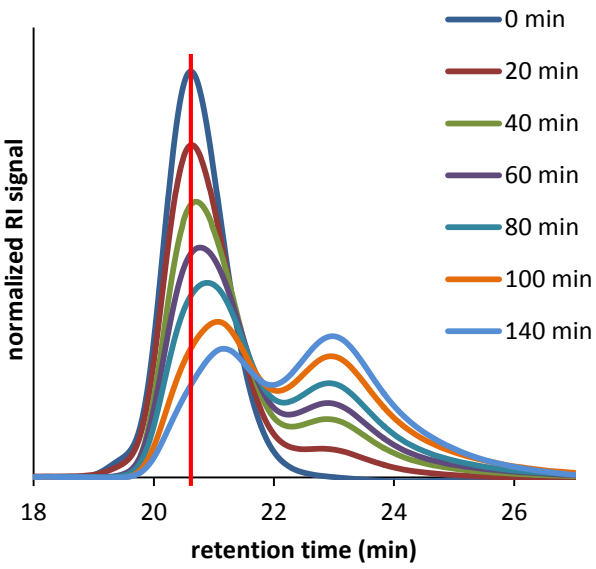
normalized RI signal
0 min
20 min
40 min
60 min
80 min
100 min
140 min
18 20 22 24 26
retention time (min)

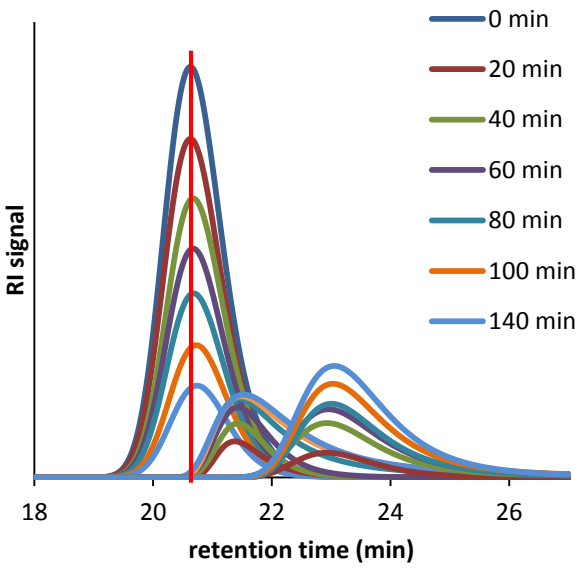
RI signal
0 min
20 min
40 min
60 min
80 min
100 min
140 min
18 20 22 24 26
retention time (min)

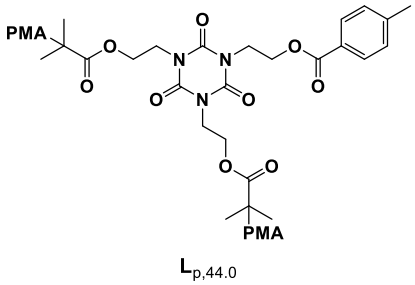
PMA
PMA

$L_{p,44.0}$

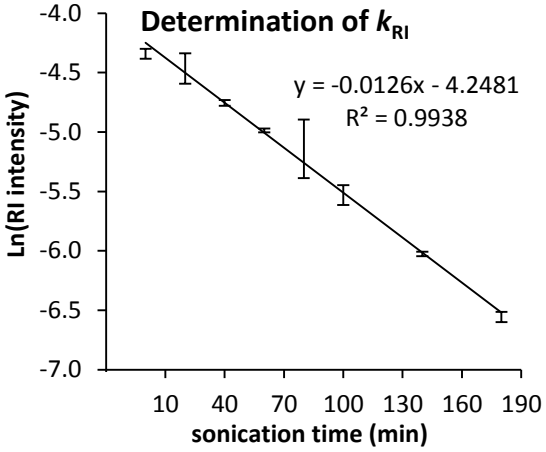
Determination of k_{RI}
y = -0.0126x - 4.2481
R² = 0.9938
Ln(RI intensity)
-4.0
-4.5
-5.0
-5.5
-6.0
-6.5
-7.0
10 40 70 100 130 160 190
sonication time (min)

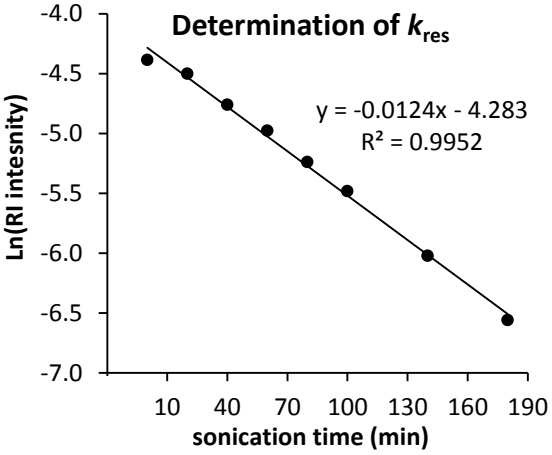
Determination of k_{res}
y = -0.0124x - 4.283
R² = 0.9952
Ln(RI intesnity)
-4.0
-4.5
-5.0
-5.5
-6.0
-6.5
-7.0
10 40 70 100 130 160 190
sonication time (min)

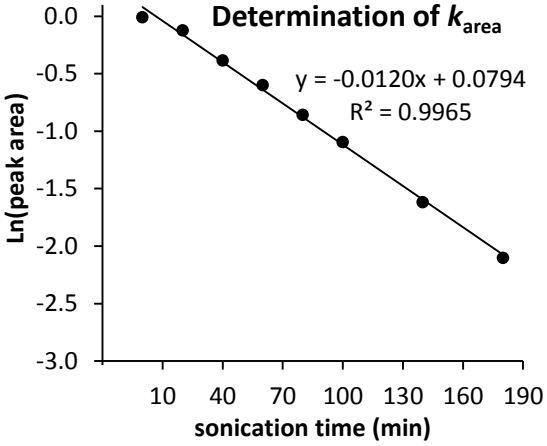
Determination of k_{area}
y = -0.0120x + 0.0794
R² = 0.9965
Ln(peak area)
0.0
-0.5
-1.0
-1.5
-2.0
-2.5
-3.0
10 40 70 100 130 160 190
sonication time (min)

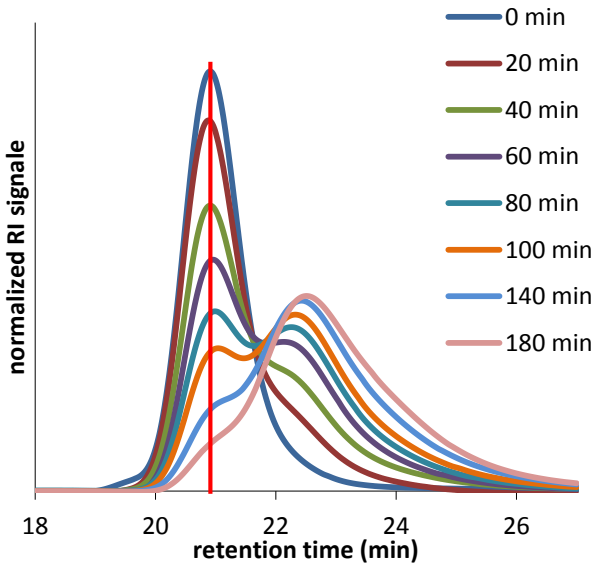
normalized RI signale
0 min
20 min
40 min
60 min
80 min
100 min
140 min
180 min
18 20 22 24 26
retention time (min)

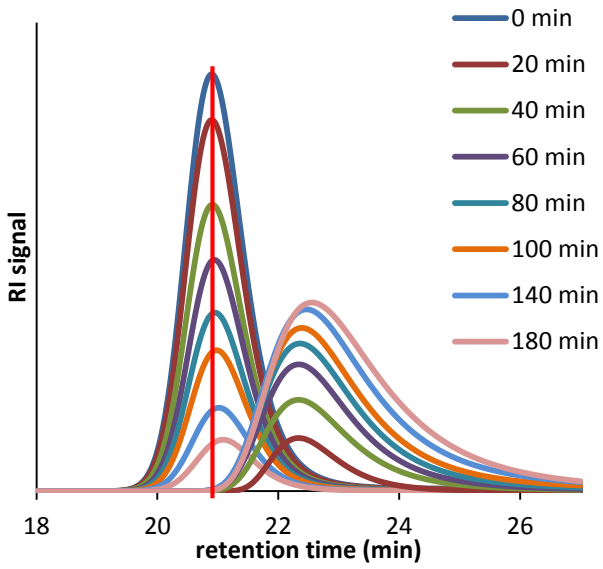
RI signal
0 min
20 min
40 min
60 min
80 min
100 min
140 min
180 min
18 20 22 24 26
retention time (min)

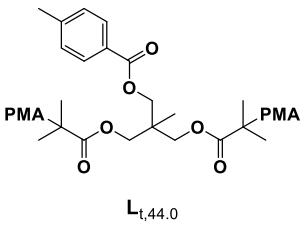
PMA
PMA
O
O
O
O
O
O

$L_{t,44.0}$

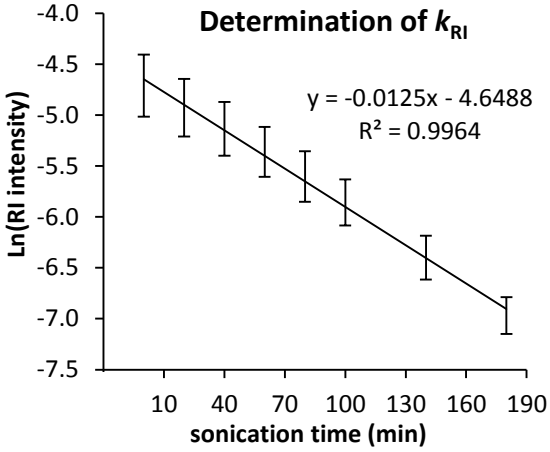
Determination of k_{RI}
y = -0.0125x - 4.6488
R² = 0.9964
Ln(RI intensity)
-4.0
-4.5
-5.0
-5.5
-6.0
-6.5
-7.0
-7.5
10 40 70 100 130 160 190
sonication time (min)

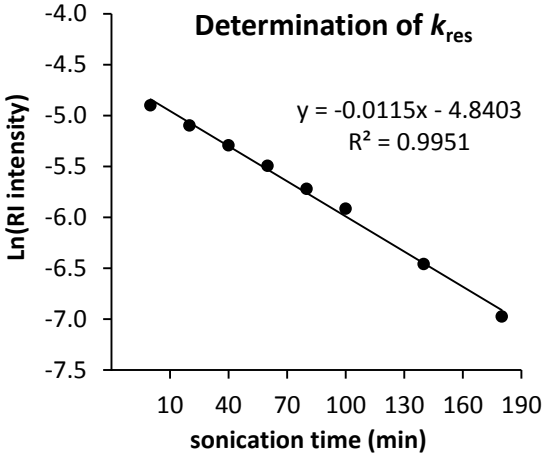
Determination of k_{res}
y = -0.0115x - 4.8403
R² = 0.9951
Ln(RI intensity)
-4.0
-4.5
-5.0
-5.5
-6.0
-6.5
-7.0
-7.5
10 40 70 100 130 160 190
sonication time (min)

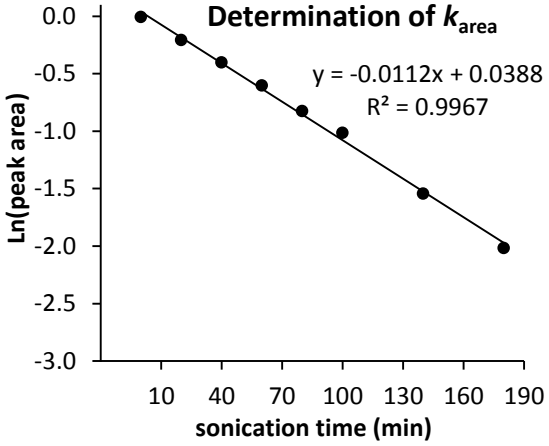
Determination of k_{area}
y = -0.0112x + 0.0388
R² = 0.9967
Ln(peak area)
0.0
-0.5
-1.0
-1.5
-2.0
-2.5
-3.0
10 40 70 100 130 160 190
sonication time (min)

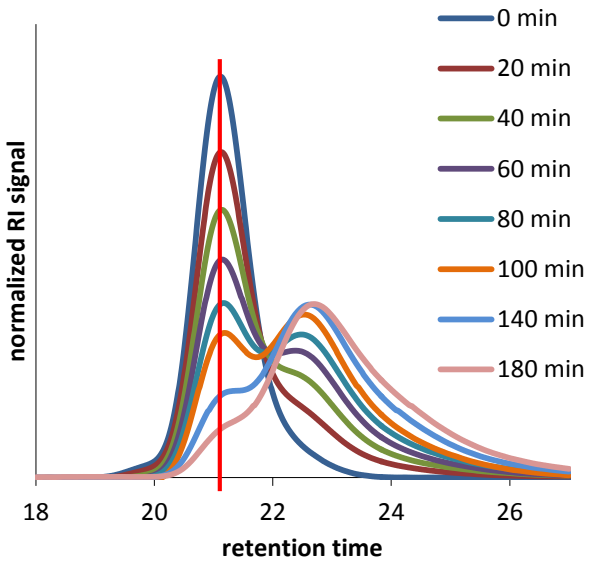
normalized RI signal
0 min
20 min
40 min
60 min
80 min
100 min
140 min
180 min
18 20 22 24 26
retention time

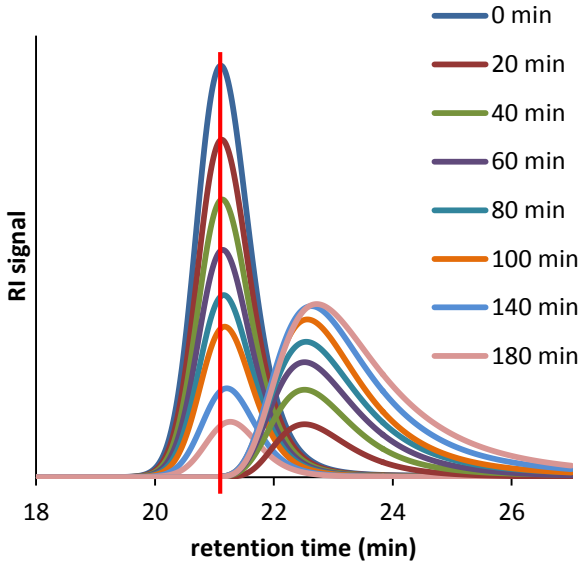
RI signal
0 min
20 min
40 min
60 min
80 min
100 min
140 min
180 min
18 20 22 24 26
retention time (min)

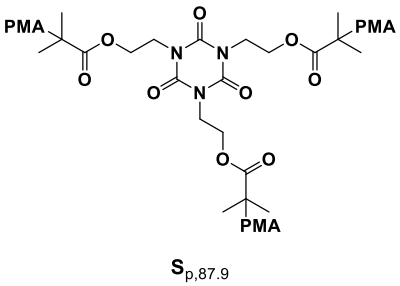
PMA
PMA
PMA

$S_{p,87.9}$

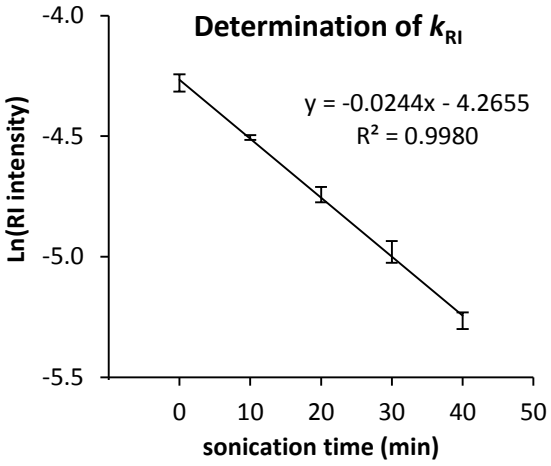
Determination of k_{RI}
y = -0.0244x - 4.2655
R² = 0.9980
Ln(RI intensity)
-4.0
-4.5
-5.0
-5.5
0
10
20
30
40
50
sonication time (min)

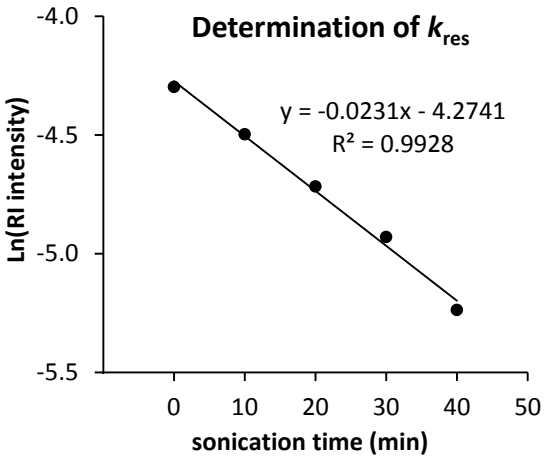
Determination of k_{res}
y = -0.0231x - 4.2741
R² = 0.9928
Ln(RI intensity)
-4.0
-4.5
-5.0
-5.5
0
10
20
30
40
50
sonication time (min)

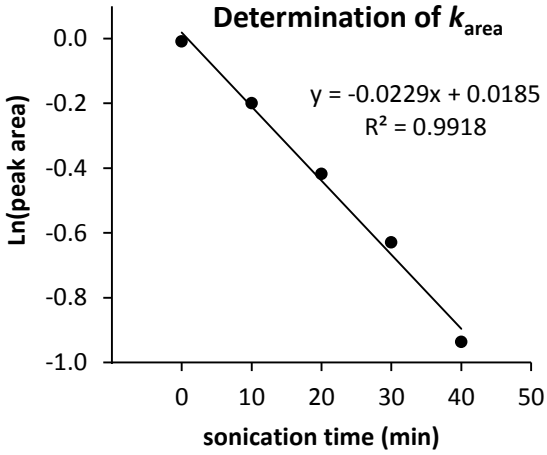
Determination of k_{area}
y = -0.0229x + 0.0185
R² = 0.9918
Ln(peak area)
0.0
-0.2
-0.4
-0.6
-0.8
-1.0
0
10
20
30
40
50
sonication time (min)

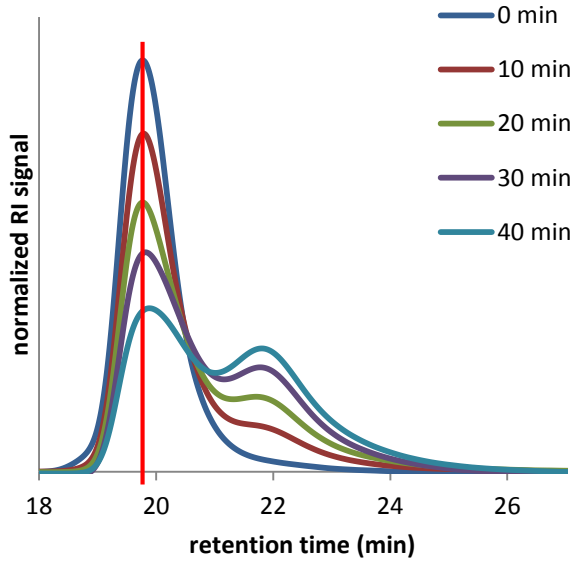
0 min
10 min
20 min
30 min
40 min
normalized RI signal
18
20
22
24
26
retention time (min)

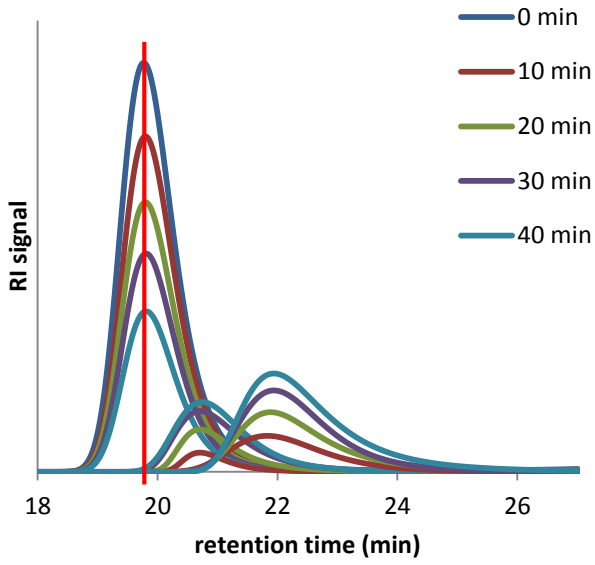
0 min
10 min
20 min
30 min
40 min
RI signal
18
20
22
24
26
retention time (min)

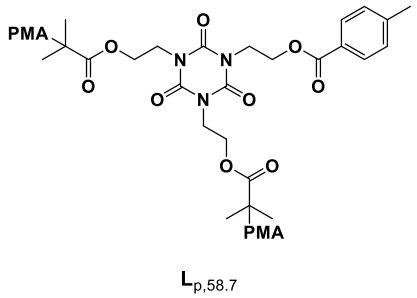
PMA
PMA

$L_{p,58.7}$

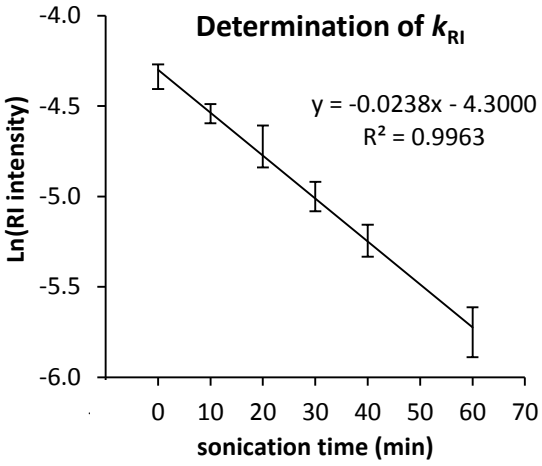
Determination of k_{RI}
y = -0.0238x - 4.3000
R² = 0.9963
Ln(RI intensity)
-4.0
-4.5
-5.0
-5.5
-6.0
0
10
20
30
40
50
60
70
sonication time (min)

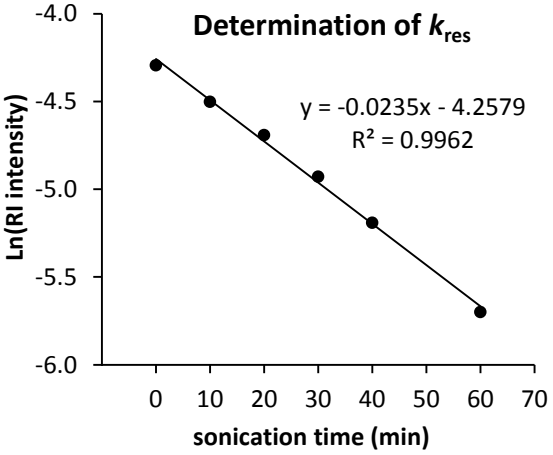
Determination of k_{res}
y = -0.0235x - 4.2579
R² = 0.9962
Ln(RI intensity)
-4.0
-4.5
-5.0
-5.5
-6.0
0
10
20
30
40
50
60
70
sonication time (min)

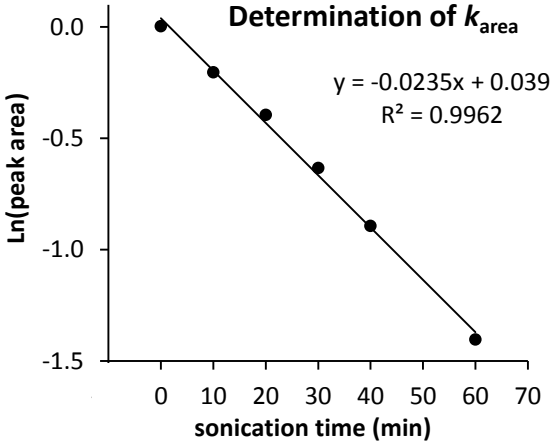
Determination of k_{area}
y = -0.0235x + 0.039
R² = 0.9962
Ln(peak area)
0.0
-0.5
-1.0
-1.5
0
10
20
30
40
50
60
70
sonication time (min)

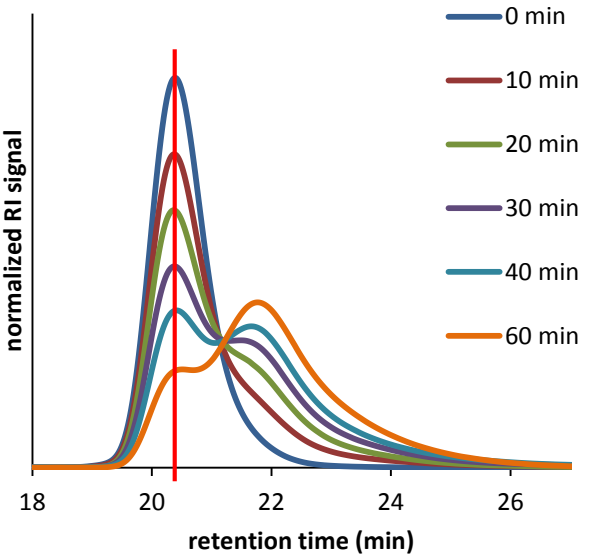
0 min
10 min
20 min
30 min
40 min
60 min
normalized RI signal
18
20
22
24
26
retention time (min)

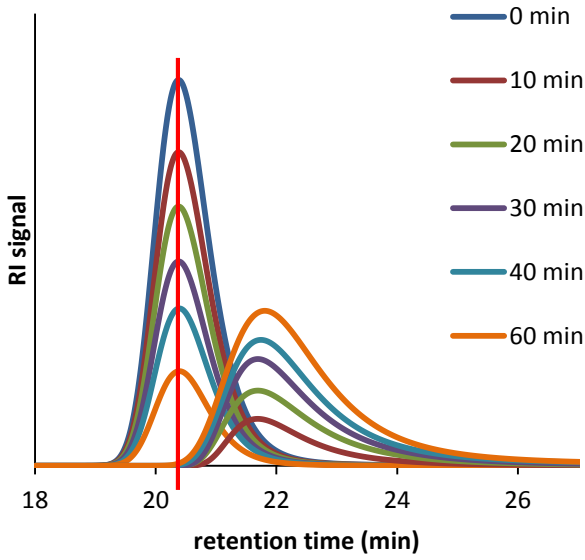
0 min
10 min
20 min
30 min
40 min
60 min
RI signal
18
20
22
24
26
retention time (min)

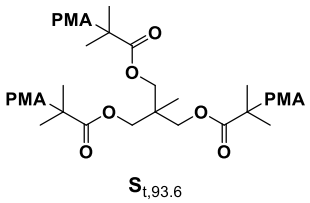
PMA
PMA
PMA
O
O
O
O
O
O
$S_{t,93.6}$

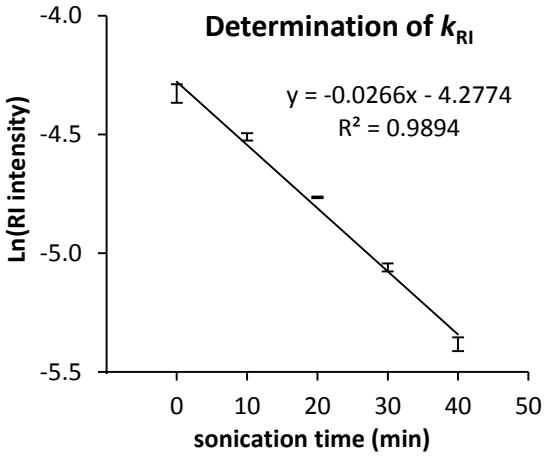
Determination of k_{RI}
y = -0.0266x - 4.2774
R² = 0.9894
Ln(RI intensity)
-4.0
-4.5
-5.0
-5.5
0
10
20
30
40
50
sonication time (min)

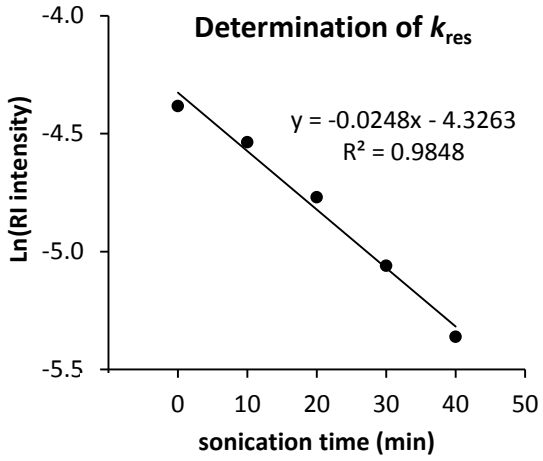
Determination of k_{res}
y = -0.0248x - 4.3263
R² = 0.9848
Ln(RI intensity)
-4.0
-4.5
-5.0
-5.5
0
10
20
30
40
50
sonication time (min)

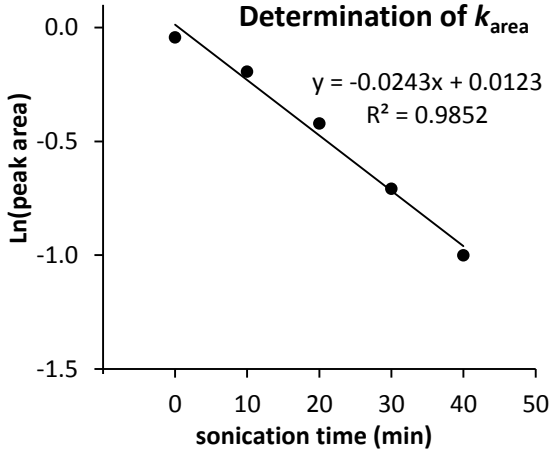
Determination of k_{area}
y = -0.0243x + 0.0123
R² = 0.9852
Ln(peak area)
0.0
-0.5
-1.0
-1.5
0
10
20
30
40
50
sonication time (min)

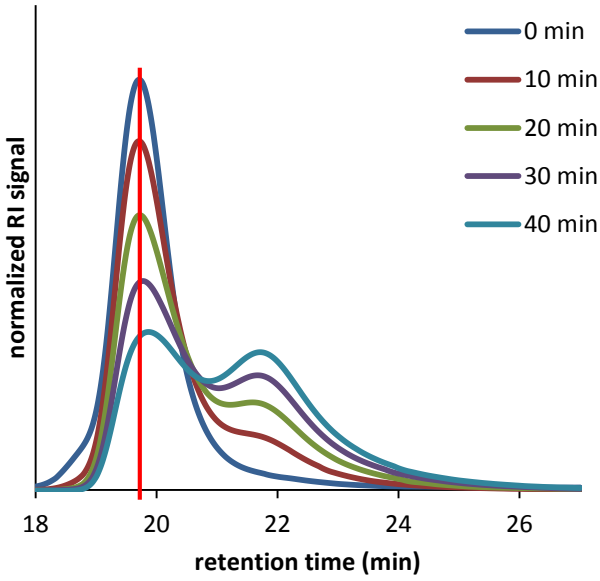
normalized RI signal
0 min
10 min
20 min
30 min
40 min
18
20
22
24
26
retention time (min)

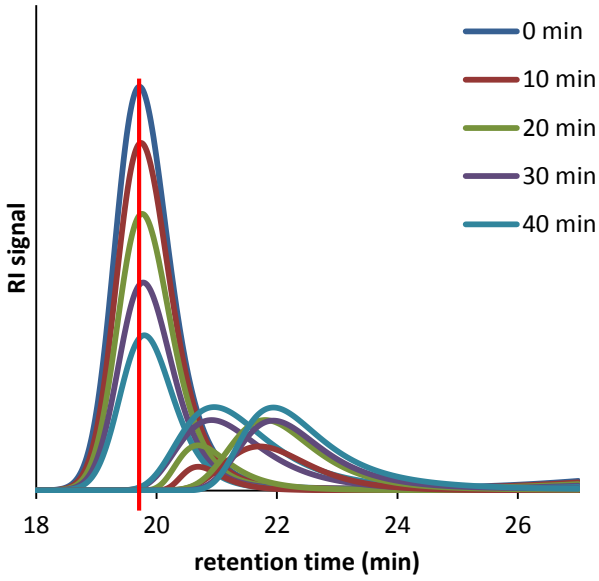
RI signal
0 min
10 min
20 min
30 min
40 min
18
20
22
24
26
retention time (min)

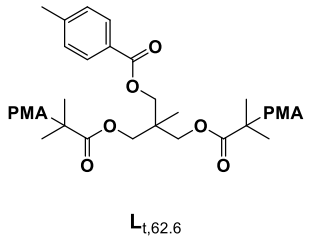
PMA
PMA
O
O
O
O
O
O

$L_{t,62.6}$

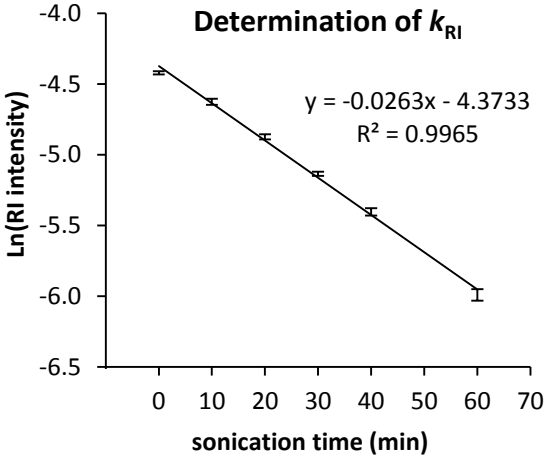
Determination of k_{RI}
y = -0.0263x - 4.3733
R² = 0.9965
Ln(RI intensity)
-4.0
-4.5
-5.0
-5.5
-6.0
-6.5
0
10
20
30
40
50
60
70
sonication time (min)

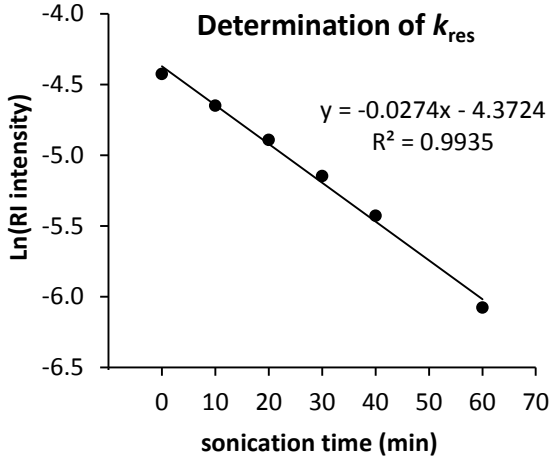
Determination of k_{res}
y = -0.0274x - 4.3724
R² = 0.9935
Ln(RI intensity)
-4.0
-4.5
-5.0
-5.5
-6.0
-6.5
0
10
20
30
40
50
60
70
sonication time (min)

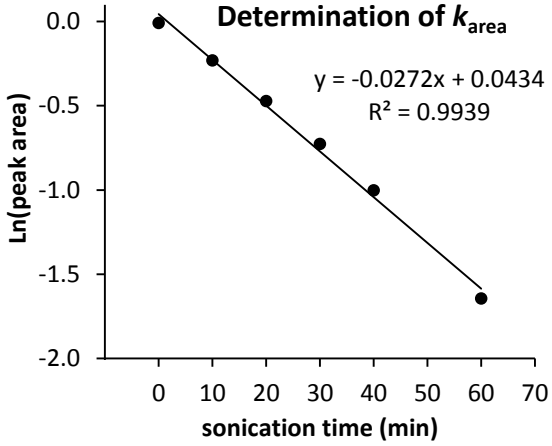
Determination of k_{area}
y = -0.0272x + 0.0434
R² = 0.9939
Ln(peak area)
0.0
-0.5
-1.0
-1.5
-2.0
0
10
20
30
40
50
60
70
sonication time (min)

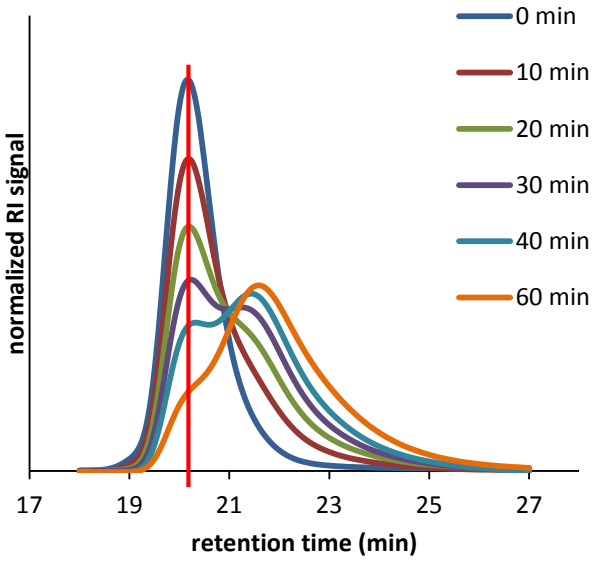
normalized RI signal
0 min
10 min
20 min
30 min
40 min
60 min
17
19
21
23
25
27
retention time (min)

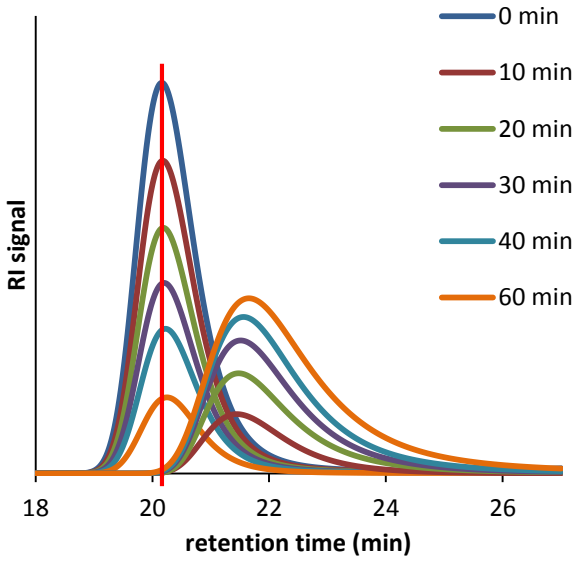
RI signal
0 min
10 min
20 min
30 min
40 min
60 min
18
20
22
24
26
retention time (min)

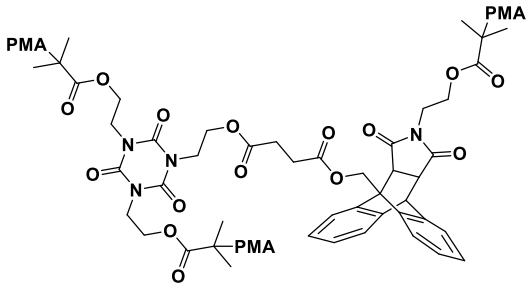
PMA
PMA
PMA

$S_{DA,85.9}$

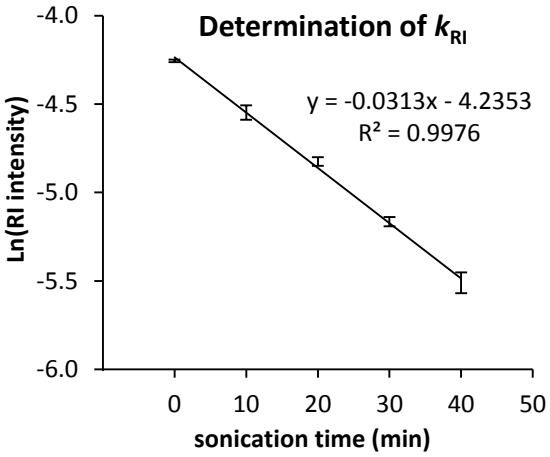
Determination of k_{RI}
y = -0.0313x - 4.2353
R² = 0.9976
Ln(RI intensity)
sonication time (min)

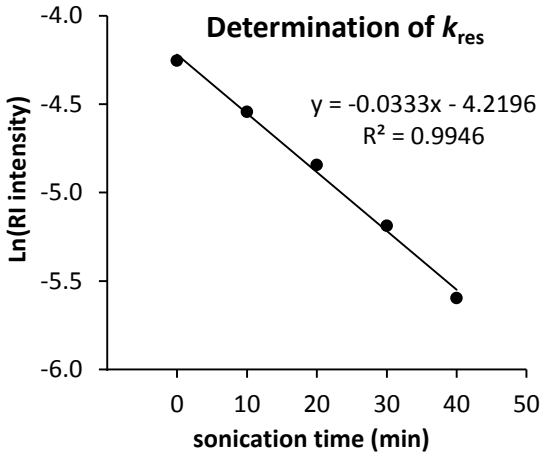
Determination of k_{res}
y = -0.0333x - 4.2196
R² = 0.9946
Ln(RI intensity)
sonication time (min)

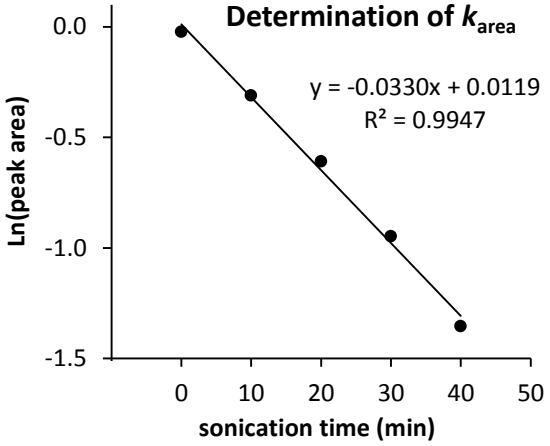
Determination of k_{area}
y = -0.0330x + 0.0119
R² = 0.9947
Ln(peak area)
sonication time (min)

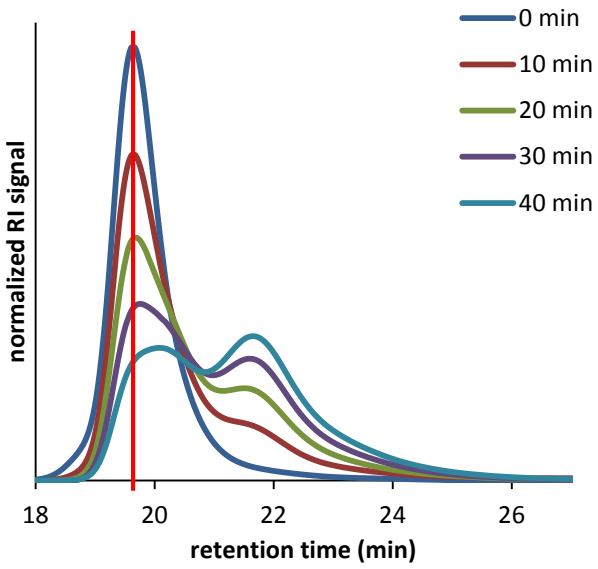
0 min
10 min
20 min
30 min
40 min
normalized RI signal
retention time (min)

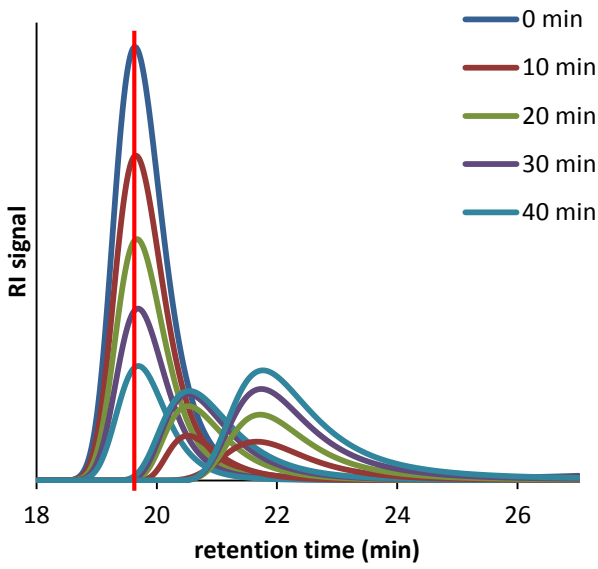
0 min
10 min
20 min
30 min
40 min
RI signal
retention time (min)

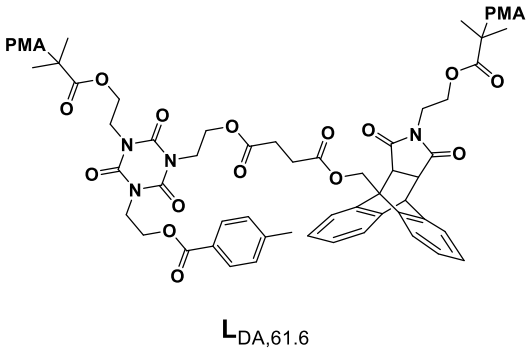
PMA
PMA

$L_{DA,61.6}$

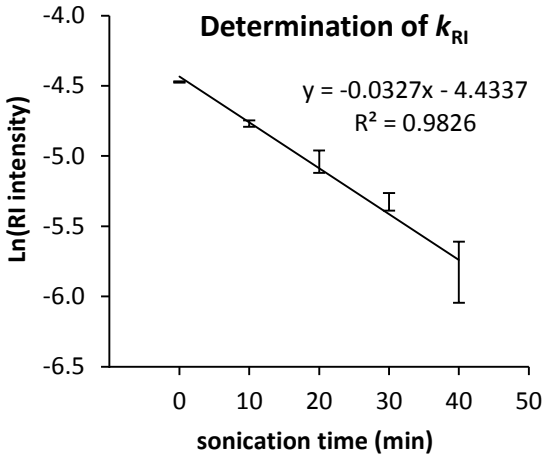
Determination of k_{RI}
y = -0.0327x - 4.4337
R² = 0.9826
Ln(RI intensity)
sonication time (min)

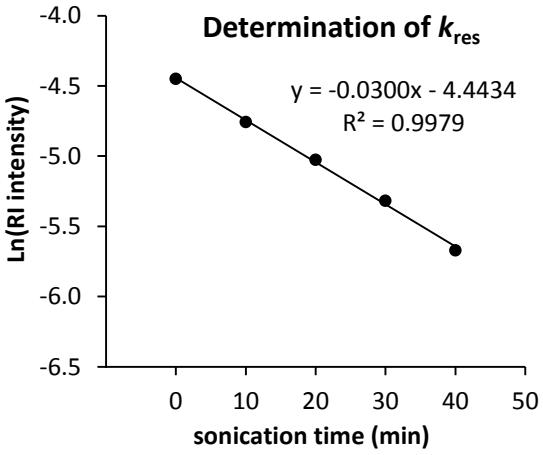
Determination of k_{res}
y = -0.0300x - 4.4434
R² = 0.9979
Ln(RI intensity)
sonication time (min)

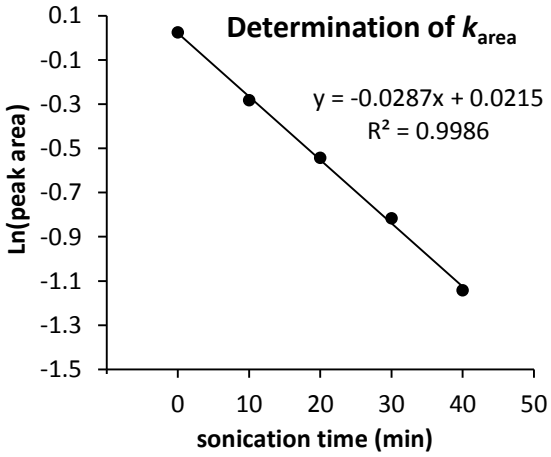
Determination of k_{area}
y = -0.0287x + 0.0215
R² = 0.9986
Ln(peak area)
sonication time (min)

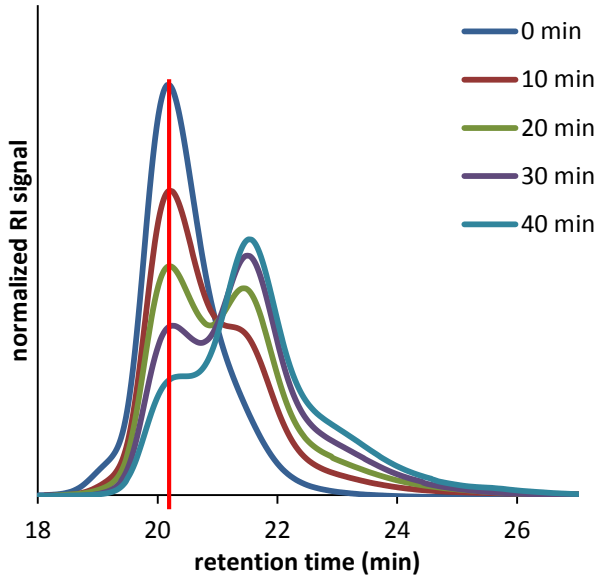
0 min
10 min
20 min
30 min
40 min
normalized RI signal
retention time (min)

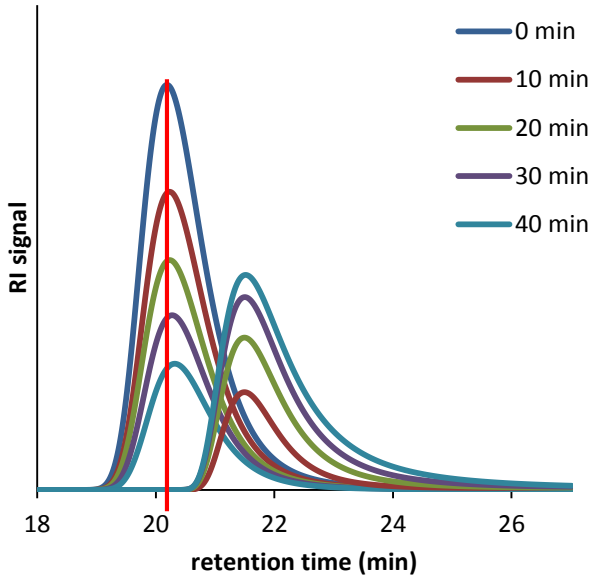
0 min
10 min
20 min
30 min
40 min
RI signal
retention time (min)